JGR Solid Earth

RESEARCH ARTICLE
10.1029/2025JB031738

# Strain Rates Along the Alpine-Himalayan Belt From a Comprehensive GNSS Velocity Field

**N. Castro-Perdomo[1], S. Jónsson[2], Y. Klinger[3], F. Masson[4], T. W. Becker[5,6,7], and K. Johnson[1]**

[1]Department of Earth and Atmospheric Sciences, Indiana University, Bloomington, IN, USA, [2]Physical Science and Engineering Division, King Abdullah University of Science and Technology (KAUST), Thuwal, Saudi Arabia, [3]Université Paris Cité, Institut de Physique du Globe de Paris, CNRS, Paris, France, [4]ITES, EOST Université de Strasbourg, CNRS, Strasbourg, France, [5]Institute for Geophysics, Jackson School of Geosciences, The University of Texas at Austin, Austin, TX, USA, [6]Department of Earth and Planetary Sciences, Jackson School of Geosciences, The University of Texas at Austin, Austin, TX, USA, [7]Oden Institute for Computational Engineering & Sciences, The University of Texas at Austin, Austin, TX, USA

**Abstract** The Alpine-Himalayan belt is one of Earth's most dynamic and complex regions, characterized by intense tectonic deformation and seismicity. Comprehensive analyses of continental-scale crustal deformation and seismic hazards along this extensive orogenic belt require the compilation of large geodetic data sets. In this study, we integrate 42 published Global Navigation Satellite System (GNSS) velocity fields, building an internally consistent data set for the entire belt, spanning from Iberia to Southeast Asia and comprising 11,177 horizontal and 3,940 vertical velocities. We use this unified GNSS velocity field to estimate surface strain rates and their posterior uncertainties in the eastern Mediterranean region and the India-Asia collision zone. Our results show large-scale agreement between the orientation and style of geodetic and seismic strain rate tensors across the belt. Additionally, our analyses substantiate previously documented azimuthal alignments between principal strain rate directions and seismic anisotropy orientations, often used as a proxy for finite strain in the convecting mantle. These correlations are particularly apparent in the Aegean, North Anatolia, Tibet, Tian Shan, Altai, Sayan, and Baikal regions, underscoring the need for future research on the relationship between mantle flow and lithospheric deformation.

**Plain Language Summary** The Alpine-Himalayan Belt, extending from Iberia to Southeast Asia, is one of the most tectonically active regions on Earth, frequently affected by large and damaging earthquakes. In this study, we compile and merge geodetic data across this vast region to construct a unified and comprehensive crustal deformation velocity field. Using this new model, we estimate the rates at which the Earth's surface deforms due to tectonic and geodynamic processes. Our results show strong agreement between the orientation and style of geodetic strain accumulation in the crust and strain release during earthquakes. Additionally, we substantiate the regional angular alignments between surface deformation patterns and azimuthal seismic anisotropy, often used as a proxy for deformation in the Earth's upper mantle.

**Key Points:**

- We build a comprehensive GNSS velocity field for the Alpine-Himalayan belt, including over 11,000 horizontal velocities
- We estimate strain rates and posterior uncertainties in the eastern Mediterranean and the India-Asia collision zone
- We find consistency between the orientation and style of geodetic and seismic strain rate tensors across the Alpine-Himalayan belt

**Supporting Information:**

Supporting Information may be found in the online version of this article.

**Correspondence to:**

N. Castro-Perdomo,
jcastrop@iu.edu

**Citation:**

Castro-Perdomo, N., Jónsson, S., Klinger, Y., Masson, F., Becker, T. W., & Johnson, K. (2025). Strain rates along the Alpine-Himalayan belt from a comprehensive GNSS velocity field. *Journal of Geophysical Research: Solid Earth*, *130*, e2025JB031738. https://doi.org/10.1029/2025JB031738

Received 10 APR 2025
Accepted 30 NOV 2025

**Author Contributions:**

**Conceptualization:** S. Jónsson, F. Masson
**Data curation:** N. Castro-Perdomo, T. W. Becker
**Formal analysis:** N. Castro-Perdomo
**Funding acquisition:** S. Jónsson, T. W. Becker, K. Johnson
**Software:** N. Castro-Perdomo
**Supervision:** K. Johnson
**Writing – original draft:** N. Castro-Perdomo
**Writing – review & editing:** S. Jónsson, Y. Klinger, F. Masson, T. W. Becker, K. Johnson





## 1. Introduction

The Alpine-Himalayan belt, associated with the closure of the Tethyan ocean, extends over 10,000 km from Gibraltar to the Indochina Peninsula in Southeast Asia and ranks among Earth's most seismically active and tectonically complex regions (e.g., Argand, 1922; Carey, 1955; Hatzfeld & Molnar, 2010; Molnar & Tapponnier, 1975; Reilinger & McClusky, 2011; Şengör, 1986). Formed through the northward subduction of the Neo-Tethys oceanic lithosphere from the Late Mesozoic to Early Cenozoic, this extensive convergence zone has been a major collisional boundary where the Eurasian Plate converged with Gondwanaland-derived fragments, including the Nubian, Arabian, and Indian Plates, as well as several smaller lithospheric blocks (e.g., Dercourt et al., 1986; Read & Watson, 1975).

These tectonic interactions have produced a broad deformation zone along the southern margin of the Eurasian plate. This zone features a nascent convergent boundary in Northern Africa (Billi et al., 2023), active subduction along the Calabria, Hellenic, Cyprus, Makran and Sunda megathrusts (e.g., Barbot & Weiss, 2021; Faccenna et al., 2011; Faccenna, Becker, Auer, et al., 2014; L. Jolivet et al., 2013; Lindsey et al., 2023), continental collision along the Caucasus, Zagros, and Himalayas, and lateral transport zones in Anatolia and the eastern and western

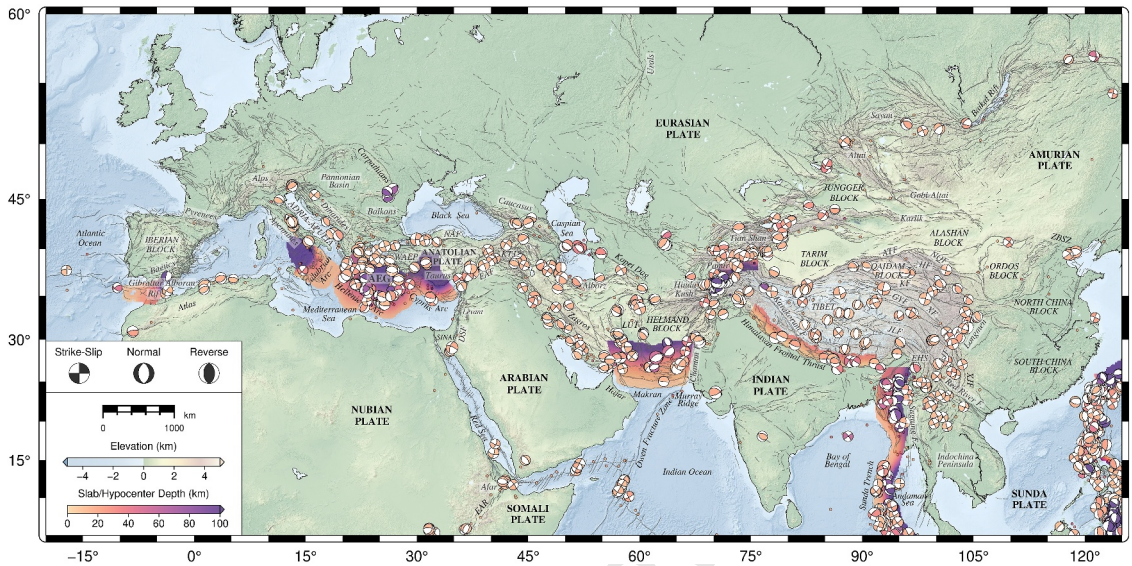


**Figure 1.** Main tectonic features and seismicity along the Alpine-Himalayan belt. Slab depths are from Slab2 (Hayes et al., 2018) and ESHM2020 (Danciu et al., 2024). Faults are sourced from AFEAD (Zelenin et al., 2021). Moment tensors for $M_W \geq 6$ earthquakes are from the gCMT catalog (Dziewonski et al., 1981; Ekström et al., 2012), with $6 \geq M_W \geq 5$ earthquakes represented as dots. AEG, Aegean Sea Plate; WAEP, Western Anatolian Extensional Province; DSF, Dead Sea Fault; EAF, East Anatolian Fault; NAF, North Anatolian Fault; EAR, East African Rift; ATF, Altyn Tagh Fault; KF, Kunlun Fault; EHS, Eastern Himalayan Syntaxis; XJF, Xiaojiang Fault; XF, Xianshuihe Fault; JF, Jiali Fault; GYF, Ganzi-Yushu Fault; ZBSZ, Zhangjiakou-Bohai Seismic Zone; LJF, Lijiang Fault; HF, Haiyuan Fault; NQF, North Qilian Fault.

margins of the Tibetan Plateau (e.g., Hatzfeld & Molnar, 2010; Tapponnier et al., 1982; Wang & Shen, 2020). The Alpide belt also hosts prominent mountain ranges, including the Atlas, Alps, Hellenides, Taurides, Zagros, Makran, and the Himalayas, all of which experience ongoing crustal deformation and heightened seismicity (e.g., Bilham, 2006; Jackson & McKenzie, 1984; McKenzie, 1978; Reilinger & McClusky, 2011), as illustrated in Figure 1.

Renewed interest in seismic hazards along the Alpine-Himalayan belt has been spurred by a series of devastating earthquakes in 2023 across various sections of the belt and neighboring regions, including the moment magnitude ($M_W$) 7.8 and 7.6 Kahramanmaraş earthquake doublet in Türkiye and Syria (e.g., Ergintav et al., 2024; Mai et al., 2023), four $M_W$6.3 earthquakes near Herat in Afghanistan (He et al., 2024), and the $M_W$6.9 Al Haouz earthquake in Morocco (Yeck et al., 2023). In 2025, two additional large earthquakes struck the region: the $M_W$7.1 Shigatse earthquake in southern Tibet and the $M_W$7.7 Mandalay earthquake in Myanmar. Collectively, these events resulted in thousands of casualties and extensive economic losses, underscoring the urgent need for improved earthquake resilience and continental-scale studies of strain accumulation and release along the Alpides (Abdrakhmatov et al., 2024).

Previous efforts to compile GNSS velocities at regional and global scales have provided valuable insights into the deformation mechanisms along the Alpide belt (e.g., Devoti et al., 2017; Faccenna, Becker, Auer, et al., 2014; Graham et al., 2018; Hatzfeld & Molnar, 2010; Kreemer et al., 2014; Li et al., 2025; Piña-Valdés et al., 2022; Serpelloni et al., 2022; Steffen et al., 2025; Weiss et al., 2020; Wang & Shen, 2020; Wang & Barbot, 2023). In addition, significant progress has been made in integrating interferometric synthetic aperture radar (InSAR) observations to illuminate areas with limited GNSS station coverage (e.g., Barnhart, 2017; Bletery et al., 2020; Chen et al., 2024; Fattahi & Amelung, 2016; X. Huang et al., 2023; Z. Huang et al., 2023; Hussain et al., 2018; Jolivet et al., 2023; Lazecký et al., 2020; Li et al., 2024; Li, Nocquet, Shan, & Song, 2021; Liu & Wang, 2023; Ou et al., 2022; Viltres et al., 2025; Watson et al., 2024; Weiss et al., 2020). Some of these studies have specifically evaluated surface strain rates, enhancing our understanding of the spatial distribution and intensity of crustal deformation across different sections of the belt (e.g., Barbot & Weiss, 2021; Chen et al., 2024; Chousianitis et al., 2024; Fang et al., 2024; Faccenna, Becker, Auer, et al., 2014; Kreemer et al., 2014; Liu & Wang, 2023; Lindsey et al., 2023; Li et al., 2025; Nucci et al., 2025; Piña-Valdés et al., 2022; Serpelloni et al., 2022; Steffen et al., 2025; Weiss et al., 2020; Wang & Shen, 2020; Wang & Barbot, 2023).

Recent improvements in geodetic monitoring and station deployment have significantly increased the spatial density of GNSS networks across the Alpides, leading to new GNSS velocity fields for Anatolia (e.g., Ergintav et al., 2023; Kurt et al., 2023), the Euro-Mediterranean (e.g., Piña-Valdés et al., 2022; Serpelloni et al., 2022), northern Africa (e.g., Bahrouni et al., 2020; Billi et al., 2023; Bougrine et al., 2019), the Arabian Plate (Viltres et al., 2022), Tibet (e.g., Li et al., 2025), and the India-Asia collision zone (e.g., Lindsey et al., 2023; Wang & Shen, 2020). Collectively, these studies provide a robust foundation for understanding regional tectonics and refining our estimates of strain rates, ultimately supporting seismic hazard assessment efforts along this extensive orogenic belt.

In this paper, we build upon those recent studies by compiling a unified, comprehensive, and up-to-date GNSS velocity field along the Alpine-Himalayan belt (hereafter referred to interchangeably as the Alpide belt or Alpides). Using this data set, we estimate strain rates and posterior uncertainties for two focus regions: the eastern Mediterranean and the India-Asia collision zone, areas with the highest strain rates and dense GNSS station coverage. Our strain rate inversions explicitly account for velocity discontinuities across known creeping faults in the eastern Mediterranean, thereby avoiding the erroneous mapping of surface creep into strain rates associated with elastic coupling on faults, a distinction relevant for seismic hazard assessment.

Additionally, we demonstrate the utility of our combined GNSS velocity field for examining large-scale spatial patterns and relationships between GNSS-derived surface strain rate styles and earthquake strain release styles from Kostrov-summed earthquake moment tensors (Dziewonski et al., 1981; Ekström et al., 2012), present-day stress release styles (Heidbach et al., 2025), and mantle dynamics inferred from seismic anisotropy compilations (Becker et al., 2012). Consequently, our study lays the foundation for future research on the links between strain accumulation and release, as well as the potential interplay between large-scale mantle dynamics and surface deformation along the Alpine-Himalayan belt.

## 2. Combined GNSS Velocity Field

In this study, we introduce `FICORO_GNSS` (Castro-Perdomo, 2024), a Python software package developed to systematically filter and combine GNSS velocity fields. Utilizing this tool, we integrated 42 published velocity data sets across various sections of the Alpine-Himalayan belt (Table 1), resulting in a comprehensive GNSS velocity field comprising 11,177 horizontal and 3,940 vertical velocities (Figure 2). Our methodology draws inspiration from the approaches of Piña-Valdés et al. (2022), who combined GNSS velocity solutions across Europe, and Zeng (2022), who developed the GNSS velocity field for the U.S. National Seismic Hazard Model. `FICORO_GNSS` implements a robust filtering and combination process consisting of 10 key steps:

1. *Removing stations affected by postseismic transient motions:* GNSS stations identified as being affected by postseismic transient motions in published velocity solutions were removed from the input data. This was accomplished by removing stations within a predefined radius around earthquake epicenters when previous studies explicitly reported postseismic transients. However, this approach represents only a first-order filter, as recent studies have shown measurable far-field deformation extending hundreds of kilometers from large earthquakes (e.g., Ergintav et al., 2024), and that postseismic transients may persist longer than previously assumed (Liu et al., 2020). Consequently, our combined velocity field and derived strain rate estimates might still include residual postseismic signals, particularly near the epicentral areas of the 2001 $M_s$8.1 Kunlun earthquake in northern Tibet and the 2020 $M_W$6.7 Elazığ earthquake in eastern Türkiye, where some previous interseismic velocity fields inadvertently incorporated transient signals.
2. *Filtering based on uncertainty distribution:* We refined the input horizontal GNSS velocity fields by fitting a lognormal distribution to the east and north components of velocity uncertainties. Following the method outlined by Piña-Valdés et al. (2022), stations with uncertainties exceeding the 99th percentile of the fitted lognormal distribution were removed, as illustrated in Figure S1 of Supporting Information S1.
3. *Filtering based on spatial coherence of velocity magnitudes:* We applied the standard (Z-Score) method used by Piña-Valdés et al. (2022) to identify and remove outlier GNSS stations based on velocity coherence with neighboring stations. GNSS stations whose velocity magnitudes in the East and North components deviated by more than two standard deviations, $2\sigma$, from the mean within a 20 km radius were removed. In tectonically active regions, a more lenient threshold of $3\sigma$ was used to account for greater variability in GNSS velocities.
4. *Aligning input GNSS velocity fields to ITRF2014:* We applied a six-parameter Helmert transformation of GNSS velocities, solving for three translation rates $\dot{\mathbf{T}} = \left(\dot{T}_x, \dot{T}_y, \dot{T}_z\right)$ and three rotation rates

**Table 1**
*GNSS Velocity Fields Used in the Combination, and Their Alignment Statistics*

| Source | Study area | Sites | Reference frame | Ties | RMS (mm/yr) |
|---|---|---|---|---|---|
| Alchalbi et al. (2010) | Northern Dead Sea Fault | 62 | ITRF2000 | 14 | 0.45 |
| Bahrouni et al. (2020)[a] | Tunisia | 42 | ITRF2014 | 38 | 0.26 |
| Billi et al. (2023) | Northern Africa | 431 | Eurasia ITRF2014 | 292 | 0.26 |
| Bougrine et al. (2019) | Algeria | 313 | ITRF2014 | 259 | 0.37 |
| Briole et al. (2021)[b] | Aegean | 329 | ITRF2014 | 188 | 0.97 |
| Brockmann et al. (2019)[b,c] | Euromediterranean (EPN) | 3,047 | Eurasia | 2,492 | 0.16 |
| Brockmann et al. (2019)[b,c] | Switzerland (EPN-CH8) | 214 | Eurasia | 245 | 1.63 |
| Castro-Perdomo et al. (2022)[b] | Southern Dead Sea Fault | 66 | ITRF2014 | 56 | 0.33 |
| England et al. (2016)[d] | Anatolia | 346 | Eurasia | 26 | 0.68 |
| Ergintav et al. (2023)[b] | Anatolia | 732 | Anatolia ITRF2014 | 108 | 1.04 |
| Floyd et al. (2023)[b] | Hellenic subduction zone | 360 | Eurasia | 70 | 1.34 |
| Gomez et al. (2020)[a] | Dead Sea Fault | 181 | ITRF2008 | 26 | 1.15 |
| Graham et al. (2018)[d] | Global | 8,354 | North America | 1,957 | 0.50 |
| Hamiel and Piatibratova (2021)[a] | Dead Sea Fault | 291 | ITRF2014 | 57 | 0.90 |
| R. Jolivet et al. (2023)[b] | North Anatolian Fault | 81 | ITRF2014 | 51 | 0.46 |
| Kadirov et al. (2014)[e] | Caucasus - Azerbaijan | 110 | Eurasia ITRF2000 | 50 | 0.26 |
| Karakhanyan et al. (2013)[a] | Armenia and Lesser Caucasus | 55 | Eurasia ITRF2008 | 49 | 0.26 |
| Khorrami et al. (2019)[a] | Iran | 399 | Eurasia ITRF2008 | 21 | 0.45 |
| Kurt et al. (2023) | Anatolia | 836 | Eurasia | 8 | 0.57 |
| Y. Li et al. (2025)[d] | Tibet-SE Asia | 4,458 | Eurasia-fixed | 101 | 0.59 |
| Liang et al. (2013)[b] | Tibetan Plateau | 750 | Eurasia ITRF2008 | 18 | 1.07 |
| McClusky et al. (2010) | Afar triple junction | 58 | Nubia | 19 | 0.54 |
| Nocquet (2012)[d] | Euromediterranean | 1,495 | Eurasia | 757 | 0.36 |
| Özarpacı et al. (2021) | North Anatolian Fault | 61 | Eurasia | 23 | 0.25 |
| Özbey et al. (2024)[a] | Cyprus and East Anatolia | 98 | ITRF2014 | 20 | 0.21 |
| Özdemir and Karslıoğlu (2019)[a] | Anatolia | 213 | Eurasia | 41 | 0.25 |
| Özkan et al. (2023)[a] | Hatay Triple Junction | 65 | Eurasia | 40 | 0.26 |
| Perry et al. (2019) | Pamir-Hindu Kush | 82 | Eurasia ITRF2008 | 23 | 0.62 |
| Piña-Valdés et al. (2022)[d,b] | Euromediterranean | 4,837 | ITRF2014 | 2871 | 0.37 |
| Reilinger et al. (2006) | Euromediterranean | 433 | Eurasia | 178 | 0.72 |
| Saleh and Becker (2014) | Egypt | 149 | Eurasia | 122 | 0.61 |
| Serpelloni et al. (2022)[b] | Euromediterranean | 3,350 | ITRF2014 | [f] | [f] |
| Sokhadze et al. (2018)[a,b] | Caucasus - Georgia | 72 | Eurasia | 24 | 0.21 |
| Stamps et al. (2018)[a] | East African Rift | 153 | Nubia | 95 | 0.48 |
| Tatar et al. (2012) | North Anatolian Fault | 48 | Eurasia | 30 | 0.56 |
| Viltres et al. (2020) | Danakil - Southern Red Sea | 33 | Nubia | 4 | 0.13 |
| Viltres et al. (2022)[b] | Arabia | 189 | ITRF2014 | 27 | 0.33 |
| L. Wang and Barbot (2023)[d] | India-Eurasia collision | 2,870 | Local NNRT[c] | 55 | 0.53 |
| M. Wang and Shen (2020)[a] | China | 3,273 | China | 99 | 0.49 |
| Wedmore et al. (2021)[a] | Africa | 262 | ITRF2014 | 150 | 0.44 |
| Zubovich et al. (2016) | Pamir and Tian Shan | 411 | Eurasia | 22 | 0.62 |
| Zheng et al. (2017)[a] | India-Eurasia collision | 2,576 | Eurasia | 46 | 0.48 |

[a]GNSS velocity fields that incorporate data from earlier studies to densify GNSS station coverage. [b]GNSS velocity fields reporting vertical velocities. [c]No-Net-Rotation and Translation. [d]GNSS velocity fields that are themselves combinations of previous data sets (see Table S2 in Supporting Information S1). [e]First rotated into Karakhanyan et al. (2013) velocity field. [f]Reference velocity field into which all others are aligned.

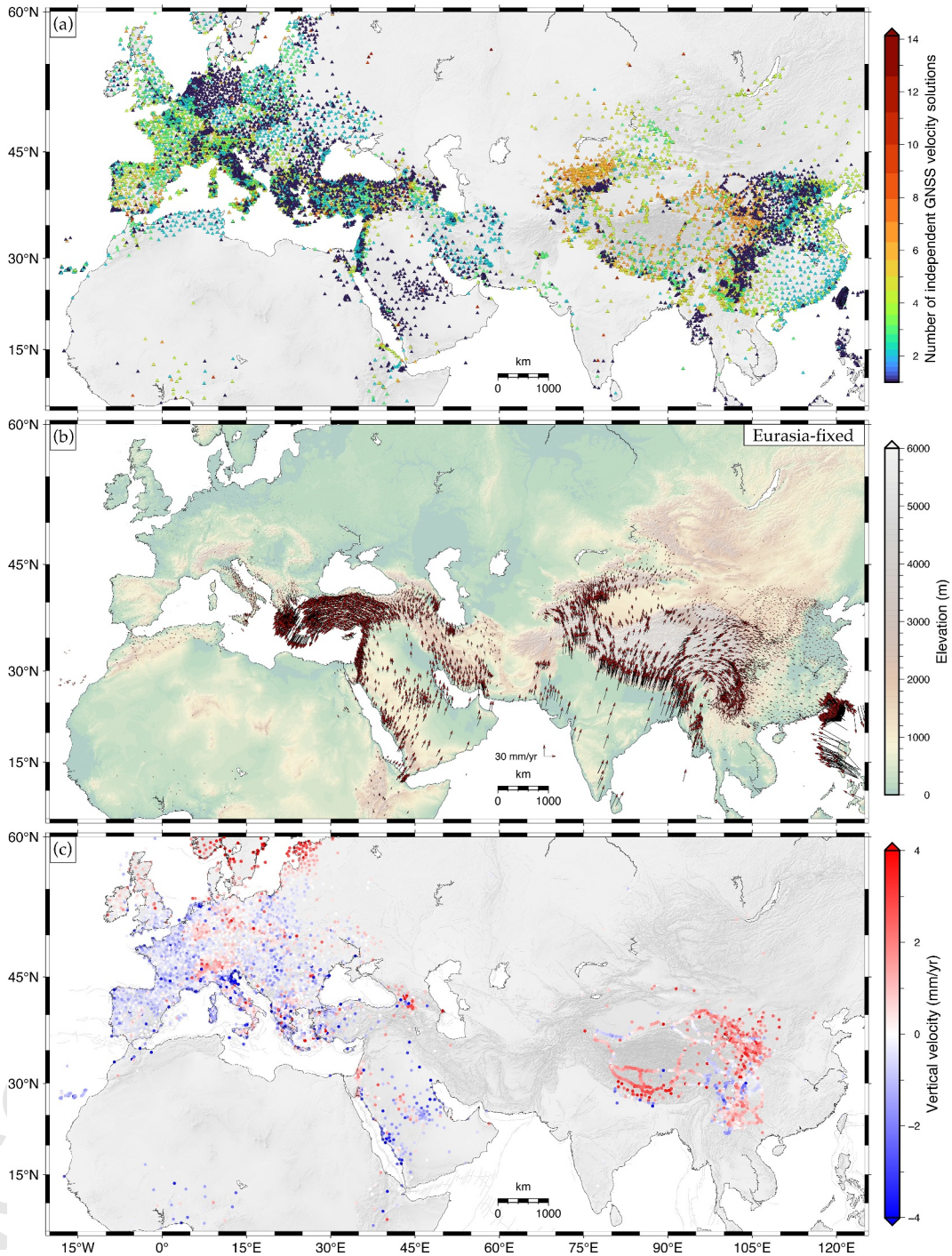


**Figure 2.** (a) Number of independent horizontal velocity solutions at each GNSS station. (b) Combined horizontal GNSS velocity field expressed in a Eurasia-fixed reference frame. (c) Combined vertical GNSS velocity field (red: uplift, blue: subsidence).

$\dot{\boldsymbol{R}} = \left(\dot{R}_x, \dot{R}_y, \dot{R}_z\right)$, fixing the scale-rate parameter ($\dot{s}$) to zero. The translation- and rotation-rate vectors were estimated using a weighted least-squares inversion that minimizes horizontal velocity differences at common GNSS sites between the input and target velocity fields. The transformation of each input GNSS velocity field into the ITRF2014 (no-net-rotation) reference frame (Altamimi et al., 2017) is given by

**Table 2**
*Euler Poles Used to Rotate the Combined Horizontal GNSS Velocity Field*

| Plate | $\omega_x$ ($^\circ Myr^{-1}$) | $\omega_y$ ($^\circ Myr^{-1}$) | $\omega_z$ ($^\circ Myr^{-1}$) | Lat | Lon | $\omega$ ($^\circ Myr^{-1}$) | Source | Map |
|---|---|---|---|---|---|---|---|---|
| Eurasi[a] | −0.023500 | −0.147600 | 0.214000 | 55.07 | −99.05 | 0.26102 | Altamimi et al. (2017) | Figure 2b |
| Arabia[a] | 0.328400 | −0.035040 | 0.406820 | 50.93 | −6.09 | 0.52400 | Viltres et al. (2022) | Figure S3a in Supporting Information S1 |
| Nubia[a] | 0.027400 | −0.170400 | 0.203700 | 49.73 | −80.87 | 0.26698 | Altamimi et al. (2017) | Figure S3b in Supporting Information S1 |
| East Anatolia[a] | 1.008722 | 0.543127 | 1.020384 | 1.01 | 0.54 | 1.02038 | Ergintav et al. (2023) | Figure S3c in Supporting Information S1 |
| West Aegean[a] | 0.050898 | 0.147426 | 0.158303 | 45.43 | 70.95 | 0.22223 | Ergintav et al. (2023) | Figure S4a in Supporting Information S1 |
| Sinai[a] | 0.242500 | −0.047970 | 0.349390 | 54.72 | −11.19 | 0.42800 | Hamiel and Piatibratova (2021) | Figure S4b in Supporting Information S1 |
| India[a] | 0.320500 | −0.001400 | 0.403800 | 51.56 | −0.25 | 0.51554 | Altamimi et al. (2017) | Figure S4c in Supporting Information S1 |
| Amuria[a] | −0.048000 | −0.107140 | 0.274140 | 66.82 | −114.13 | 0.29822 | This study[b] | Figure S5a in Supporting Information S1 |
| South China[a] | −0.057800 | −0.127200 | 0.293300 | 64.53 | −114.45 | 0.32490 | Vardić et al. (2022) | Figure S5b in Supporting Information S1 |
| Central Tibet[a] | 0.129830 | −0.713600 | −0.023360 | −1.84 | −79.69 | 0.72569 | This study[c] | Figure S5c in Supporting Information S1 |

[a]Relative to the International Terrestrial Reference Frame 2014 (ITRF2014, Altamimi et al., 2017). [b]Estimated using three GNSS stations within the Amurian plate (see Figure S6a and S6b in Supporting Information S1 for details). [c]Estimated using five GNSS stations in central Tibet (see Figure S6c and S6d in Supporting Information S1 for details). Although the Tibetan Plateau undergoes internal deformation and this reference frame holds no geological significance, it effectively highlights the E−W extension within the plateau, as noted by Gan et al. (2007).

$$\mathbf{V}_{\mathrm{ITRF2014}} = \mathbf{V}_{\mathrm{input}} + \dot{\mathbf{T}} + \dot{\boldsymbol{R}} \times \mathbf{X} + \dot{s}\mathbf{X}, \quad (1)$$

where $\mathbf{V}_{\mathrm{input}}$ and $\mathbf{V}_{\mathrm{ITRF2014}}$ are the velocity vectors in the original and target reference frames, respectively, and $\mathbf{X} = (X, Y, Z)$ is the station position vector (see Appendices A1 and A2 in Altamimi et al., 2002). All input GNSS velocity fields listed in Table 1 were aligned to the velocity field of Serpelloni et al. (2022), expressed in the International GNSS Service (IGS) realization of the ITRF2014 reference frame (IGB14). Our implementation of this six-parameter Helmert transformation of GNSS velocities follows the same approach adopted in previous regional and global GNSS velocity combinations (e.g., Gomez et al., 2020; Graham et al., 2018; Kreemer et al., 2006, 2009; Mallick et al., 2020; Piña-Valdés et al., 2022; Serpelloni et al., 2022). The alignment statistics, including RMS alignment residuals and the number of common GNSS stations used for each transformation, are provided in Table 1. The consistently low RMS residuals demonstrate the quality of the transformation to ITRF2014 across all input GNSS velocity fields, with a mean RMS alignment residual of 0.5 ± 0.3 mm yr$^{-1}$.

5. *Rotating input velocity fields to different reference frames:* To aid visual inspection, tectonic interpretation, and subsequent manual filtering, we rotated input GNSS velocity fields, already aligned to ITRF2014, into various reference frames, including Eurasia, Nubia, India, East Anatolia, Arabia, Amuria, Yangtze (South China), Central Tibet, and Aegean-fixed reference frames, using the Euler poles listed in Table 2.
6. *Filtering by velocity magnitude and azimuthal direction:* We applied an Interquartile Range (IQR) method to assess the spread of velocity magnitudes and azimuthal directions at colocated stations where multiple velocities were reported by previous studies. Velocities falling below $Q_1 - 1.5 \times IQR$ or above $Q_3 + 1.5 \times IQR$ were considered outliers and subsequently removed, where $Q_1$ and $Q_3$ represent the first and third quartile, respectively. This approach was inspired by Zeng (2022), who filtered velocities that deviated by more than 20% in magnitude or azimuth from neighboring stations.
7. *Combining velocity fields:* Our approach for combining GNSS velocity fields builds on the method proposed by Zeng (2022), which averages velocity components for colocated stations and estimates uncertainties as the square root of the sum of averaged squared uncertainties from multiple studies. In our approach, instead of using the arithmetic mean, we computed the median velocities and uncertainties for colocated stations within a 0.01° (∼1.1 km) radius, as the median is less sensitive to outliers. Figure 2a shows the number of independent velocity observations used to compute the median horizontal velocity at each GNSS station. Vertical velocities were processed separately due to the limited availability of vertical rates in many previous studies, resulting in a less comprehensive data set. To improve the vertical velocity field, we incorporated leveling

data from Wu et al. (2022) for the Tibetan Plateau and the India-Asia collision zone, which had already been aligned through a Helmert joint adjustment with regional continuous GNSS stations. To ensure robustness, we removed vertical velocities that deviated by more than $2\sigma$ from the mean or exceeded the 99th percentile of the lognormal fit to the vertical uncertainty distribution, effectively filtering out outliers. However, vertical rates were not adjusted using a Helmert transformation and are provided as a separate data set for completeness and future use. Vertical velocities are not used in our strain rate inversions, as we estimate the 2D strain rate tensor field solely from the combined horizontal GNSS velocities.

8. *Manual filtering:* We applied a manual filtering step to refine the combined velocity field, identifying outliers missed in previous filtering steps and stations affected by volcanic transient motions and anthropogenic sources. GNSS stations impacted by the Groningen gas field and volcanic activity at Campi Flegrei, Vesuvius, Etna, Afar, Santorini, and the Aeolian Islands were specifically excluded.
9. *Scaling velocity uncertainties:* We scaled horizontal velocity uncertainties in the combined velocity field using the method of Piña-Valdés et al. (2022), which assumes GNSS velocity uncertainties follow a log-normal distribution. The uncertainties were adjusted to match the same percentile in a subjectively chosen target log-normal distribution. Here, we used the velocity uncertainty distribution of Wang and Barbot (2023), which has a mean close to 1 mm/yr for East and North velocity uncertainties, as shown in Figure S2 of Supporting Information S1. This step was implemented to prevent unrealistically low velocity uncertainties, which could disproportionately weight certain stations and lead to improper scaling of the covariance matrix in our weighted least squares inversion for strain rates.
10. *Final filtering based on uncertainty distribution:* We removed stations with velocity uncertainties exceeding the 99th percentile of the scaled log-normal distribution, similar to our second filtering step but this time applied to the combined horizontal GNSS velocity field.

We intentionally included 2,714 additional horizontal GNSS velocities from stations located outside the Alpine-Himalayan belt to serve as tying sites for future global GNSS velocity combinations. This ensures that any future reference frame alignment involving our data set can be performed robustly, as these stations provide broad geographic coverage for such transformations. Additionally, we provide rotated velocity fields in 10 different reference frames, openly available in a public repository (Castro-Perdomo, 2025), to further facilitate their use in future research. Corresponding maps of the rotated horizontal GNSS velocity fields are included in the (Figures S3–S5 in Supporting Information S1).

## 3. Strain Rate Inversion

Given the spatially scattered nature of GNSS velocities, interpolating these data is essential for estimating surface strain rates. Various methodologies have been developed for this purpose, ranging from calculating strain rates using baselines—often through techniques like Delaunay triangulation (e.g., Cai & Grafarend, 2007; Kreemer et al., 2018, 2020; Savage, 1983; Savage et al., 2001)—to employing non-parametric and elastic basis functions to fit surface velocities (e.g., Beavan & Haines, 2001; Haines & Holt, 1993; Haines et al., 2015; Johnson, 2024; Okazaki et al., 2021; Sandwell & Wessel, 2016; Tape et al., 2009). Additionally, methodologies utilizing weighted mean and locally weighted regression have been explored (e.g., El-Fiky & Kato, 1998; Shen et al., 1996, 2015), and recent studies have proposed Bayesian interpolation schemes (e.g., Pagani et al., 2021) and geostatistical approaches based on ordinary kriging (e.g., Maurer & Materna, 2023).

Here, we adopted the body-force method proposed by Johnson (2024), as implemented in the BForStrain MATLAB code (Johnson, 2023). BForStrain interpolates 2D velocity fields using analytical Green's functions for a thin elastic body under in-plane body forces (Sandwell & Wessel, 2016). Velocities and strain rates are estimated at the centroids of triangles within a 2D adaptive triangular mesh generated using MESH2D, a Delaunay mesh-generator by Engwirda (2009), whose resolution is refined based on the GNSS station density. BForStrain enables uncertainty estimation through linear error propagation of GNSS velocity uncertainties and posterior sampling across a range of regularization parameters. Notably, it also allows for velocity discontinuities across predefined creeping faults, which are conflated with strain in most of the other methods.

Our strain rate inversions solve for the distribution of body forces at the vertices of a triangular mesh and surface creep rates on faults that best fit the observed geodetic surface velocities $v_{obs}$. The regularized weighted least squares formulation can be expressed as:

$$\begin{bmatrix} \Sigma_v^{-\frac{1}{2}} v_{\text{obs}} \\ \alpha c \\ 0 \end{bmatrix} = \begin{bmatrix} \Sigma_v^{-\frac{1}{2}} G_v & \Sigma_v^{-\frac{1}{2}} G_c \\ 0 & \alpha I \\ \beta I & 0 \end{bmatrix} \begin{bmatrix} f \\ s_c \end{bmatrix}, \tag{2}$$

where $\Sigma_v$ represents the covariance matrix of the observed velocities, $I$ is the identity matrix, and $G_v$ and $G_c$ are matrices of Green's functions for body forces and fault creep rates, respectively. The objective is to solve for the body forces and fault creep rates ($f$ and $s_c$) that minimize the residual between observed and predicted surface velocities, subject to Tikhonov regularization constraints ($\alpha$ and $\beta$) on surface creep rates and body-force magnitudes, respectively.

Upon solving the linear system in Equation 2, we aim to calculate the full posterior probability distribution for the estimated strain rates. This involves computing the predicted strain rates, $\varepsilon_\beta$, from the best-fitting model of body forces and surface creep rates and then deriving their covariance, $\Sigma_{\varepsilon,\beta}$, to quantify uncertainties. The posterior probability distribution for the strain rates, given the observed data $d$ and regularization parameter $\beta$, can be expressed as:

$$p(\varepsilon|d,\beta) = \frac{1}{\left[(2\pi)^k |\Sigma_{\varepsilon,\beta}|\right]^{\frac{1}{2}}} \exp\left(-\frac{1}{2}(\varepsilon - \varepsilon_\beta)^\top \Sigma_{\varepsilon,\beta}^{-1} (\varepsilon - \varepsilon_\beta)\right). \tag{3}$$

To encapsulate uncertainty in the body force damping $\beta$, we approximated the posterior distribution $p(\varepsilon|d)$ by drawing 500 random samples from Equation 3 for each $\beta$ value, representing altogether discrete realizations of the posterior distribution $p(\varepsilon|d)$, following the same procedure implemented by Johnson (2024). We then evaluated the solution's smoothness and fit across a range of damping parameters, with L-curves provided in the Supporting Information S1 to support our subjective damping choices (Figure S7 in Supporting Information S1). The damping parameter $\alpha$ controlling surface creep rates was selected subjectively to ensure that the model neither overfits nor underfits observed GNSS velocities across well instrumented creeping faults. Finally, strain rates are computed from the inverted model solution of body forces and surface creep rates ($f$ and $s_c$) and analytical Green's functions ($G_\varepsilon, G_{c,\varepsilon}$) relating those to strain rates, for a particular $\beta$ value:

$$\varepsilon_\beta = G_\varepsilon f_\beta + G_{c,\varepsilon} s_{c\beta}. \tag{4}$$

We conducted three strain rate inversions. The first one aimed to capture large-scale deformation patterns and identify regions with the highest deformation rates along the entire Alpine-Himalayan belt (Figure 3). This inversion applied moderate body-force damping constraints to emphasize broad-scale strain rate features, without estimating posterior uncertainties or surface creep rates. Based on these results, we selected two regions for detailed analysis: the eastern Mediterranean and the India-Asia collision zone, both characterized by high strain rates and dense GNSS station coverage. For these regions, we performed focused inversions using refined triangular meshes to resolve finer-scale deformation features, as discussed in Section 4.

In these focused inversions, we estimated posterior uncertainties by drawing 3,000 samples from the posterior distribution, utilizing six damping parameters near the L-curve elbows to balance model smoothing and fit to observed GNSS velocities. To further regularize our least squares inversion, we incorporated priors on fault creep rates in the eastern Mediterranean based on creep rate estimates from previous geodetic studies along select fault segments. Specifically, we included shallow creep rate priors from the Izmit and İsmetpaşa segments of the North Anatolian fault (Aslan et al., 2019; Cakir et al., 2005; Cetin et al., 2014; Hussain et al., 2016; Kaneko et al., 2013; Kurt et al., 2023; Özarpacı et al., 2021), the Marmara segment of the North Anatolian Fault (Yamamoto et al., 2019), the Palu segment of the East Anatolian fault (Bletery et al., 2020; Cakir et al., 2023; Cavalié & Jónsson, 2014), and the northern segment of the Jordan Valley fault located south of the Sea of Galilee, where shallow fault creep has been reported (Hamiel et al., 2016; Hamiel & Piatibratova, 2021).

Considering that the method proposed by Johnson (2024) estimates strain rates in a Cartesian coordinate system, evaluating distortion effects across the continental-scale Alpine-Himalayan belt is crucial. To this end, we generated a synthetic Euler-pole-predicted velocity field over the entire belt using an equidistant grid with a

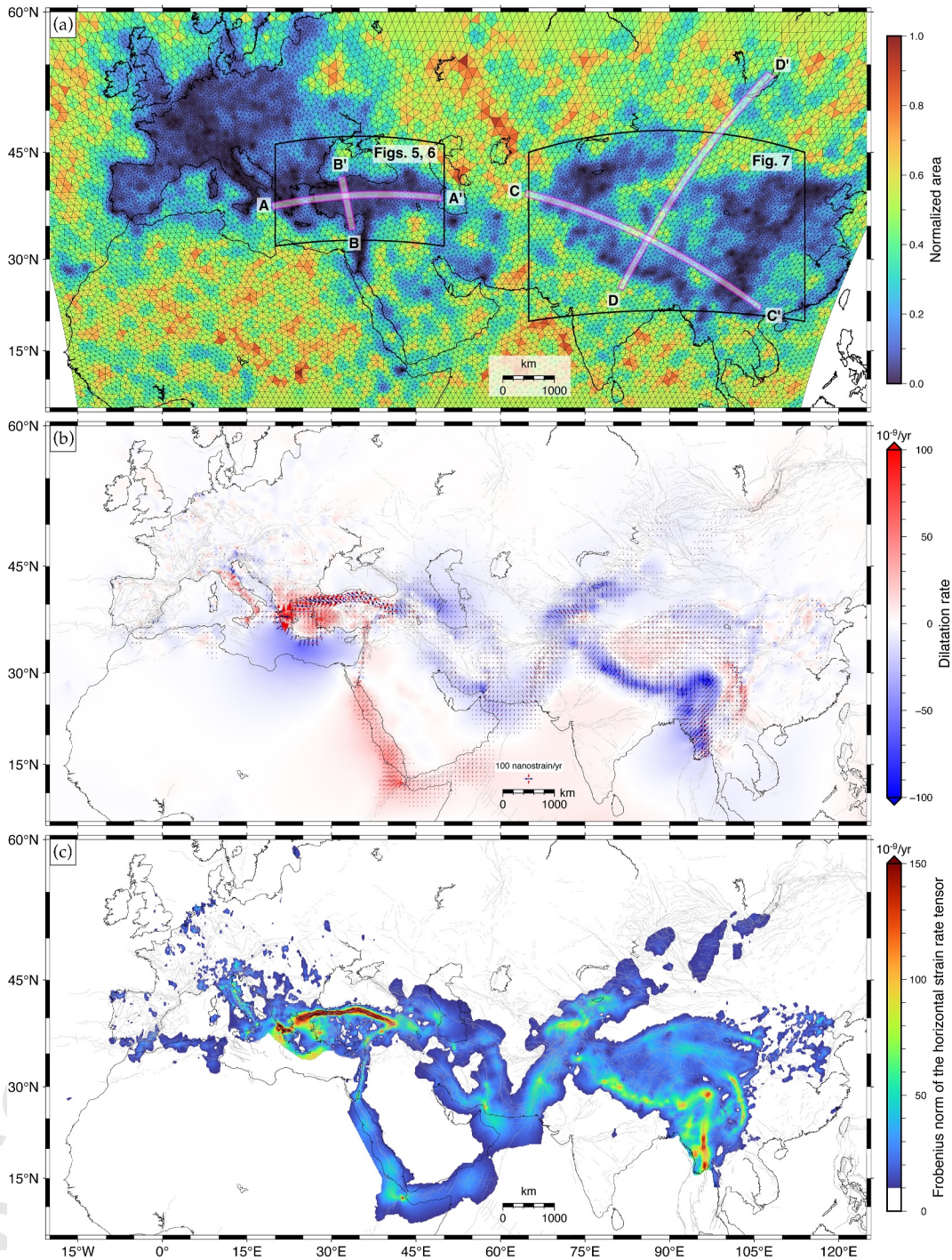


**Figure 3.** (a) Triangular mesh used in the large-scale strain rate inversion, with a nominal node spacing of 100 km in regions with sparse GNSS coverage (warmer colors) and refined to ~15 km in well-instrumented areas (cooler colors). The locations of four profiles shown in Figure 4, are also indicated. (b) First invariant of the strain rate tensor (dilatation rate) with principal strain rate directions plotted on a 0.75° equidistant grid. Red indicates extension, while blue represents contraction. (c) Strain rate, with a lower threshold of 10 nanostrain/yr to emphasize the main deformation belts and shear zones. We applied a mask to suppress strain rate bleeding artifacts in poorly instrumented regions and over water bodies, including the Mediterranean Sea, western Red Sea borderlands, Indian Ocean, Bay of Bengal, and South China Sea (see Figure S10 in Supporting Information S1).

$1° \times 1°$ spacing and inverted this synthetic velocity field to estimate strain rates, applying the same body force damping parameters used in our large-scale inversion (Figure S8 in Supporting Information S1). The purpose of this test is to isolate distortion artifacts: since the synthetic Euler-pole-predicted velocity field represents purely rigid body rotations, any nonzero strain rates estimated far from tectonic plate boundaries can be attributed to coordinate system distortions rather than true deformation.

Our analysis revealed that strain rates resulting from distortion effects are small, remaining below 5 nanostrain/yr. Faster-moving plates such as India and Arabia exhibit the largest distortion effects, which increase with the angular distance from each plate's Euler pole. Additionally, distortion more significantly impacts the magnitude of dilatation rates compared to the second invariant and maximum shear strain rates. Furthermore, distortion effects are spatially systematic and intensify with latitude, becoming more pronounced near the geographic poles, a factor not highlighted in our test due to our use of a Eurasia-fixed reference frame for the GNSS velocities. Further details on our test for distortion effects are provided in Figure S8 of Supporting Information S1.

Several scalar measures can be used to characterize the strain rate tensor, often expressed in terms of its invariants or eigenvalues (see Appendix A). In this study, we adopt two widely used scalar quantities: the first invariant ($I_1^{2D}$, dilatation rate) and the Frobenius norm of the 2D horizontal strain rate tensor ($\|\dot{\varepsilon}\|_F^{2D}$), defined as:

$$I_1^{2D}\left(\dot{\varepsilon}\right) = \dot{\Delta} = \mathrm{tr}\left(\dot{\varepsilon}\right) = \dot{\varepsilon}_{11} + \dot{\varepsilon}_{22} = \dot{\varepsilon}_1 + \dot{\varepsilon}_2, \tag{5}$$

$$\|\dot{\varepsilon}\|_F^{2D} = \sqrt{\sum_{i,j} \dot{\varepsilon}_{ij}^2} = \sqrt{\dot{\varepsilon} : \dot{\varepsilon}} = \sqrt{\mathrm{tr}\left(\dot{\varepsilon}^2\right)} = \sqrt{\dot{\varepsilon}_{11}^2 + \dot{\varepsilon}_{22}^2 + 2\dot{\varepsilon}_{12}^2}. \tag{6}$$

For clarity, throughout this paper we refer to the Frobenius norm of the 2D horizontal strain rate tensor as "strain rate" (e.g., Tape et al., 2009). Note that for the deviatoric strain rate tensor $\dot{\varepsilon}'$, the Frobenius norm is directly related to the deviatoric second invariant, $\|\dot{\varepsilon}'\|_F = \sqrt{2J_2}$, which in two dimensions is equivalent to $\|\dot{\varepsilon}'\|_F^{2D} = \sqrt{2}\,\dot{\gamma}_{\max}^{2D}$, where $\dot{\gamma}_{\max}^{2D} = \sqrt{J_2} = \frac{1}{2}\left(\dot{\varepsilon}_1 - \dot{\varepsilon}_2\right)$ denotes the maximum shear strain rate.

## 4. Velocity and Strain Rate Fields

### 4.1. Combined Horizontal GNSS Velocity Field

The horizontal velocity field relative to Eurasia (Figure 2b) reveals coherent large-scale motions that underscore the region's active tectonics and geodynamics, which have been extensively studied over the past 50 years (e.g., Barbot & Weiss, 2021; Becker & Faccenna, 2011; Faccenna, Becker, Auer, et al., 2014; Hatzfeld & Molnar, 2010; Jackson & McKenzie, 1984; Jolivet et al., 2013, 2018; Kreemer et al., 2014; McClusky et al., 2000; McKenzie, 1978; Molnar & Tapponnier, 1975; Nocquet, 2012; Palano, 2014; Reilinger et al., 2006; Şengör, 1986; Wang & Shen, 2020; Wang & Barbot, 2023). Notable large-scale features include the counterclockwise rotation of Arabia, western Iran, Anatolia, and the Aegean (e.g., McClusky et al., 2000; Reilinger et al., 2006); the acceleration of Anatolia toward the Hellenic Trench, likely driven by trench retreat and slab rollback (e.g., Faccenna, Becker, Auer, et al., 2014; Le Pichon & Angelier, 1979; Reilinger et al., 2006; Royden, 1993); and lateral escape tectonics on both flanks of the Tibetan Plateau as a result of the India-Asia collision (Tapponnier et al., 1982; Wang & Shen, 2020).

Additionally, the horizontal velocity field in a Eurasia-fixed reference frame reveals a clockwise rotation around the eastern Himalayan syntaxis in Southeast Asia (e.g., Hatzfeld & Molnar, 2010; Holt et al., 1991; Sol et al., 2007; Tapponnier et al., 1982; Wang & Shen, 2020; Yin & Harrison, 2000). Several mechanisms have been invoked to explain deformation patterns observed in this complex region, including crustal and mantle flow driven by gravitational potential energy (GPE) release from the Tibetan Plateau (e.g., Bai et al., 2010; He et al., 2021; Molnar & Lyon-Caen, 1988; Royden et al., 1997; Shen et al., 2001; Timsina et al., 2024), localized flow due to partial melting (Sun et al., 2025), and the possible influence of slab rollback (e.g., Hou et al., 2024; León Soto et al., 2012; Shen et al., 2001).

### 4.2. Combined Vertical GNSS Velocity Field

The vertical velocity field illustrated in Figure 2c also displays coherent regional and large-scale tectonic and geodynamic signatures. Notable features include the well-documented uplift in the Fennoscandian Peninsula, with vertical rates reaching ∼10 mm/yr, attributed to glacial isostatic adjustment (GIA) following the Late Pleistocene glaciation (e.g., Johansson et al., 2002; Milne et al., 2001; Nocquet, 2012). Additionally, ∼1 mm/yr uplift rates are observed in the Eifel volcanic field in Germany, linked to a buoyant mantle plume (Kreemer et al., 2020; Ritter et al., 2001; Walker et al., 2005), and 1–2.5 mm/yr uplift rates are recorded along the Alps (e.g., Nocquet et al., 2016; Piña-Valdés et al., 2022; Serpelloni et al., 2022). These uplift rates are interpreted to result from a mix of processes, with contributions from shortening (e.g., van Gelder et al., 2017), erosion (e.g., Kuhlemann et al., 2002), isostatic rebound after the last deglaciation (e.g., Mey et al., 2016), slab detachment (e.g., Fox et al., 2015; Sue et al., 1999; Wortel & Spakman, 2000), and Eurasia-Adria subduction (e.g., Brückl et al., 2007; Lippitsch et al., 2003), as discussed by Sternai et al. (2019).

Further features of the vertical velocity field include widespread subsidence in the Po Basin, with rates exceeding 5 mm/yr. This subsidence is driven by a combination of anthropogenic sources (e.g., groundwater extraction), Adriatic slab retreat, and compaction of alluvial deposits (e.g., Carminati et al., 2003; Serpelloni et al., 2013; Tosi et al., 2013). In contrast, the central Apennines exhibit both uplift and positive dilatation rates (see Figure S9 in Supporting Information S1), consistent with active mantle flow in a slab gap and recent orogeny (Faccenna, Becker, Miller, et al., 2014; Serpelloni et al., 2013; Shaw & Pysklywec, 2007).

Systematic uplift is also evident along the Levant, where vertical rates reach up to ∼2 mm/yr (e.g., Serpelloni et al., 2013; Serpelloni et al., 2022), associated with the activity of the Dead Sea Fault (e.g., Gomez et al., 2006, 2020; Ten Brink et al., 1990). Finally, the vertical velocity field highlights both widespread uplift across the Tibetan Plateau and subsidence along its southeastern flank around the eastern Himalayan syntaxis (Y. Wu et al., 2022). Observed uplift rates ranging from ∼1 to ∼4 mm/yr have been attributed to vertical crustal thickening driven by the India-Asia collision (e.g., England & Houseman, 1986; S. Liu et al., 2025; Molnar et al., 1993), while the 0.5–3.5 mm/yr subsidence rates in the southeast have been interpreted as a consequence of crustal flow and gravitational collapse (Y. Wu et al., 2022).

### 4.3. Strain Rate Field

Continental-scale strain rate maps and profiles across sections of the Alpide belt are presented in Figures 3 and 4. To enhance the readability of our strain rate maps, we regridded the strain rate tensor components from the original triangular meshes to an equidistant grid with $0.1° \times 0.1°$ spacing using linear interpolation. Regional-scale strain rate features derived from our combined velocity field align with previous studies (e.g., Kreemer et al., 2014; Lindsey et al., 2023; Y. Li et al., 2025; Piña-Valdés et al., 2022; Serpelloni et al., 2022; Weiss et al., 2020; Wang & Shen, 2020; Wang & Barbot, 2023), although differences in strain rate magnitudes are observed. These discrepancies are primarily due to the significant recent expansion of GNSS networks—particularly in the eastern Mediterranean, northern Africa and the India-Asia collision zone—and the inherent non-uniqueness of strain rate estimates. The increased GNSS station density in these regions has substantially improved resolution compared to earlier GNSS-derived strain rate models.

Below, we discuss key features observed in the velocity and strain rate fields for the eastern Mediterranean and the India-Asia collision zone. These regions were selected due to their dense GNSS station coverage, which has improved significantly with the addition of over 2,000 new stations in recent years (Kurt et al., 2023; Y. Li et al., 2025; Wang & Shen, 2020), and the presence of high strain rate belts, such as those in Anatolia, Tibet, Himalayas, and the southeast borderland of the Tibetan Plateau. For these areas, we performed additional strain rate inversions using finer triangular meshes, with a nominal spacing of 100 km in regions with sparse GNSS coverage, refined to approximately 5 km in areas with dense instrumentation. Unlike our large-scale inversion, where we prioritized regional trends by subjectively selecting a range of body-force damping parameters ($\beta$) that produce a smooth strain rate field, these focused inversions applied an L-curve method to identify a range of damping parameters within the elbow of the L-curve, optimizing the balance between model roughness and fit to the data. Consequently, the refined strain rate estimates presented below have higher resolution and exhibit greater magnitudes in highly deforming regions compared to those from our broader-scale inversion. Moreover, unlike our large-scale inversion, we compute and display posterior uncertainties for the refined strain rate estimates, as shown in Figure S14 of Supporting Information S1.

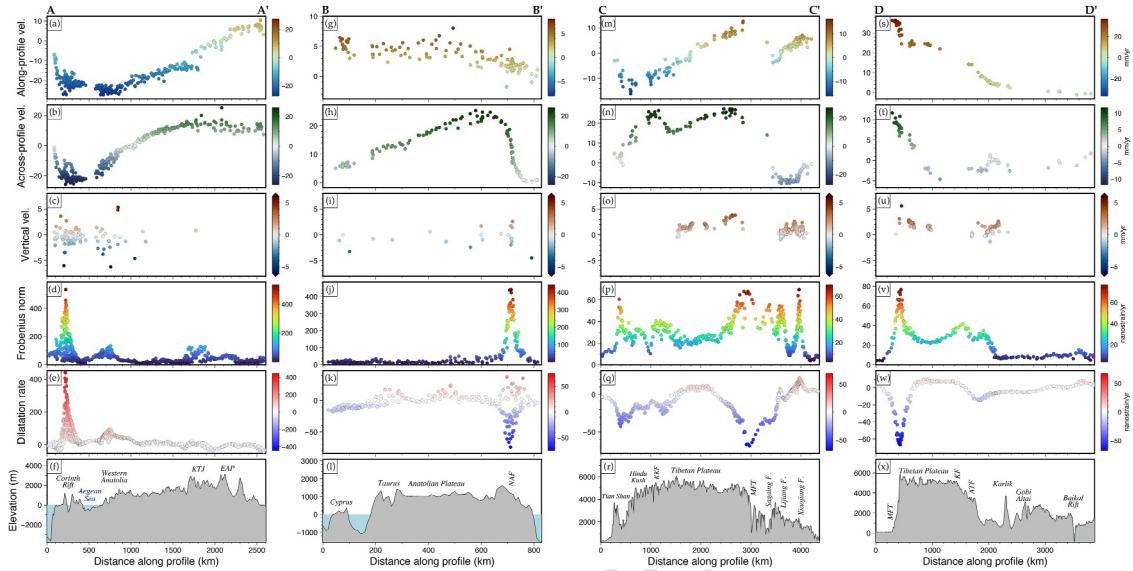


**Figure 4.** Profiles of GNSS velocities in a Eurasia-fixed reference frame, strain rates, and topography across various sections of the Alpine-Himalayan belt. Profile locations are shown in Figure 3a. From top to bottom, the rows display along-profile velocity, across-profile velocity, vertical velocity, strain rate, dilatation rate, and elevation. Profile A-A′ spans from the Adriatic Sea to the Caspian Sea. Profile B-B′ extends from Cyprus to the Black Sea. Profile C-C′ traverses from the Tian Shan to Southeast Asia. Profile D-D′ runs from the Indo-Gangetic Plain to the Baikal Rift. Additional profiles along other sections of the Alpide belt are shown in Figures S11–S13 in Supporting Information S1. KTJ, Karliova Triple Junction; EAP, Eastern Anatolia Plateau; NAF, North Anatolian Fault; KKF, Karakorum Fault; MFT, Main Frontal Trust; KF, Kunlun Fault; ATF, Altyn Tagh Fault.

#### 4.3.1. Eastern Mediterranean

Figure 5 presents the results of our refined strain rate inversion for the eastern Mediterranean region. Panel (a) displays the GNSS velocity field in the East Anatolia-fixed reference frame from Ergintav et al. (2023), highlighting the pronounced N-S extension in western Anatolia—a feature that is less evident in the commonly used Eurasia-fixed reference frame. This reference frame also emphasizes the right-lateral North Anatolian Fault, where slip rates range from ∼20 to ∼30 mm/yr, increasing westward (e.g., Ergintav et al., 2023; Hussain et al., 2018; Kurt et al., 2023; Le Pichon & Kreemer, 2010; McClusky et al., 2000; Reilinger et al., 2006). Additionally, the velocity field reveals <10 mm/yr of left-lateral motion between the Anatolian and Arabian plates along the East Anatolian Fault (e.g., Güvercin et al., 2022), with negligible fault-perpendicular velocities. This observation, first noted by Reilinger et al. (2006), was cited as evidence against the extrusion hypothesis as the primary driver of Anatolia's motion (Şengör et al., 1985), instead supporting an alternative model in which deformation is primarily controlled by slab rollback and trench retreat (e.g., Faccenna et al., 2006; Heidbach, 2005; Le Pichon & Angelier, 1979; Malinverno & Ryan, 1986; McKenzie & Yılmaz, 1991; Royden, 1993).

Panel (b) in Figure 5 illustrates the triangular mesh used in the refined strain rate inversion, with higher resolution applied in densely instrumented areas and along creeping fault segments. Well-instrumented regions include most of the Anatolian Plate, the Peloponnese, Crete, northern Cyprus, and the Levant. In contrast, areas with sparse GNSS coverage include Libya in north Africa, the northern Arabian Plate across Syria and Iraq, and the region north of the Greater Caucasus near the Caspian Sea. Panel (c) presents a map of dilatation rates and principal strain rate directions, illustrating a transition from E-W extension in central Anatolia to N-S extension across the western Anatolia extensional province. Principal strain directions also delineate a shear belt extending offshore from the North Anatolian Fault into the North Aegean Sea along the North Aegean Trough (e.g., Flerit et al., 2004; Rodriguez et al., 2023), which widens westward, consistent with recent results by Chousianitis et al. (2024), as shown in Figures 5c and 5d. The southwestern Aegean exhibits low strain rates (<10 nanostrain/yr), supporting previous studies suggesting that portions of the southwestern Aegean Sea behave as a relatively rigid block (e.g., Kreemer & Chamot-Rooke, 2004; McClusky et al., 2000). Additionally, mild extension (10–20 nanostrain/yr) is observed across parts of the south central Taurus Mountains, as depicted in profile B-B′ in Figure 4.

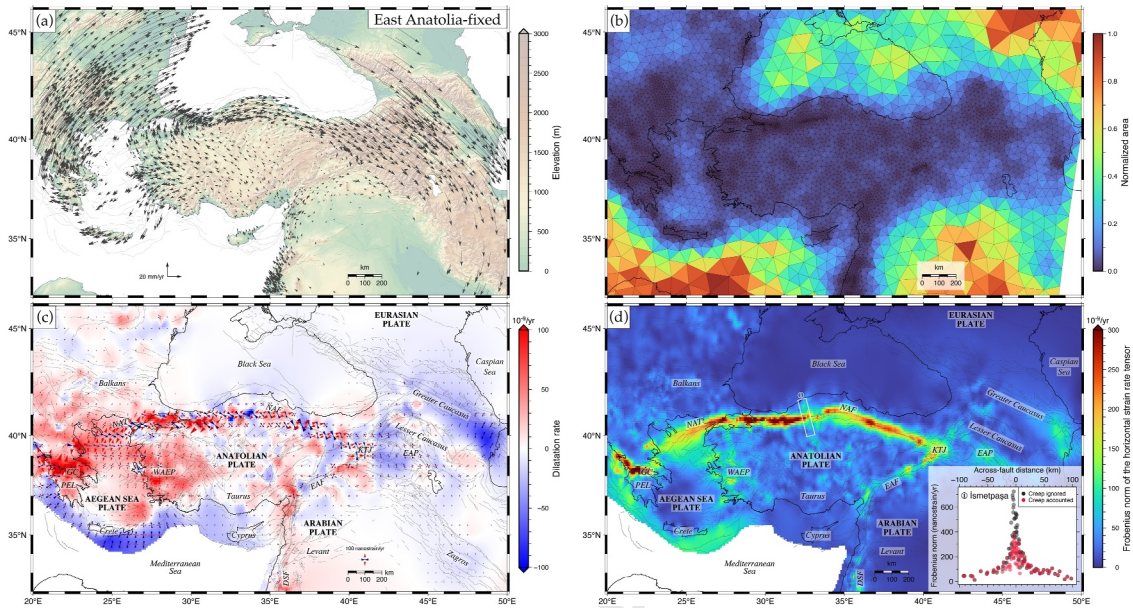


**Figure 5.** (a) GNSS velocity field rotated into the East Anatolia-fixed reference frame from Ergintav et al. (2023), highlighting the transition from E-W extension in central Anatolia to N-S extension in western Anatolia. (b) Triangular mesh used for strain rate inversion, color-coded by normalized triangle area. (c) Dilatation rate (first invariant) and principal strain rate directions (red: stretching, blue: shortening). Principal strain rate directions are shown only at locations where the strain rate is larger than 10 nanostrain/yr. (d) Strain rate. The panel in the bottom right compares modeled strain rates from inversions that accounted (red dots) and ignored (dark gray dots) the contribution of surface creep to strain rates along a profile crossing the İsmetpaşa segment of the North Anatolian Fault, as indicated by the white box on the map. PEL, Peloponnese; GC, Gulf of Corinth; WAEP, Western Anatolian Extensional Province; NAT, North Aegean Trough; NAF, North Anatolian Fault; EAF, East Anatolian Fault; KTJ, Karliova Triple Junction; EAP, Eastern Anatolian Plateau.

Although GNSS station coverage in the Caucasus region is sparser than in Anatolia, our results reveal a west-to-east transition from predominantly N-S to NNE-SSW shortening across the Greater Caucasus, with strain rates increasing toward the Caspian Sea, exceeding 60 nanostrain/yr. In contrast, the Lesser Caucasus exhibits localized, discontinuous zones of extension and shortening, with principal strain directions indicating a combination of strike-slip motion, NW-SE shortening, and NE-SW extension (see Figure 5c). These findings align with geological studies documenting the complex coexistence of compressional and extensional structures (e.g., Rebaï et al., 1993) and evidence of syn- and post-collisional magmatism (Ismail-Zadeh et al., 2020, and references therein). Similarly, our results agree with early block model interpretations by Reilinger et al. (2006), which, despite being based on a more limited GNSS velocity data set, inferred small fault-normal extension within the Lesser Caucasus and south of the Caspian Sea (see their Figures 9b, 9c, and 11). However, a denser GNSS network is needed to confirm these observations.

Panel (d) in Figure 5 highlights strain rates in Anatolia, revealing along-strike variations in strain rates along the NAF. These variations align with findings by Liu and Wang (2023), who reported a potential link between elevated strain rates, surface creep, and earthquake ruptures over the past century, starting with the 1939 $M_W$7.8 Erzincan Earthquake. Along-strike strain rate variations were also noted by Weiss et al. (2020), although they emphasized biases due to sparse GNSS station coverage prior to the recent expansion of the GNSS network in Türkiye (Ergintav et al., 2023; Kurt et al., 2023). If these variations reflect afterslip-related surface creep, they suggest that interseismic velocity fields in Anatolia could be influenced by long-term postseismic afterslip transients, as documented along the Izmit rupture 20 years after the 1999 earthquake (Özarpacı et al., 2021). Furthermore, InSAR data and stress-driven afterslip models suggest that postseismic afterslip along the creeping segment of the East Anatolian Fault (EAF) could persist for several decades (>50 years) following the 2023 Kahramanmaraş earthquake doublet (Z. Liu et al., 2025). However, the origin and time-dependent evolution of surface creep along various segments of the NAF and EAF remain debated (e.g., Bilham et al., 2016; Çakir et al., 2012; Cetin et al., 2014; Jolivet et al., 2023; Kaneko et al., 2013; Liu et al., 2025).

The study by Özarpacı et al. (2021) also reported that current locking depths along the Izmit segment of the NAF are significantly shallower than pre-earthquake estimates, attributing this reduction to afterslip. However, given

that transient signals observed in GNSS velocity profiles extend up to 70 km from the fault, viscoelastic mantle relaxation cannot be ruled out as a contributing factor, as proposed by earlier studies (e.g., DeVries et al., 2017; Ergintav et al., 2009; Hearn et al., 2009; Wang et al., 2009). If ongoing postseismic viscoelastic relaxation is confirmed, it would challenge the hypothesis by Hussain et al. (2018), which proposed a short-lived postseismic period of approximately 10 years. The discrepancy may arise from Hussain et al. conflating two distinct parameters: the locking depth (16 km) derived from elastic half-space modeling of surface velocities (e.g., Savage & Burford, 1973) and the elastic thickness assumed in layered viscoelastic models (e.g., Savage & Prescott, 1978). Further research incorporating vertical GNSS and InSAR velocities (e.g., Fukuda & Johnson, 2021; Jónsson, 2008; Luo & Wang, 2022) is necessary to better distinguish between the contributions of afterslip and viscoelastic mantle flow along the North Anatolian Fault, which is thought to be underlain by a 50–100 km-wide shear zone in the lower crust and upper mantle (e.g., Barbot & Weiss, 2021; Papaleo et al., 2018; Taylor et al., 2016).

Our results also reveal a shear belt along the East Anatolian Fault (EAF), though strain rates are notably lower than those along the North Anatolian Fault (NAF), typically ranging between 50 and 80 nanostrain/yr, in agreement with previous InSAR- and GNSS-derived strain rate estimates (Özbey et al., 2024; Weiss et al., 2020). Localized elevated strain rates are observed near the epicenter of the 2020 $M_W$ 6.7 Elaziğ earthquake, as also pointed out by Weiss et al. (2020), likely reflecting postseismic transients inadvertently incorporated into prior interseismic velocity fields. Another area of elevated strain rates is the Karlıova triple junction, where strain rates exceed 100 nanostrain/yr. Additionally, increased posterior uncertainties are evident along the main shear belts of the NAF, EAF, DSF, and the Gulf of Corinth, as detailed in Figure S14 of Supporting Information S1.

To assess the quality of our GNSS velocity inversion for strain rates, we compared observed and model-predicted (i.e., mean posterior) GNSS velocities, as shown in Figure 6a. The results indicate excellent agreement, with 80% of residual velocities falling within ±1 mm/yr, as illustrated in the histogram in the bottom right of Figure 6b. We further quantified the spatial coherence in the residual velocities by computing a "systematic misfit index" (e.g., Johnson et al., 2024), defined as the absolute value of the average dot product of normalized residual velocity vectors with their neighbors within a specified radius (∼50 km), which reveals no evidence for regional-scale systematic residuals (Figure 6b). Our model also effectively resolves velocity gradients across closely spaced creeping and locked fault segments where GNSS station density is high. For example, panels 1 and 2 in Figure 6a show that it accurately captures the velocity gradients across the creeping İsmetpaşa segment and the locked Düzce segment of the NAF, separated by 100 km. Panels 1 and 2 in Figure 6a further demonstrate strong correspondence between observed, mean posterior, and predicted fault-parallel velocities from an elastic half-space antiplane dislocation model (e.g., Savage & Burford, 1973; Sandwell, 2022; Weertman & Weertman, 1964), with posterior distributions shown in Figures S16 and S17 in Supporting Information S1.

A key finding from our analysis is that a significant portion of apparent velocity gradients across some faults can be attributed to surface creep, particularly along the Izmit and İsmetpaşa segments of the NAF, where near-fault GNSS station coverage is dense. The inset in the bottom right of Figure 5d compares strain rates from models that either explicitly incorporate or disregard velocity discontinuities due to surface fault creep, revealing that strain rates exceeding 300 nanostrain/yr may be associated with mismodeled strain rates arising from surface creep along the İsmetpaşa segment. This distinction is important because previous strain rate models in Anatolia did not explicitly account for fault creep, thereby failing to capture the velocity discontinuities observed across faults creeping at the surface—a challenge previously highlighted by Weiss et al. (2020). Differentiating between interseismic fault locking and surface creep contributions to surface strain rates is crucial for seismic hazard assessment, as only strain rates from elastic coupling on faults contribute to the energy budget available for future earthquakes.

Finally, Figure 6c presents the distribution of mean posterior shallow creep rates along various fault segments in the eastern Mediterranean, compared with prior distributions from previous geodetic studies (e.g., Aslan et al., 2019; Bletery et al., 2020; Cakir et al., 2005; Cakir et al., 2023; Cavalié & Jónsson, 2014; Cetin et al., 2014; Hamiel et al., 2016; Hamiel & Piatibratova, 2021; Hussain et al., 2016; Kaneko et al., 2013; Kurt et al., 2023; Özarpacı et al., 2021; Yamamoto et al., 2019). Our inversion applied moderate constraints on the prior distribution of surface creep rates, allowing the posterior to vary from the prior but ensuring consistency with existing observations where available. The validity of this approach is demonstrated by the minimal and non-systematic residual GNSS velocities across well-instrumented creeping faults, such as the Izmit and İsmetpaşa segments of

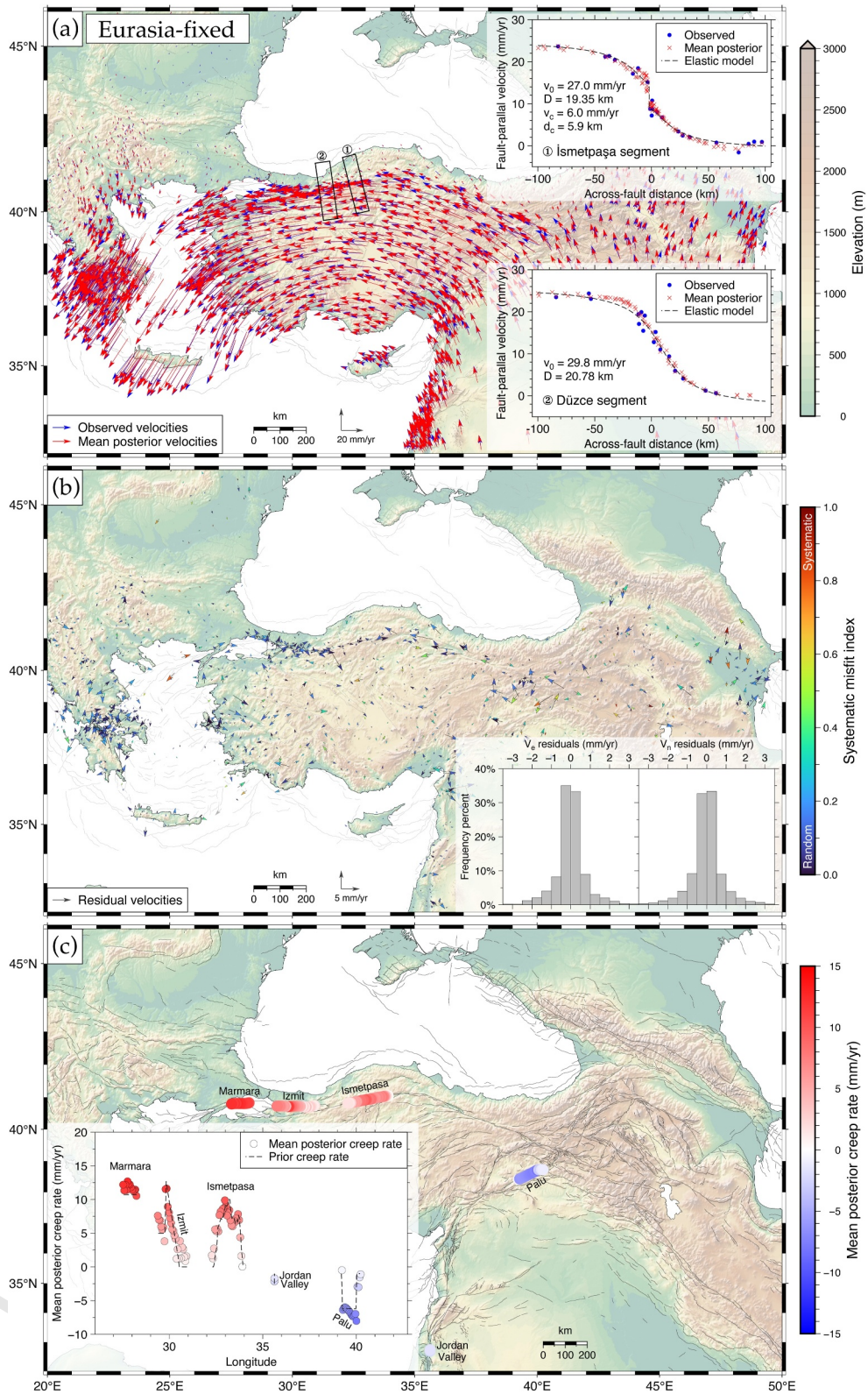
(a) Eurasia-fixed
Observed velocities
Mean posterior velocities
km
0 100 200
20 mm/yr
Observed
Mean posterior
Elastic model
v0 = 27.0 mm/yr
D = 19.35 km
vc = 6.0 mm/yr
dc = 5.9 km
① İsmetpaşa segment
Fault-parallal velocity (mm/yr)
Across-fault distance (km)
v0 = 29.8 mm/yr
D = 20.78 km
② Düzce segment
Elevation (m)
(b)
Residual velocities
5 mm/yr
Vs residuals (mm/yr)
Vn residuals (mm/yr)
Frequency percent
Systematic
Random
Systematic misfit index
(c)
Marmara
Izmit
Ismetpasa
Palu
Jordan Valley
Mean posterior creep rate
Prior creep rate
Mean posterior creep rate (mm/yr)
Longitude
45°N
40°N
35°N
20°E
25°E
30°E
35°E
40°E
45°E
50°E

**Figure 6.**

the North Anatolian Fault, as shown in Figure 6b and profile 1 in Figure 6a. However, surface creep rates along the Palu segment of the East Anatolian Fault and the offshore Marmara segment of the North Anatolian Fault are less well constrained due to limited near-fault GNSS data along these segments.

#### 4.3.2. India-Asia Collision Zone

The ongoing convergence of the Indian and Eurasian plates since the Eocene (~50 Ma) has driven the uplift, deformation, and lateral escape of the Tibetan Plateau (e.g., Clark & Royden, 2000; S. Liu et al., 2025; Molnar & Tapponnier, 1975; Searle et al., 2011; Wang & Shen, 2020; Yin & Harrison, 2000). This region has long been a focal point of research aimed at understanding the mechanisms governing present-day horizontal and vertical deformation, as well as its temporal evolution (Thatcher, 2009). Debate over these processes has centered around two end-member models: (a) deformation localized along discrete faults (e.g., Avouac & Tapponnier, 1993; Y. Li et al., 2025; Meade, 2007; Peltzer & Tapponnier, 1988; Replumaz & Tapponnier, 2003; Shen et al., 2005; Tapponnier et al., 1982, 2001; Thatcher, 2007), and (b) deformation occurring as a broadly distributed continuum (e.g., Clark & Royden, 2000; England & Molnar, 2005; Flesch et al., 2001; Holt et al., 2000; Houseman & England, 1993; Vilotte et al., 1986). The first model suggests that most surface deformation is accommodated along a finite number of faults bounding rigid tectonic blocks, whereas the second model posits that strain is diffusely distributed over large regions. An intermediate hypothesis reconciles these two perspectives, proposing that deformation is partitioned between localized faulting and distributed strain within tectonic blocks (e.g., Chen et al., 2004; Loveless & Meade, 2011; Fang et al., 2024).

The first-order characteristics of the GNSS velocity field relative to Eurasia, shown as blue vectors in Figure 7a, include: (a) a pronounced clockwise rotation of the southeastern borderlands of the Tibetan Plateau around the eastern Himalayan syntaxis, (b) a marked decrease in GNSS velocities across the Himalayas, the Longmen Shan in eastern Tibet, and the Qaidam block in northern Tibet, (c) eastward and westward motion of the Tibetan Plateau's eastern and western flanks, respectively; and (d) a general southeastward motion of lithospheric blocks in eastern Asia relative to the Eurasian Plate, including the South China Block, North China Block, Amurian Plate, and Ordos Block. To assess the quality of our strain rate inversion, we compared observed GNSS velocities with the mean posterior velocities predicted by our model (shown as red vectors in Figure 7a). The close agreement between the two indicates minimal systematic residuals at regional scales, with roughly 85% of GNSS velocity residuals falling within ±1 mm/yr, as illustrated in Figure 7b. Additionally, a velocity profile across the Xiaojiang Fault compares observed fault-parallel GNSS velocities, model-predicted (mean posterior) velocities from our strain rate inversion, and fault-parallel rates from an antiplane screw dislocation model (e.g., Savage & Burford, 1973; Weertman & Weertman, 1964), with the posterior distribution shown in Figure S18 of Supporting Information S1. The excellent agreement between model predictions and fault-parallel velocities further reinforces the robustness of our strain rate inversion, accurately capturing velocity gradients across faults (Figure 7a, panel 1).

While most previous studies interpret GNSS velocities in a Eurasia-fixed reference frame, we find that expressing them in a central Tibet-fixed reference frame (Figures S5c and S6d in Supporting Information S1) more effectively highlights internal deformation within Tibet and the relative motion of adjacent blocks. This approach, first advocated by Gan et al. (2007), has been largely overlooked in subsequent studies. In this reference frame, the dominant E-W extension across the plateau becomes more apparent. Additionally, it highlights that surface motions around the eastern Himalayan syntaxis cannot be explained by simple rigid block rotation alone. Instead, some internal deformation occurs in the regions bounded by the Jiali and Xianshuihe-Xiaojiang faults, where systematic stretching is clearly evident in the dilatation rate map (Figure 7c), consistent with previous strain rate studies (e.g., Allmendinger et al., 2007; Kreemer et al., 2014; Wang & Shen, 2020). This deformation pattern was recognized by geologists even before geodetic data became available for crustal deformation studies (e.g., Figure 1 in Tapponnier et al., 1982) and was attributed to extrusion-related extension. A more detailed analysis of this



**Figure 6.** (a) Comparison of observed velocities (blue vectors) and mean posterior velocities (red vectors). Profiles 1 and 2 show observed, mean posterior, and screw-dislocation model-predicted velocities (Savage & Burford, 1973; Weertman & Weertman, 1964) across the İsmetpaşa and Düzce segments of the North Anatolian Fault. Profiles demonstrate accurate modeling of velocity gradients –even across creeping faults– when dense near-fault GNSS velocities are available. (b) Residual velocities (observed minus modeled) colored by their systematic misfit index (red: systematic, blue: random). Histograms show the distribution of east and north velocity residuals. (c) Mean posterior creep rates on select fault segments (red: right-lateral creep rates, blue: left-lateral creep rates), with a profile showing prior and mean posterior creep rate variability along select fault segments as a function of longitude.

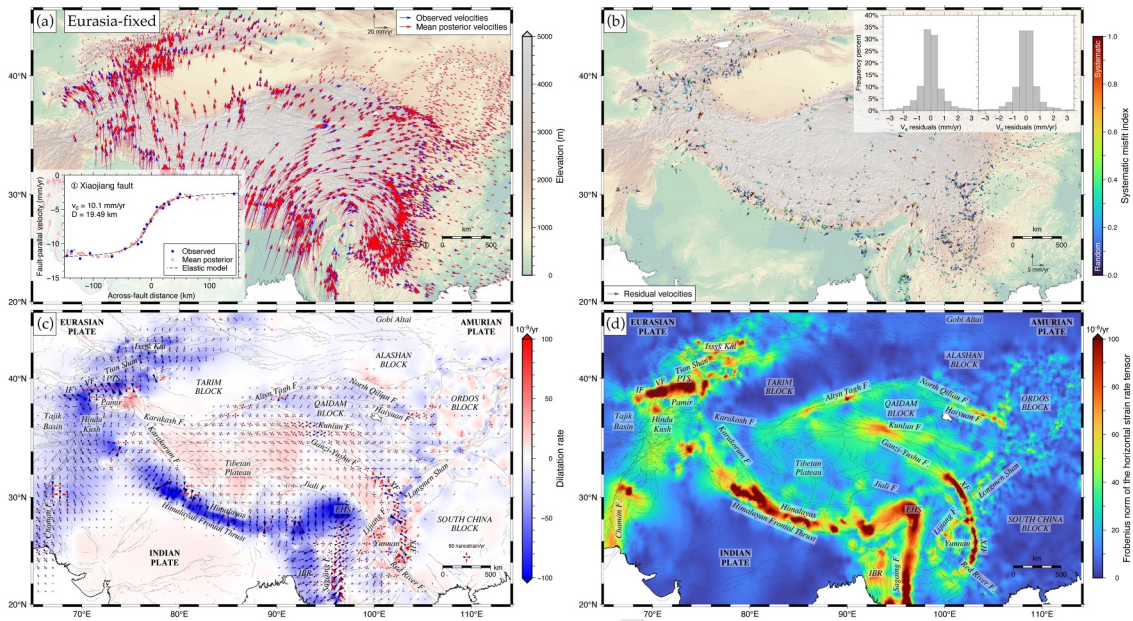


**Figure 7.** (a) Observed GNSS velocities (blue vectors) compared with mean posterior GNSS velocities (red vectors). Profile 1 illustrates observed, mean posterior, and screw dislocation model-predicted fault-parallel GNSS velocities across the Xiaojiang fault. (b) Residual GNSS velocities (observed−modeled) colored by their systematic misfit index (red: systematic, blue: random). Top-right histograms display the distribution of East and North GNSS velocity residuals. (c) Dilatation rate (first invariant) and principal strain rate directions (red: extension, blue: shortening). (d) Strain rate. PTS, Pamir Thrust System; VF, Vakhsh Fault; IF, Illiac Fault; XF, Xianshuihe Fault; XJF, Xiaojiang Fault; IBR, Indo-Burman Ranges.

clockwise rotation was conducted by Wang and Shen (2020), who attributed it to a combination of translation and rotation of small blocks within a larger rotating terrane confined between the Jiali and Xianshuihe-Xiaojiang faults. It is important to note, however, that GNSS velocities in this region may still contain postseismic signals from large earthquakes such as the 2001, $M_W$7.8 Kunlun and 2008, $M_W$8.0 Wenchuan earthquakes, as well as from several smaller earthquakes.

Figure 7c presents the dilatation rates and principal strain rate directions, highlighting key deformation patterns across the region. Significant N-S shortening is observed along the Himalayas, where dilatation rates typically range from −70 to −90 nanostrain/yr, with peaks exceeding −120 nanostrain/yr in the eastern Himalayan syntaxis, consistent with previous studies (e.g., Wang & Shen, 2020). Other regions of pronounced shortening include the Hindu Kush (−20 nanostrain/yr), where the maximum shortening direction trends NNE-SSW to NNW-SSE, western Pamir (−60 to −80 nanostrain/yr) and the Pamir Thrust System (−60 to −100 nanostrain/yr), both exhibiting NNW-SSE shortening, Central Tian Shan (−50 to −60 nanostrain/yr) undergoing N-S shortening, and the Qaidam Block in northeastern Tibet, where dilatation rates range from −10 to −20 nanostrain/yr, with principal strain rate directions showing NE-SW shortening. Additionally, NW-SE shortening is observed across the Longmen Shan in eastern Tibet, where typical dilatation rates range from −30 to −40 nanostrain/yr.

In contrast, extension is prominent in the northeastern Pamir, where E-W dilatation rates range from 10 to 40 nanostrain/yr, and across the Tibetan Plateau, where widespread E-W extension results in dilatation rates generally between 10 and 20 nanostrain/yr. The highest dilatation rates within the plateau, around 20 nanostrain/yr, are concentrated in its southern region, where seven N-S oriented rift zones have been documented (Armijo et al., 1986). However, a recent high-resolution strain rate map locally integrating InSAR and GNSS data revealed that dilatation rates exceed 50 nanostrain/yr along these rift zones (Chen et al., 2024), suggesting that strain rates may be higher than inferred from GNSS data alone. This underscores the importance of integrating GNSS and InSAR observations to refine strain rate estimates and improve the resolution of deformation patterns across this region in future studies. Additionally, a distinct belt of positive dilatation rates is observed between the Jiali and Xianshuihe faults in eastern Tibet, with values typically ranging from 10 to 20 nanostrain/yr, consistent with recent findings by Wang and Shen (2020). In this region, principal strain rate directions progressively rotate clockwise around the eastern Himalayan syntaxis.

Our refined strain rate estimates across the India-Asia collision zone and neighboring regions are shown in Figure 7d, highlighting distinct shear belts. In the westernmost part of our study area, the Chaman Fault exhibits strain rates of 50–60 nanostrain/yr, locally increasing to 70–90 nanostrain/yr in its better-instrumented northern segment. Further north, in the Hindu Kush, strain rates hover around 30 nanostrain/yr. Northward, the Pamir Thrust System shows strain rates between 100 and 150 nanostrain/yr, while the Vakhsh Fault, further west, reaches 130–170 nanostrain/yr. To the west, the Illiac Fault exhibits strain rates of 90–140 nanostrain/yr, decreasing systematically westward. In the Central Tian Shan, northeast of the Pamir Plateau, strain rates typically range from 50 to 60 nanostrain/yr, with local peaks around 100 nanostrain/yr near the Issyk Kul lake.

Moving eastward into the Tibetan Plateau, along the Altyn Tagh Fault, strain rates range from 40 to 60 nanostrain/yr, though GNSS station coverage is sparse. In the southeastern Tarim Basin, where instrumentation is denser, we observe a small cluster of high strain rates (80–150 nanostrain/yr) along the Altyn Tagh Fault. Further south, the Kunlun Fault exhibits typical strain rates of 40 nanostrain/yr (see profile D-D′, Figure 4), with localized peaks of 60–80 nanostrain/yr, likely influenced by postseismic deformation following the 2001 $M_s$8.1 Kunlun earthquake (see Figure 7d). The Karakorum Fault, in western Tibet, has systematically lower strain rates, around 30 nanostrain/yr. In northeastern Tibet, strain rates along the Haiyuan Fault hover around 60 nanostrain/yr, in agreement with recent results by D. L. Wu et al. (2024), peaking locally at 80 nanostrain/yr. However, our estimates are lower than the high-resolution InSAR-derived strain rates reported by Ou et al. (2022), which exceed 100 nanostrain/yr, with peaks surpassing 400 nanostrain/yr across a creeping section of the Haiyuan Fault that is not well resolved by our combined GNSS velocity field. Further south, the Ganzi-Yushu Fault displays strain rates of 40–50 nanostrain/yr, while across the Longmen Shan, on the eastern flank of the Tibetan Plateau, strain rates range from 30 to 50 nanostrain/yr.

Across the Himalayas, strain rates consistently exceed 60 nanostrain/yr, with typical values between 90 and 120 nanostrain/yr. The highest strain rates are observed in the eastern Himalayan syntaxis, with strain rates around 140 nanostrain/yr, peaking at 170 nanostrain/yr. Further east, distributed deformation accommodates relative motion between India, Burma, and South China along the southeastern borderlands of the Tibetan Plateau. Here, the Xianshuihe-Xiaojiang Fault System forms a semi-continuous high-strain belt exceeding 100 nanostrain/yr, with localized peaks reaching 180 nanostrain/yr at its northwestern termination, where surface creep has been documented by InSAR studies (e.g., Fang et al., 2024; X. Huang et al., 2023; Li, Nocquet, Shan, & Jian, 2021; Qiao & Zhou, 2021; Tong & Chen, 2024; J. Zhang et al., 2018).

However, unlike in the Mediterranean, where dense GNSS coverage enabled explicit modeling of along-strike variations in fault creep rates, the irregular and sparse distribution of near-fault GNSS stations along the creeping segments of the Xianshuihe Fault precluded a similar approach (see Figure S19 in Supporting Information S1). To the southwest, the Lijiang Fault, oriented NE-SW, forms a narrow shear belt with strain rates of 40–70 nanostrain/yr, peaking above 90 nanostrain/yr. Further south, the Sagaing Fault shows strain rates exceeding 100 nanostrain/yr, in agreement with previous estimates by Lindsey et al. (2023), though slightly lower rates (70–90 nanostrain/yr) are observed in its northern segment due to uneven GNSS station density. Strain rates along the Indo-Burman Ranges similarly range from 50 to 70 nanostrain/yr. Finally, higher posterior uncertainties are observed in regions experiencing greater deformation, particularly along major shear belts such as the Xianshuihe, Xiaojiang, Kunlun, Altyn Tagh, Haiyuan, and Sagaing faults, as well as the Pamir Thrust and Tian Shan, as illustrated in Figure S14 in Supporting Information S1.

## 5. Discussion

Building on the extensive GNSS-derived strain rate data set compiled in this study, we compare our results with other large-scale geophysical data sets indicative of lithospheric and mantle deformation, including stress indicators from the World Stress Map (WSM, Heidbach et al., 2025), seismic strain-rates inferred from the global Centroid Moment Tensor (gCMT) catalog (Dziewonski et al., 1981; Ekström et al., 2012, catalog up to 12/2024), and shear wave splitting (SKS) compilations (Becker et al., 2012, updated as of 02/2025). These comparisons seek to address two fundamental questions: How does the style of strain release from earthquakes compare to the strain accumulation captured by geodetic measurements along the Alpine-Himalayan belt? And to what extent do large-scale mantle deformation patterns, as inferred from seismic anisotropy, correlate with geodetically derived surface strain rates? To investigate these questions, we conduct three analyses: (a) a comparison between GNSS-derived strain rates and stress orientations from earthquake and borehole data, (b) an assessment of strain rate

styles and orientations between geodetic and seismic (Kostrov-summed) strain rate tensors, and (c) an evaluation of large-scale surface deformation patterns in relation to mantle dynamics inferred from seismic anisotropy.

### 5.1. Comparison of Strain Rate and Stress Orientations

Although several studies have used the maximum horizontal compressive stress ($S_{Hmax}$) as a proxy for the maximum shortening rate ($\dot{\varepsilon}_2$) direction (e.g., Bird, 2009; Flesch et al., 2005; Shen & Bird, 2022), it has been shown that the two do not always coincide and can exhibit systematic discrepancies in certain regions, such as central Japan, the San Andreas Fault, and the Cascadia subduction zone (e.g., Johnson, 2024; Schulte-Pelkum et al., 2021; Townend & Zoback, 2006).

To investigate this relationship across the Alpide belt, we follow methodologies implemented in previous studies (e.g., Johnson, 2024; Townend & Zoback, 2006; Yang & Hauksson, 2013). In our analysis, we use quality A, B, and C stress data from the World Stress Map (WSM, Heidbach et al., 2025), which are largely derived from earthquake focal mechanisms. As such, they are not entirely independent from strain rates derived from a Kostrov summation, and the relationship between stress and coseismic strain remains subject to ambiguity (e.g., McKenzie, 1969; Michael, 1987). We identify stress observations within a 50 km radius of each strain rate estimate exceeding 10 nanostrain/yr in the triangular mesh shown in Figure 3a. When at least two stress measurements are available, we compute the median stress azimuth and determine its angular difference relative to the maximum shortening direction from our strain rate inversion. Observations are excluded if they do not meet the strain rate threshold, lack sufficient nearby stress data, or if the stress measurements correspond to depths exceeding the local Moho depth from Reguzzoni and Sampietro (2015).

Our results, summarized in Figure 8, demonstrate a strong large-scale agreement between GNSS-derived maximum shortening rate directions (panel a) and maximum compressive stress orientations (panel b). The azimuthal differences between these parameters are shown in panel c, with the histogram in the bottom-left corner illustrating their distribution. The overall agreement is notable, with a median azimuthal difference of $-4.1 \pm 15.6$ degrees and a mode of $-5.0 \pm 15.6$ degrees across the entire Alpide belt, computed using 18 bins (every 10°). Warmer colors (positive values) indicate that the principal shortening rate direction is rotated clockwise relative to $S_{Hmax}$, while cooler colors (negative values) represent a counterclockwise offset. Additionally, a violin plot in Figure S20 of Supporting Information S1 illustrates the distribution of azimuthal differences ($\dot{\varepsilon}_2$ - $S_{Hmax}$) as a function of the strain rate, highlighting greater variance in lower strain rate regions.

Figure 8 also shows that $S_{Hmax}$ azimuths exhibit greater spatial variability than $\dot{\varepsilon}_2$ directions. This difference arises from the nature of the two data sets. The maximum shortening rate azimuths ($\dot{\varepsilon}_2$) emphasize broad, coherent deformation patterns, a consequence of the spatial regularization applied in the strain rate inversion. In contrast, the $S_{Hmax}$ estimates capture local stress conditions and record rotations associated with fault bends, segmentation, and depth variations. Moreover, seismogenic faults are not always optimally oriented relative to the regional stress field (e.g., Hardebeck & Michael, 2004; Townend & Zoback, 2004). Consequently, while the two data sets show strong regional agreement in their median statistics, the $S_{Hmax}$ azimuths display greater local variability.

### 5.2. Comparison Between Geodetic and Seismic Strain Rate Tensors

While comparing stress and principal strain rate directions provides valuable insights into their spatial relationships, a more comprehensive assessment requires analyzing the full strain rate tensor. Here, we evaluate whether strain accumulation and release styles are consistent across the Alpide belt by comparing strain rate styles from our GNSS-derived strain rate field with those inferred from Kostrov-summed earthquake moment tensors from the gCMT catalog (Dziewonski et al., 1981; Ekström et al., 2012). As noted, such Kostrov summations are not independent from the WSM stress constraints, the bulk of which are derived from focal mechanisms. However, they are independent from the GNSS-derived strain rates.

Following the formulation by Kostrov (1974), the average seismically released strain rate tensor $\dot{\varepsilon}_{ij}$ within a seismically strained crustal volume V containing N earthquakes with moment tensors $\mathcal{M}$ over a time period T, given a shear modulus $\mu$, is expressed as:

$$\dot{\varepsilon}_{ij} = \frac{1}{2\mu V T} \sum_{n=1}^{N} \mathcal{M}_{ij}^{(n)}. \quad (7)$$

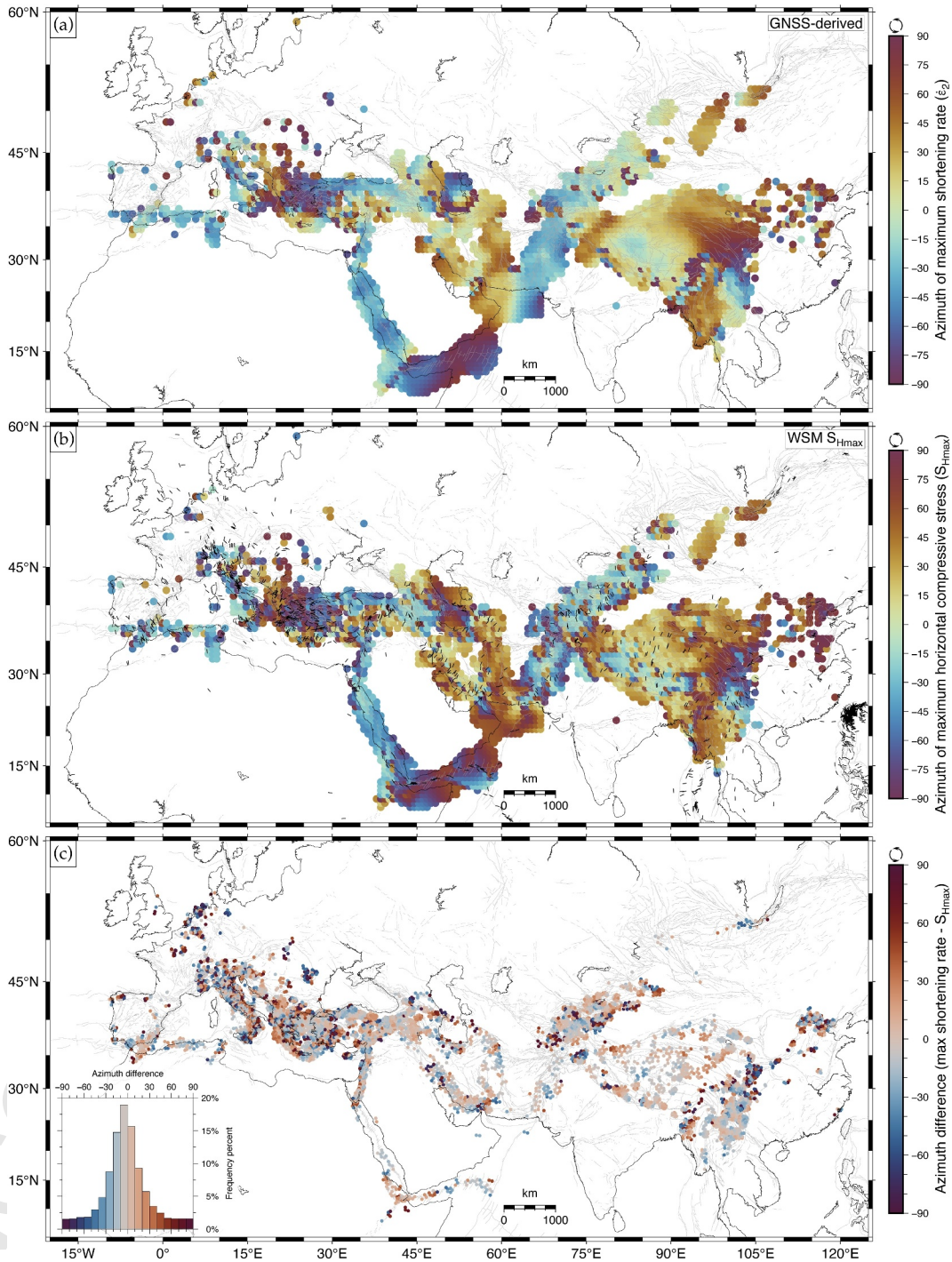


**Figure 8.** (a) GNSS-derived maximum horizontal shortening rate directions ($\dot{\varepsilon}_2$). (b) Maximum horizontal compressive stress ($S_{Hmax}$) azimuths from the World Stress Map (Heidbach et al., 2025), with black lines indicating their orientation. To reduce visual clutter, the WSM data set has been decimated for display purposes; however, all quality A, B, and C events were included in the analysis. (c) Azimuthal differences between the maximum shortening rate direction and the $S_{Hmax}$ azimuth ($\dot{\varepsilon}_2 - S_{Hmax}$). The histogram in the bottom-left corner shows the distribution of these azimuthal differences. Warmer colors indicate a clockwise offset of the principal shortening rate direction relative to $S_{Hmax}$, while cooler colors indicate an anti-clockwise offset. A mask was applied to show only regions where strain rates exceed 10 nanostrain/yr.

In our analysis, we estimated strain rate tensors by applying a normalized Kostrov summation of moment tensors from the gCMT catalog using an equidistant 0.5° × 0.5° grid, considering earthquakes with hypocentral depths shallower than 50 km and $M_W \geq 5$. We then computed the eigenvalues of both strain rate tensor data sets (Kostrov-summed and GNSS-derived) to obtain the principal strain rates (see details in Appendix A). To ensure spatial consistency, both data sets were linearly interpolated onto a common regular grid, retaining observations where strain rates exceed 10 nanostrain/yr, following the approach used in our previous analysis of stress and principal strain rate orientations.

The strain rate style was computed as a ratio of principal strain rates: $-\frac{\varepsilon_1+\varepsilon_2}{|\varepsilon_1|+|\varepsilon_2|}$. This ratio ranges from −1 (indicating a normal faulting style) to +1 (indicating a reverse faulting style), with strike-slip faulting corresponding to values near zero (Johnson, 2024). Figures 9a and 9b illustrate the strain rate styles derived from GNSS velocities and Kostrov-summed moment tensors, respectively, while Figure S21 in Supporting Information S1 presents a map of their signed angular differences (GNSS−Kostrov). Strain rate styles derived from Kostrov-summed moment tensors depend on the lower magnitude threshold applied. Due to the Gutenberg-Richter distribution, small earthquakes are more abundant and improve spatial resolution, but their moment tensors are generally less reliable. We tested thresholds ranging from 3.5 (i.e., all events, lowest actual $M_W$ in the catalog is 4.3) to 6.5 and found that a moment magnitude cutoff of 5 provides a good balance—ensuring sufficient resolution while mitigating the uncertainties associated with smaller earthquake moment tensors. To illustrate this sensitivity, we include strain rate style maps using lower magnitude thresholds of 3.5, 5.5, and 6.5 in the (Figure S22 in Supporting Information S1).

Consistent with earlier, more geographically limited comparisons (e.g., Faccenna, Becker, Auer, et al., 2014; Holt et al., 2000; Jenny et al., 2004; Kahle et al., 1998), our results reveal a strong large-scale agreement between strain accumulation and coseismic release styles across the Alpide belt, with a median strain rate style difference of 0.1 ± 0.3 (Figure S21 in Supporting Information S1). The mode ± mean absolute deviation (MAD), computed using 18 bins, matches the median ± MAD, reflecting the symmetric distribution of signed strain rate style differences. Small-scale discrepancies primarily arise from the low frequency of instrumental earthquakes along some plate boundaries (e.g., the Himalayas), which biases strain rate styles inferred from Kostrov-summed moment tensors. Additional mismatches occur in subduction settings where intermediate-depth slab earthquakes, such as normal-faulting events in the Caspian Sea linked to slab tearing (e.g., Mumladze et al., 2015) and those within the descending slab of the Makran subduction zone (e.g., Barnhart et al., 2014), influence the inferred strain rate style.

To complement our results, we computed the misfit between geodetic and seismic (Kostrov-summed) strain rate tensors, following a tensor inner product approach used by Frohlich and Davis (1999) and Flesch et al. (2007; Eq. 22). To quantify the misfit, we calculated the normalized inner product between the geodetic and seismic strain rate tensors, $\frac{\dot{\varepsilon}_{geo} : \dot{\varepsilon}_{seis}}{||\dot{\varepsilon}_{geo}||||\dot{\varepsilon}_{seis}||}$, which ranges from +1 (perfect match) through 0 (orthogonal) to −1 (opposite orientations). Our results demonstrate large-scale agreement between the orientations of the 2D geodetic and seismic strain rate tensors across the Alpine–Himalayan Belt (Figure 9c). As noted earlier, opposite geodetic and seismic strain rate orientations occur in the Caspian Sea and inland Makran, where slab-related normal events dominate. Offshore Makran also shows poor agreement, with misfit values close to −1, reflecting both bleeding of our modeled strain rates into unconstrained offshore regions and the influence of normal-faulting earthquakes along the Murray Ridge between the Owen Fracture Zone and the Makran subduction zone. Another area of disagreement lies in the northwestern corner of the North China Block, where geodetic strain rate tensors indicate broadly E-W extension, but most instrumental earthquakes display right-lateral strike-slip motion on NNE-trending faults (Y. G. Zhang et al., 2018).

### 5.3. Large-Scale Patterns of GNSS-Derived Surface Strain Rates and Mantle Dynamics Inferred From Seismic Anisotropy Compilations

While strain in the crust can be measured directly via geodetic or geological observations, mantle strain must be inferred indirectly from seismic data, either from the earthquake source via moment release or from seismic anisotropy (e.g., Holt, 1995; Holt, 2000; Silver, 1996; Silver & Holt, 2002). One of the most widely used methods for inferring mantle strain is through azimuthal seismic anisotropy inferred from shear wave splitting

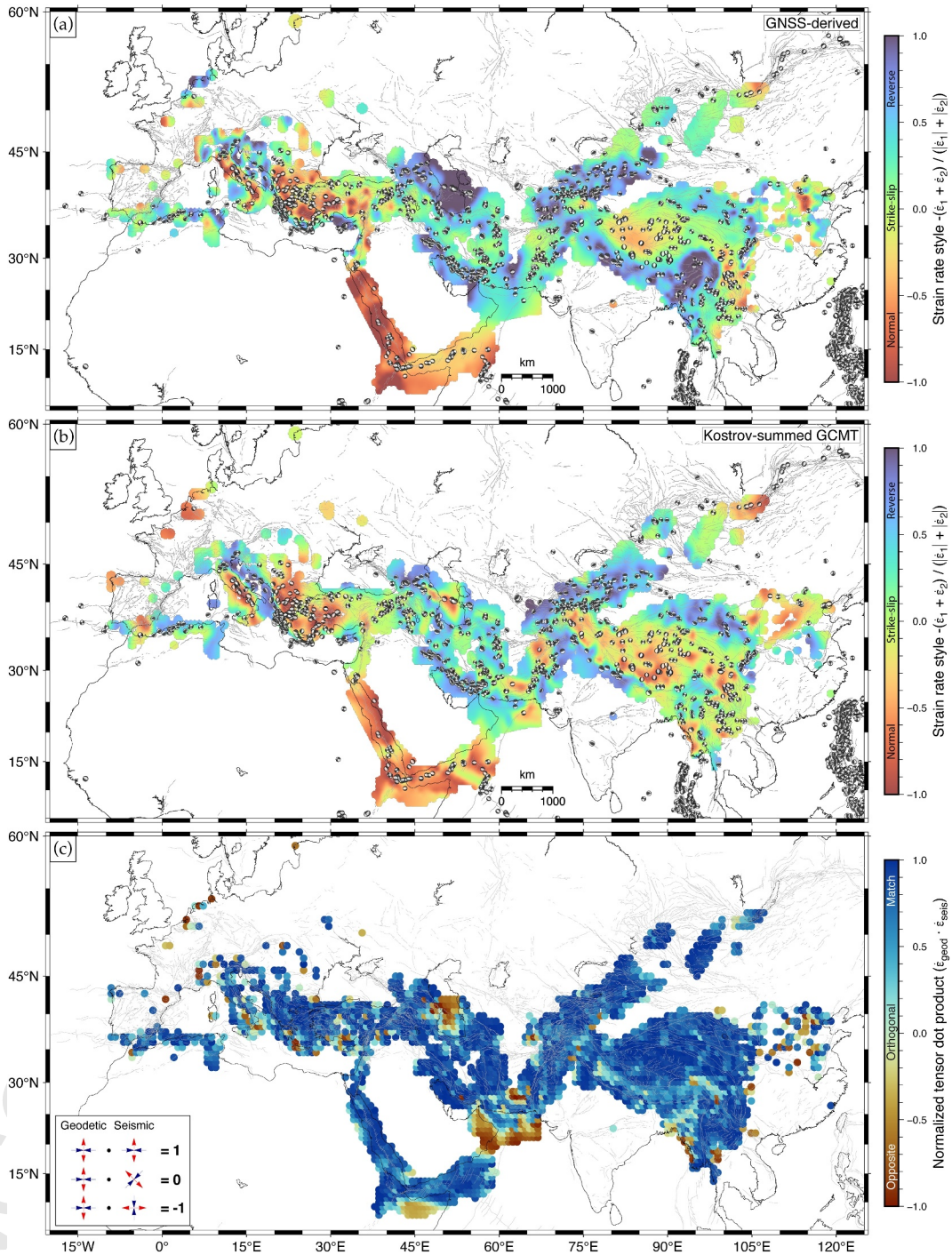


**Figure 9.** (a) Geodetic strain rate style (red: normal, green: strike-slip, blue: reverse). Moment tensors ($M_W \geq 5$, depth <50 km) are from the gCMT catalog (Dziewonski et al., 1981; Ekström et al., 2012). (b) Seismic strain rate style from Kostrov-summed gCMT tensors with the same criteria. (c) Misfit between geodetic and seismic strain rate tensor orientations, expressed as the dot product of normalized tensors (blue: perfect agreement, green: orthogonal, red: opposite). Results are masked where the strain rate is <10 nanostrain/yr.

measurements (e.g., Silver & Chan, 1991; Vinnik et al., 1992), as upper mantle anisotropy is largely attributed to crystallographic preferred orientation (CPO) of intrinsically anisotropic olivine crystals (e.g., Christensen & Crosson, 1968; Nicolas & Christensen, 1987; Silver, 1996).

When shear waves pass through an anisotropic medium, they can be split into two orthogonally polarized wave trains that propagate at different speeds. This splitting is quantified by two parameters: the azimuth of the fast-polarized wave ($\phi$, "fast axis") and the time delay ($\delta t$) between the fast and slow shear wave components (e.g., Silver, 1996; Savage, 1999). Core refracted phases such as SK(K)S are often used since this rules out source side anisotropy; while anisotropy may accumulate anywhere along the path, much of the signal is attributed to the uppermost mantle where dislocation creep can form CPOs (e.g., Becker et al., 2008; Fischer & Wiens, 1996; Podolefsky et al., 2004). While the formation and reworking of CPOs is complex, we expect that "A type" fabrics are predominant in the upper mantle, in which case the fast axes should rotate from the maximum extension to the shear orientation for large strains (e.g., Becker et al., 2008, 2014; Bernard et al., 2019; Zhang & Karato, 1995). Consequently, SKS fast orientations from seismic anisotropy studies provide valuable insights into lithospheric mantle flow and finite strain (e.g., Silver, 1996; Zhang & Karato, 1995).

Early studies comparing SKS fast orientations with surface tectonic features revealed spatial correlations in certain regions. For example, Vinnik et al. (1992) observed that in areas of active plate convergence, SKS fast polarization orientations tend to align with plate boundaries and follow the orientation of associated mountain ranges. Subsequent studies corroborated these findings using strain estimates derived from active faulting and plate-motion models, identifying a general consistency between SKS fast orientations and the directions of maximum crustal horizontal extension in the Tian Shan, Altai, Sayan, and Baikal regions (e.g., Davis et al., 1997). These results suggested coherent mantle and lithospheric deformation and highlighted the potential role of mantle flow in orogenesis (Silver, 1996). In Tibet, McNamara et al. (1994) observed that SKS fast orientations align with fault traces rather than the maximum horizontal elongation directions. Later, with advancements in GNSS instrumentation, Holt (2000) further demonstrated that SKS fast orientations in Tibet systematically align with left-lateral crustal shear planes, supporting the findings of McNamara et al. (1994).

Additionally, several studies identified consistent patterns in rift settings, where SKS fast axes generally parallel the extensional direction, as observed in the Baikal and East African Rift (e.g., Gao et al., 1994; Kendall et al., 2006; Vinnik et al., 1992). Furthermore, SKS fast orientations have been observed to align with the azimuths of major strike-slip faults, such as the Alpine Fault in New Zealand (Savage et al., 2004) and the strike-slip fault systems of Tibet (e.g., Holt, 2000; McNamara et al., 1994). A similar alignment has also been noted in the upper anisotropic layer required to fit SKS observations along the San Andreas Fault (e.g., Hartog & Schwartz, 2001; Özalaybey & Savage, 1995; Savage et al., 2004).

However, interpreting shear wave splitting observations remains challenging, particularly in continental regions where complex tectonic histories can lead to significant heterogeneities within the crust and lithosphere. Such heterogeneities can influence both shallow, frozen-in anisotropy and deeper mantle flow (e.g., Fouch & Rondenay, 2006; Schulte-Pelkum et al., 2021; Silver, 1996). Aside from uncertainties surrounding CPO formation, many tectonic scenarios are compatible with multiple interpretations. For instance, observed rift-aligned fast axes may reflect contributions from partial melting, mantle flow, or a combination of both (e.g., Faccenna et al., 2013; Kendall et al., 2006). Moreover, the influence of plate boundaries on rotating fast axes from background trends is not uniform (e.g., Becker et al., 2006; Biryol et al., 2010; Faccenna, Becker, Auer, et al., 2014; Silver & Holt, 2002), with pronounced rotations observed only across faults in few regions. One key issue is that the alignment with crustal features may be indicative of causation, such as a lithospheric origin of anisotropy, or only apparent, such as when the shear in the mantle is coherent with what is observed in the crust (e.g., Silver, 1996; Savage, 1999).

Our analysis here focuses on documenting the angular relationships between SKS fast orientations ($\phi$) and the maximum stretching rate ($\dot{\varepsilon}_1$) direction across different sections of the Alpine-Himalayan belt, without attempting to necessarily infer causality or propose specific physical mechanisms behind these correlations. This is achieved with an unprecedented resolution, made possible by our large-scale strain rate estimates, complemented with an up-to-date station-averaged SKS splitting compilation by Becker et al. (2012, updated 02/2025). Figure 10a provides a large-scale comparison of SKS fast orientations (orange lines) and maximum stretching rate directions (blue lines) across the Alpine-Himalayan belt, with azimuthal difference statistics summarized in Table 3. We report both the median and mode, along with their MAD, to characterize azimuthal differences. However, because the mode more effectively captures dominant azimuthal correlations—particularly in skewed distributions—we adopt the mode ± MAD as our primary measure, providing a geophysically meaningful and statistically robust

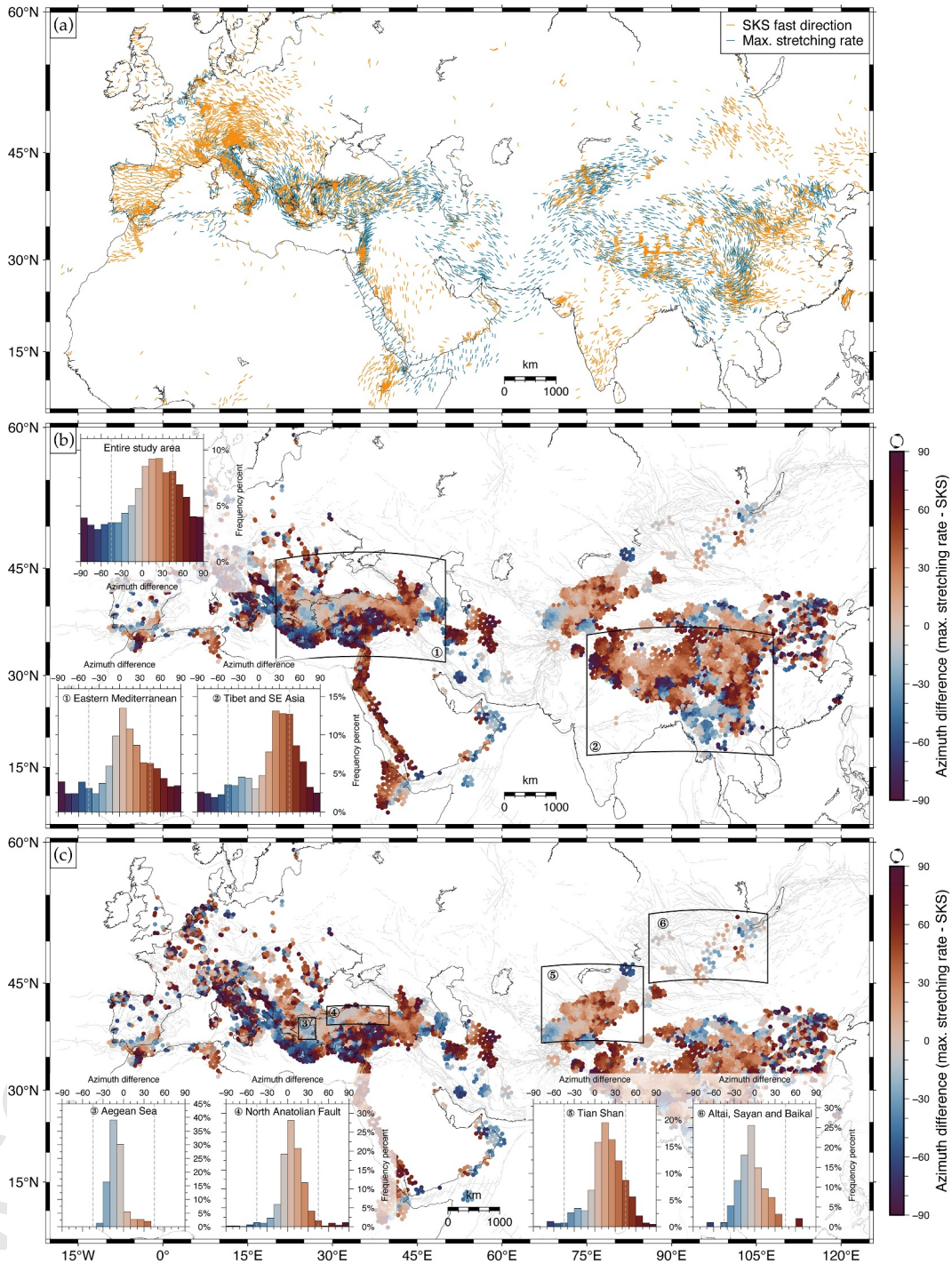


**Figure 10.** (a) GNSS-derived maximum stretching rate azimuths $\dot{\varepsilon}_1$ (blue) and SKS fast orientations (orange), compiled by Becker et al. (2012, updated 02/2025). (b, c) Signed azimuthal differences between $\dot{\varepsilon}_1$ and SKS fast orientations, with histograms showing distributions across the Alpide Belt (top-left) and in selected regions: (1) eastern Mediterranean, (2) Tibet and SE Asia, (3) Aegean Sea, (4) North Anatolian fault, (5) Tian Shan, and (6) Altai-Sayan-Baikal regions. Dashed vertical gray lines mark maximum shear strain rate directions ($\pm 45°$ from $\dot{\varepsilon}_1, \dot{\varepsilon}_2$). Warm colors indicate clockwise offsets of $\dot{\varepsilon}_1$ relative to fast SKS directions, cool colors counter-clockwise, and dark purple near-perpendicular orientations. A mask was applied to show only regions where strain rates exceed 10 nanostrain/yr.

**Table 3**
*Statistical Summary of Azimuth Differences Between SKS Fast Orientations ($\phi$) and Maximum Principal Strain Rate ($\dot{\varepsilon}_1$) Directions in Different Regions of the Alpine-Himalayan Belt*

| Region | Data points | Median ± MAD (°) | Mode ± MAD (°) | Map |
|---|---|---|---|---|
| Eastern Mediterranean | 3,919 | 9.1 ± 25.5 | 5.0 ± 26.1 | Figure 10b |
| Tibet and Southeast Asia | 3,171 | 27.7 ± 22.9 | 25.0 ± 24.2 | Figure 10b |
| Aegean Sea | 146 | −11.5 ± 6.9 | −15.0 ± 6.8 | Figure 10c |
| North Anatolian Fault | 694 | 6.6 ± 10.0 | 5.0 ± 10.1 | Figure 10c |
| Tian Shan | 1,068 | 17.9 ± 14.4 | 15.0 ± 14.2 | Figure 10c |
| Altai, Sayan, and Baikal | 94 | −5.8 ± 12.5 | −5.0 ± 12.1 | Figure 10c |

*Note*. MAD is the median absolute deviation, computed as median ($|X_i - C(X)|$), where $C(X)$ represents either the *median* or *mode* of $X$, depending on which statistics is being presented. The mode was computed using 18 bins (every 10°).

representation of the most frequent azimuthal difference between SKS fast orientations and principal strain rate directions.

#### 5.3.1. Eastern Mediterranean

In the eastern Mediterranean, SKS fast orientations broadly align with GNSS-derived maximum stretching rate directions in the crust ($\dot{\varepsilon}_1$), consistent with previous findings (e.g., Endrun et al., 2011; Kreemer et al., 2004; Merry et al., 2021). Across the region spanning from the Aegean to the Caspian Sea, $\dot{\varepsilon}_1$ is rotated clockwise relative to SKS, with a mode azimuthal difference is 5.0° ± 26.1° (see histogram 1 in Figure 10b). In the Aegean, where SKS fast orientations are broadly NE-SW (Hatzfeld et al., 2001; Kreemer et al., 2004; Paul et al., 2014), $\dot{\varepsilon}_1$ is rotated counterclockwise relative to SKS, with a mode azimuthal difference of −15.0° ± 6.8°, as illustrated in histogram 3, Figure 10c.

Along the North Anatolian Fault (NAF), alignment is particularly strong, with a mode azimuthal difference of 5.0° ± 10.1°, as shown in histogram 4, Figure 10c. A systematic along-strike variation is evident: in the eastern NAF, $\dot{\varepsilon}_1$ is slightly rotated clockwise relative to SKS, transitioning westward to a slight counterclockwise rotation, ultimately matching the pattern in the Aegean. In contrast, no clear correlation is detected in central Anatolia; a potential change in alignment of fault proximal azimuthal anisotropy from extensional to maximum shear strain might be expected from fault maturity controlled fabrics (e.g., Biryol et al., 2010; Bonnin et al., 2012; Vauchez et al., 2012) but remains to be further explored. Further south, in the Hellenic and Cyprus back-arc regions, SKS fast orientations and $\dot{\varepsilon}_1$ are nearly perpendicular, consistent with previous studies (e.g., L. Jolivet et al., 2009; L. Jolivet et al., 2013).

#### 5.3.2. Central Asia

In the Tian Shan region, SKS fast orientations generally run subparallel to the mountain range, particularly in the western section of the range, with a mode azimuthal difference of 15.0° ± 14.2°, in agreement with earlier studies (e.g., Davis et al., 1997; Makeyeva et al., 1992; Vinnik et al., 1992). However, two small clusters of anomalous NNE-SSW SKS fast orientations appear around Issyk Kul and along the Tian Shan–Tarim boundary, resulting in localized azimuthal differences between 50° and 90° between SKS orientations and $\dot{\varepsilon}_1$, as shown in Figure 10c. These deviations have been attributed to various mechanisms, including small-scale mantle convection (Wolfe & Solomon, 1998), an upper mantle plume (Makeyeva et al., 1992), or shear between the northward-moving lithosphere and the underlying asthenosphere (A. Li & Chen, 2006).

#### 5.3.3. Tibet and Southeast Asia

In Tibet and Southeast Asia, SKS fast orientations and $\dot{\varepsilon}_1$ exhibit a systematic offset of 25.0° ± 24.2°, with $\dot{\varepsilon}_1$ consistently rotated clockwise relative to SKS fast orientations across the Tibetan Plateau, as depicted in histogram 2, Figure 10b. This result aligns with previous studies (e.g., Holt, 2000; McNamara et al., 1994), which report that SKS fast orientations align with left-lateral crustal shear planes, and are generally subparallel to major strike-slip faults in the region. Additionally, our findings agree with Savage (1999), who first documented a

systematic misalignment of 10°–30° between SKS fast orientations and maximum elongation orientations from plate motion models, with the latter exhibiting a consistent clockwise rotation relative to the SKS fast orientations.

A notable regional variation occurs in Yunnan and Indochina, where SKS fast orientations transition from N-S to E-W. This sharp change has been used to assess the extent of inferred viscous crustal channel flow, suggesting crustal and mantle deformation may be coupled in Southeast Tibet but decoupled farther south in Yunnan and Indochina (e.g., Clark & Royden, 2000; Flesch et al., 2005; Kong et al., 2018; Lev et al., 2006; Lin & Zhao, 2024; Royden et al., 1997). Additionally, this shift has been linked to a possible change in upper mantle deformation style, transitioning from simple shear in Southeast Tibet to pure shear in Yunnan (e.g., Wang et al., 2008).

#### 5.3.4. Altai, Sayan and Baikal Regions

Despite limited observations, we find a general alignment between SKS fast polarization and $\dot{\varepsilon}_1$ in the Altai, Sayan, and Baikal regions, with a mode azimuthal difference of $-5.0° \pm 12.1°$, as shown in histogram 6 of Figure 10c, consistent with earlier findings (e.g., Davis et al., 1997; Gao et al., 1994; Vinnik et al., 1992). Our results thus reinforce and further substantiate previous studies documenting systematic regional-scale correlations between principal strain rate orientations and SKS fast orientations from seismic anisotropy across the Alpide belt. How much of this alignment arises due to lithospheric and how much due to mantle contributions needs to be further explored by tectonic and mantle flow modeling.

## 6. Conclusion

We estimate strain rates along the Alpine-Himalayan belt using a unified, comprehensive, and up-to-date GNSS velocity field constructed with `FICORO_GNSS`, a Python toolbox developed for filtering and combining GNSS velocities. Our results show a remarkable agreement between both the styles and orientations of geodetic and seismic (Kostrov-summed) strain rate tensors. Similarly, we observe a strong correspondence between strain rate and stress orientations in the crust. These results suggest overall consistency between the styles of strain accumulation and release across the Alpide belt.

Additionally, we find that mismodeled strain rates due to surface fault creep can be substantial in some regions—for example, exceeding 300 nanostrain/yr along the İsmetpaşa segment of the North Anatolian Fault. To avoid misattributing these localized velocity discontinuities to strain rates from elastic coupling on faults, we explicitly incorporate surface creep rates into our inversion where dense near-fault geodetic data are available. Distinguishing between strain rates associated with elastic coupling on faults and those arising from surface fault creep is essential for seismic hazard assessment, as only the former contributes to the elastic energy buildup to be released in future earthquakes.

Our analyses substantiate previous findings of regional-scale relationships between surface deformation and SKS fast orientations from seismic anisotropy compilations, which are thought to be associated with different mantle deformation regimes. While these correlations do not necessarily imply causation and remain poorly understood, we hypothesize that the observed systematic angular relationships between SKS and principal strain rate directions in regions such as the Aegean, North Anatolia, Tibet, Tian Shan, Altai, Sayan, and Baikal, may reflect deep-seated mantle dynamics, as has been previously suggested. Nevertheless, this hypothesis warrants further investigation, particularly regarding the effects of depth-dependent anisotropy in the lithosphere and its relationship with surface deformation.

## Appendix A: The 2D Strain Rate Tensor and Its Invariants

Given a set of geodetically derived horizontal surface velocities $v$, we can define the strain rate tensor as:

$$\dot{\varepsilon}_{i,j} = \frac{1}{2}\left(\frac{\partial v_i}{\partial x_j} + \frac{\partial v_j}{\partial x_i}\right) = \begin{pmatrix} \frac{\partial v_1}{\partial x_1} & \frac{1}{2}\left(\frac{\partial v_1}{\partial x_2} + \frac{\partial v_2}{\partial x_1}\right) \\ \frac{1}{2}\left(\frac{\partial v_2}{\partial x_1} + \frac{\partial v_1}{\partial x_2}\right) & \frac{\partial v_2}{\partial x_2} \end{pmatrix}, \tag{A1}$$

where $i$ and $j$ represent the components of coordinates $x$ and surface velocities $v$. Here, we consider surface horizontal strain rates, then $i,j = 1,2$, where the eigenvalues of the strain rate tensor represent the principal strain rates ($\dot{\varepsilon}_1$ and $\dot{\varepsilon}_2$):

$$\dot{\varepsilon}_1, \dot{\varepsilon}_2 = \frac{\dot{\varepsilon}_{11} + \dot{\varepsilon}_{22}}{2} \pm \sqrt{\left(\frac{\dot{\varepsilon}_{11} - \dot{\varepsilon}_{22}}{2}\right)^2 + \dot{\varepsilon}_{12}^2}, \tag{A2}$$

and their corresponding eigenvectors are the principal strain rate orientations. In continuum mechanics, we often use the tensor's coordinate system independent quantities (i.e., the invariants) for quantifying geodetically derived surface strain rates. These invariants appear as coefficients of the characteristic polynomial of the tensor, which for a 2D horizontal strain rate tensor is given by $\lambda^2 - I_1\left(\dot{\varepsilon}\right)\lambda + I_2\left(\dot{\varepsilon}\right) = 0$, where $I_1$ and $I_2$ are the first and second invariants, respectively.

The first invariant is the trace of the strain rate tensor, representing the areal strain rate (dilatation rate, $\dot{\Delta}$), which is equivalent to the divergence of the velocity field:

$$I_1^{2D}\left(\dot{\varepsilon}\right) = \dot{\Delta} = \nabla \cdot v = \mathrm{tr}\left(\dot{\varepsilon}\right) = \dot{\varepsilon}_{11} + \dot{\varepsilon}_{22} = \dot{\varepsilon}_1 + \dot{\varepsilon}_2. \tag{A3}$$

A related quantity is the mean (normal) horizontal strain rate ($\dot{\varepsilon}_m^{2D}$), defined as:

$$\dot{\varepsilon}_m^{2D} = \frac{1}{2} I_1^{2D} = \frac{1}{2}\left(\dot{\varepsilon}_1 + \dot{\varepsilon}_2\right) \tag{A4}$$

The second invariant can be expressed in several equivalent forms. The formal definition can be written as:

$$I_2\left(\dot{\varepsilon}\right) = \frac{1}{2}\left[\mathrm{tr}\left(\dot{\varepsilon}\right)^2 - \mathrm{tr}\left(\dot{\varepsilon}^2\right)\right]. \tag{A5}$$

In the special case of a 2D tensor, this reduces directly to the determinant:

$$I_2^{2D}\left(\dot{\varepsilon}\right) = \det\left(\dot{\varepsilon}\right) = \dot{\varepsilon}_{11}\dot{\varepsilon}_{22} - \dot{\varepsilon}_{12}^2. \tag{A6}$$

Equivalently, because the determinant of a tensor equals the product of its eigenvalues, the second invariant of the 2D strain rate tensor is also:

$$I_2^{2D}\left(\dot{\varepsilon}\right) = \dot{\varepsilon}_1\, \dot{\varepsilon}_2. \tag{A7}$$

The definition of the second invariant of the 2D horizontal strain rate tensor has been applied inconsistently in the literature. A commonly used expression is:

$$\|\dot{\varepsilon}\|_F^{2D} = \sqrt{\dot{\varepsilon}_{11}^2 + \dot{\varepsilon}_{22}^2 + 2\dot{\varepsilon}_{12}^2}, \tag{A8}$$

$$\|\dot{\varepsilon}\|_F^{2D} = \sqrt{\dot{\varepsilon}_1^2 + \dot{\varepsilon}_2^2},$$

which corresponds to the Frobenius (Euclidean) norm of the 2D horizontal strain rate tensor rather than its formal second invariant ($I_2$, Equation A5). The Frobenius norm is often preferred because it is always non-negative, whereas the formal second invariant ($I_2$) can be negative if $\dot{\varepsilon}_{11}\dot{\varepsilon}_{22} - \dot{\varepsilon}_{12}^2 < 0$. To facilitate direct comparison with previous studies, we adopted the Frobenius norm in this work.

Another common measure is the maximum shear strain rate ($\dot{\gamma}_{max}$), which relates to the second invariant of the deviatoric strain rate tensor ($J_2$), and in 2D is given by:

$$|\dot{\gamma}^{2D}_{max}| = \sqrt{J_2},$$
$$\dot{\gamma}^{2D}_{max} = \frac{1}{2}\sqrt{\left(\dot{\varepsilon}_{11} - \dot{\varepsilon}_{22}\right)^2 + 4\dot{\varepsilon}_{12}} = \frac{1}{2}\left(\dot{\varepsilon}_1 - \dot{\varepsilon}_2\right). \tag{A9}$$

Combining Equations A2 and A9, we find that the principal extension and shortening rates $\dot{\varepsilon_1}$,$\dot{\varepsilon_2}$ can be rewritten in terms of $\dot{\Delta}$ and $\dot{\gamma}_{max}$

$$\dot{\varepsilon_1} = \frac{\dot{\Delta} + \dot{\gamma}_{max}}{2},$$
$$\dot{\varepsilon_2} = \frac{\dot{\Delta} - \dot{\gamma}_{max}}{2}.$$

A relationship exists between $J_2$, $I_1 = \mathrm{tr}\left(\dot{\varepsilon}\right)$, and $\|\dot{\varepsilon}\|^{2D}_F$, which can be written as:

$$\|\dot{\varepsilon}\|^{2D}_F = \sqrt{2J_2 + \frac{1}{2}(I_1)^2}. \tag{A10}$$

From Equation A10, it is clear that for a 2D deviatoric strain rate tensor $\dot{\varepsilon}'$, the Frobenius norm is just a scaled form of the deviatoric second invariant, or equivalently, a scaled form of the maximum shear strain rate:

$$\|\dot{\varepsilon}'\|^{2D}_F = \sqrt{2J_2} = \sqrt{2} \cdot \dot{\gamma}^{2D}_{max}. \tag{A11}$$

The azimuth of the maximum principal strain rate ($\dot{\varepsilon}_{max}$) can be estimated as follows:

$$Az_{\dot{\varepsilon}_{max}} = 90° - \frac{\arctan\left(\frac{\dot{\varepsilon}_{12}}{\frac{\dot{\varepsilon}_{11} - \dot{\varepsilon}_{22}}{2}}\right)}{2}. \tag{A12}$$

We can further estimate the azimuth of the maximum shortening rate ($\dot{\varepsilon}_2$) by evaluating the sign of the maximum principal strain rate ($\dot{\varepsilon}_{max}$). If $\dot{\varepsilon}_{max} > 0$ (extension), the maximum shortening rate occurs 90° away from the azimuth of $\dot{\varepsilon}_{max}$. On the other hand, if $\dot{\varepsilon}_{max} < 0$ (compression), the azimuth of $\dot{\varepsilon}_{max}$ directly represents the maximum shortening direction.

## Conflict of Interest

The authors declare no conflicts of interest relevant to this study.

## Data Availability Statement

All results and figures presented in this study are fully reproducible using the Jupyter notebook and supporting files archived in an open-access repository (Castro-Perdomo, 2025). The Python toolkit `FICORO_GNSS` Version 1.3.0, developed for filtering and combining GNSS velocity fields, is distributed under the MIT License and permanently archived in a public repository (Castro-Perdomo, 2024). The MATLAB code `BForStrain` Version 1.1.0 was used to invert GNSS velocities for strain rates and is publicly available in an open-access repository (Johnson, 2023). Comparisons between GNSS-derived strain rates and $S_{Hmax}$ orientations were conducted using the World Stress Map (WSM 2025) data set, available through the GFZ Data Services Portal (Heidbach et al., 2025). Maps were generated using the Generic Mapping Tools (`GMT`) Version 6.5.0 (Wessel et al., 2019), `PyGMT` Version 0.12.0 (Tian et al., 2024), and the scientific color maps of Crameri (2023).

**Acknowledgments**
We thank Romain Jolivet and Jorge Jara for providing GNSS velocities for the İsmetpaşa segment of the North Anatolian Fault, and Seda Özarpacı for contributing GNSS velocities across the Izmit segment. We are also grateful to Jeff Freymueller and an anonymous reviewer for their constructive comments, which helped improve the manuscript, and to Michael Hamburger for his thoughtful in-house reviews. This research was supported by the National Science Foundation (NSF) under award EAR-2045292, and in part by King Abdullah University of Science and Technology (KAUST) under award OSR-CRG2020-4335.

## References

Abdrakhmatov, K., Arrowsmith, R., Elliott, J., Grutzner, C., Mukambayev, A., Rizza, M., et al. (2024). Urgent need for greater earthquake resilience in continental Asia. *Nature Geoscience*, *17*(9), 818–819. https://doi.org/10.1038/s41561-024-01531-0

Alchalbi, A., Daoud, M., Gomez, F., McClusky, S., Reilinger, R., Romeyeh, M. A., et al. (2010). Crustal deformation in northwestern Arabia from GPS measurements in Syria: Slow slip rate along the northern Dead Sea Fault. *Geophysical Journal International*, *180*(1), 125–135. https://doi.org/10.1111/j.1365-246X.2009.04431.x

Allmendinger, R. W., Reilinger, R., & Loveless, J. (2007). Strain and rotation rate from GPS in Tibet, Anatolia, and the Altiplano. *Tectonics*, *26*(3). https://doi.org/10.1029/2006TC002030

Altamimi, Z., Métivier, L., Rebischung, P., Rouby, H., & Collilieux, X. (2017). ITRF2014 plate motion model. *Geophysical Journal International*, *209*(3), 1906–1912. https://doi.org/10.1093/gji/ggx136

Altamimi, Z., Sillard, P., & Boucher, C. (2002). ITRF2000: A new release of the International Terrestrial Reference Frame for earth science applications. *Journal of Geophysical Research*, *107*(B10), ETG2-1–19. https://doi.org/10.1029/2001JB000561

Argand, E. (1922). La tectonique de l'Asie. Conférence faite á Bruxelles, le 10 août 1922. In *Congrès géologique international (XIIIe session)-belgique 1922* (pp. 171–372).

Armijo, R., Tapponnier, P., Mercier, J. L., & Han, T.-L. (1986). Quaternary extension in southern Tibet: Field observations and tectonic implications. *Journal of Geophysical Research*, *91*(B14), 13803–13872. https://doi.org/10.1029/JB091iB14p13803

Aslan, G., Lasserre, C., Cakir, Z., Ergintav, S., Özarpaci, S., Dogan, U., et al. (2019). Shallow creep along the 1999 Izmit earthquake rupture (Turkey) from GPS and high temporal resolution interferometric synthetic aperture radar data (2011–2017). *Journal of Geophysical Research: Solid Earth*, *124*(2), 2218–2236. https://doi.org/10.1029/2018JB017022

Avouac, J.-P., & Tapponnier, P. (1993). Kinematic model of active deformation in central Asia. *Geophysical Research Letters*, *20*(10), 895–898. https://doi.org/10.1029/93GL00128

Bahrouni, N., Masson, F., Meghraoui, M., Saleh, M., Maamri, R., Dhaha, F., & Arfaoui, M. (2020). Active tectonics and GPS data analysis of the Maghrebian thrust belt and Africa-Eurasia plate convergence in Tunisia. *Tectonophysics*, *785*, 228440. https://doi.org/10.1016/j.tecto.2020.228440

Bai, D., Unsworth, M. J., Meju, M. A., Ma, X., Teng, J., Kong, X., et al. (2010). Crustal deformation of the eastern Tibetan plateau revealed by magnetotelluric imaging. *Nature Geoscience*, *3*(5), 358–362. https://doi.org/10.1038/ngeo830

Barbot, S., & Weiss, J. (2021). Connecting subduction, extension and shear localization across the Aegean Sea and Anatolia. *Geophysical Journal International*, *226*(1), 422–445. https://doi.org/10.1093/gji/ggab078

Barnhart, W. D. (2017). Fault creep rates of the Chaman fault (Afghanistan and Pakistan) inferred from InSAR. *Journal of Geophysical Research: Solid Earth*, *122*(1), 372–386. https://doi.org/10.1002/2016JB013656

Barnhart, W. D., Hayes, G. P., Samsonov, S. V., Fielding, E. J., & Seidman, L. E. (2014). Breaking the oceanic lithosphere of a subducting slab: The 2013 Khash, Iran earthquake. *Geophysical Research Letters*, *41*(1), 32–36. https://doi.org/10.1002/2013GL058096

Beavan, J., & Haines, J. (2001). Contemporary horizontal velocity and strain rate fields of the Pacific-Australian plate boundary zone through New Zealand. *Journal of Geophysical Research*, *106*(B1), 741–770. https://doi.org/10.1029/2000jb900302

Becker, T. W., Conrad, C. P., Schaeffer, A. J., & Lebedev, S. (2014). Origin of azimuthal seismic anisotropy in oceanic plates and mantle. *Earth and Planetary Science Letters*, *401*, 236–250. https://doi.org/10.1016/j.epsl.2014.06.014

Becker, T. W., & Faccenna, C. (2011). Mantle conveyor beneath the Tethyan collisional belt. *Earth and Planetary Science Letters*, *310*(3), 453–461. https://doi.org/10.1016/j.epsl.2011.08.021

Becker, T. W., Kustowski, B., & Ekström, G. (2008). Radial seismic anisotropy as a constraint for upper mantle rheology. *Earth and Planetary Science Letters*, *267*, 213–237.

Becker, T. W., Lebedev, S., & Long, M. D. (2012). On the relationship between azimuthal anisotropy from shear wave splitting and surface wave tomography. *Journal of Geophysical Research*, *117*(B1). https://doi.org/10.1029/2011JB008705

Becker, T. W., Schulte-Pelkum, V., Blackman, D. K., Kellogg, J. B., & O'Connell, R. J. (2006). Mantle flow under the western United States from shear wave splitting. *Earth and Planetary Science Letters*, *247*(3), 235–251. https://doi.org/10.1016/j.epsl.2006.05.010

Bernard, R., Behr, W. M., Becker, T. W., & Young, D. (2019). Relationships between olivine CPO and deformation parameters in naturally deformed rocks and implications for mantle seismic anisotropy. *Geochemistry, Geophysics, Geosystems*, *20*(7), 3469–3494. https://doi.org/10.1029/2019gc008289

Bilham, R. (2006). Dangerous tectonics, fragile buildings, and tough decisions. *Science*, *311*(5769), 1873–1875. https://doi.org/10.1126/science.1125176

Bilham, R., Ozener, H., Mencin, D., Dogru, A., Ergintav, S., Cakir, Z., et al. (2016). Surface creep on the North Anatolian Fault at Ismetpasa, Turkey, 1944–2016. *Journal of Geophysical Research: Solid Earth*, *121*(10), 7409–7431. https://doi.org/10.1002/2016JB013394

Billi, A., Cuffaro, M., Orecchio, B., Palano, M., Presti, D., & Totaro, C. (2023). Retracing the Africa–Eurasia nascent convergent boundary in the Western Mediterranean based on earthquake and GNSS data. *Earth and Planetary Science Letters*, *601*, 117906. https://doi.org/10.1016/j.epsl.2022.117906

Bird, P. (2009). Long-term fault slip rates, distributed deformation rates, and forecast of seismicity in the western United States from joint fitting of community geologic, geodetic, and stress direction data sets. *Journal of Geophysical Research*, *114*(B11). https://doi.org/10.1029/2009JB006317

Biryol, C. B., Zandt, G., Beck, S. L., Ozacar, A. A., Adiyaman, H. E., & Gans, C. R. (2010). Shear wave splitting along a nascent plate boundary: The North Anatolian Fault Zone. *Geophysical Journal International*, *181*, 1201–1213.

Bletery, Q., Cavalié, O., Nocquet, J.-M., & Ragon, T. (2020). Distribution of interseismic coupling along the north and East anatolian faults inferred from InSAR and GPS data. *Geophysical Research Letters*, *47*(16), e2020GL087775. https://doi.org/10.1029/2020GL087775

Bonnin, M., Tommasi, A., Hassani, R., Chevrot, S., Wookey, J., & Barruol, G. (2012). Numerical modelling of the upper-mantle anisotropy beneath a migrating strike-slip plate boundary: The San Andreas Fault system. *Geophysical Journal International*, *191*(2), 436–458. https://doi.org/10.1111/j.1365-246x.2012.05650.x

Bougrine, A., Yelles-Chaouche, A. K., & Calais, E. (2019). Active deformation in Algeria from continuous GPS measurements. *Geophysical Journal International*, *217*(1), 572–588. https://doi.org/10.1093/gji/ggz035

Briole, P., Ganas, A., Elias, P., & Dimitrov, D. (2021). The GPS velocity field of the Aegean. New observations, contribution of the earthquakes, crustal blocks model. *Geophysical Journal International*, *226*(1), 468–492. https://doi.org/10.1093/gji/ggab089

Brockmann, E., Lutz, S., Zurutuza, J., Caporali, A., Lidberg, M., & Völksen, C. (2019). Towards a dense velocity field in Europe as a basis for maintaining the European reference frame. In *27th IUGG assembly*.

Brückl, E., Bleibinhaus, F., Gosar, A., Grad, M., Guterch, A., Hrubcová, P., et al. (2007). Crustal structure due to collisional and escape tectonics in the Eastern Alps region based on profiles Alp01 and Alp02 from the ALP 2002 seismic experiment. *Journal of Geophysical Research*, *112*(B6). https://doi.org/10.1029/2006JB004687

Cai, J., & Grafarend, E. W. (2007). Statistical analysis of geodetic deformation (strain rate) derived from the space geodetic measurements of BIFROST Project in Fennoscandia. *Journal of Geodynamics*, *43*(2), 214–238. https://doi.org/10.1016/j.jog.2006.09.010

Cakir, Z., Akoglu, A. M., Belabbes, S., Ergintav, S., & Meghraoui, M. (2005). Creeping along the Ismetpasa section of the North Anatolian fault (Western Turkey): Rate and extent from InSAR. *Earth and Planetary Science Letters*, *238*(1), 225–234. https://doi.org/10.1016/j.epsl.2005.06.044

Cakir, Z., Doğan, U., Akoğlu, A. M., Ergintav, S., Özarpacı, S., Özdemir, A., et al. (2023). Arrest of the Mw 6.8 January 24, 2020 Elaziğ (Turkey) earthquake by shallow fault creep. *Earth and Planetary Science Letters*, *608*, 118085. https://doi.org/10.1016/j.epsl.2023.118085

Çakir, Z., Ergintav, S., Özener, H., Dogan, U., Akoglu, A. M., Meghraoui, M., & Reilinger, R. (2012). Onset of aseismic creep on major strike-slip faults. *Geology*, *40*(12), 1115–1118. https://doi.org/10.1130/G33522.1

Carey, S. W. (1955). The orocline concept in geotectonics-part I. In *Papers and proceedings of the Royal Society of Tasmania*.

Carminati, E., Doglioni, C., & Scrocca, D. (2003). Apennines subduction-related subsidence of Venice (Italy). *Geophysical Research Letters*, *30*(13). https://doi.org/10.1029/2003GL017001

Castro-Perdomo, N. (2025). Supplementary material for "Strain Rates along the Alpine-Himalayan Belt from a Comprehensive GNSS Velocity Field" [Dataset]. *Zenodo*. https://doi.org/10.5281/zenodo.15186333

Castro-Perdomo, N. (2024). FICORO_GNSS: An open-source Python software package for filtering, combining and rotating GNSS velocity fields (Version 1.3.0) [Software]. *Zenodo*. https://doi.org/10.5281/zenodo.13921188

Castro-Perdomo, N., Viltres, R., Masson, F., Klinger, Y., Liu, S., Dhahry, M., et al. (2022). Interseismic deformation in the Gulf of Aqaba from GPS measurements. *Geophysical Journal International*, *228*(1), 477–492. https://doi.org/10.1093/gji/ggab353

Cavalié, O., & Jónsson, S. (2014). Block-like plate movements in eastern Anatolia observed by InSAR. *Geophysical Research Letters*, *41*(1), 26–31. https://doi.org/10.1002/2013GL058170

Cetin, E., Cakir, Z., Meghraoui, M., Ergintav, S., & Akoglu, A. M. (2014). Extent and distribution of aseismic slip on the Ismetpaşa segment of the North Anatolian Fault (Turkey) from Persistent Scatterer InSAR. *Geochemistry, Geophysics, Geosystems*, *15*(7), 2883–2894. https://doi.org/10.1002/2014GC005307

Chen, H., Qu, C., Zhao, D., Shan, X., Li, C., & Dal Zilio, L. (2024). Large-Scale extensional strain in Southern Tibet from Sentinel-1 InSAR and GNSS data. *Geophysical Research Letters*, *51*(19), e2024GL110512. https://doi.org/10.1029/2024GL110512

Chen, Q., Freymueller, J. T., Wang, Q., Yang, Z., Xu, C., & Liu, J. (2004). A deforming block model for the present-day tectonics of Tibet. *Journal of Geophysical Research*, *109*(B1). https://doi.org/10.1029/2002JB002151

Chousianitis, K., Sboras, S., Mouslopoulou, V., Chouliaras, G., & Hristopulos, D. T. (2024). The upper crustal deformation field of Greece inferred from GPS data and its correlation with earthquake occurrence. *Journal of Geophysical Research: Solid Earth*, *129*(4), e2023JB028004. https://doi.org/10.1029/2023JB028004

Christensen, N., & Crosson, R. (1968). Seismic anisotropy in the upper mantle. *Tectonophysics*, *6*(2), 93–107. https://doi.org/10.1016/0040-1951(68)90013-9

Clark, M. K., & Royden, L. H. (2000). Topographic ooze: Building the eastern margin of Tibet by lower crustal flow. *Geology*, *28*(8), 703–706. https://doi.org/10.1130/0091-7613(2000)028<0703:tobtem>2.3.co;2

Crameri, F. (2023). Scientific colour maps (Version 8.0.1) [Software]. *Zenodo*. https://doi.org/10.5281/zenodo.8409685

Danciu, L., Giardini, D., Weatherill, G., Basili, R., Nandan, S., Rovida, A., et al. (2024). The 2020 European seismic hazard model: Overview and results. *EGUsphere*, *2024*, 1–36. https://doi.org/10.5194/egusphere-2023-3062

Davis, P., England, P., & Houseman, G. (1997). Comparison of shear wave splitting and finite strain from the India-Asia collision zone. *Journal of Geophysical Research*, *102*(B12), 27511–27522. https://doi.org/10.1029/97JB02378

Dercourt, J. e. a., Zonenshain, L., Ricou, L.-E., Kazmin, V., Le Pichon, X., Knipper, A., et al. (1986). Geological evolution of the Tethys belt from the Atlantic to the Pamirs since the Lias. *Tectonophysics*, *123*(1–4), 241–315. https://doi.org/10.1016/0040-1951(86)90199-x

Devoti, R., d'Agostino, N., Serpelloni, E., Pietrantonio, G., Riguzzi, F., Avallone, A., et al. (2017). A combined velocity field of the Mediterranean region. *Annals of Geophysics*, *60*(2), S0215. https://doi.org/10.4401/ag-7059

DeVries, P. M., Krastev, P. G., Dolan, J. F., & Meade, B. J. (2017). Viscoelastic block models of the North Anatolian fault: A unified earthquake cycle representation of pre-and postseismic geodetic observations. *Bulletin of the Seismological Society of America*, *107*(1), 403–417. https://doi.org/10.1785/0120160059

Dziewonski, A. M., Chou, T.-A., & Woodhouse, J. H. (1981). Determination of earthquake source parameters from waveform data for studies of global and regional seismicity. *Journal of Geophysical Research*, *86*(B4), 2825–2852. https://doi.org/10.1029/jb086ib04p02825

Ekström, G., Nettles, M., & Dziewoński, A. (2012). The global CMT project 2004–2010: Centroid-moment tensors for 13,017 earthquakes. *Physics of the Earth and Planetary Interiors*, *200*, 1–9.

El-Fiky, G. S., & Kato, T. (1998). Continuous distribution of the horizontal strain in the Tohoku district, Japan, predicted by least-squares collocation. *Journal of Geodynamics*, *27*(2), 213–236. https://doi.org/10.1016/s0264-3707(98)00006-4

Endrun, B., Lebedev, S., Meier, T., Tirel, C., & Friederich, W. (2011). Complex layered deformation within the Aegean crust and mantle revealed by seismic anisotropy. *Nature Geoscience*, *4*(3), 203–207. https://doi.org/10.1038/ngeo1065

England, P., & Houseman, G. (1986). Finite strain calculations of continental deformation: 2. Comparison with the India-Asia Collision Zone. *Journal of Geophysical Research*, *91*(B3), 3664–3676. https://doi.org/10.1029/JB091iB03p03664

England, P., Houseman, G., & Nocquet, J.-M. (2016). Constraints from GPS measurements on the dynamics of deformation in Anatolia and the Aegean. *Journal of Geophysical Research: Solid Earth*, *121*(12), 8888–8916. https://doi.org/10.1002/2016jb013382

England, P., & Molnar, P. (2005). Late Quaternary to decadal velocity fields in Asia. *Journal of Geophysical Research*, *110*(B12). https://doi.org/10.1029/2004JB003541

Engwirda, D. (2009). Mesh2d-automatic mesh generation. available online on MatlabCentral: http://www.mathworks.com/matlabcentral/fileexchange/25555-mesh2d-automatic-mesh-generation

Ergintav, S., Floyd, M., Paradissis, D., Karabulut, H., Vernant, P., Masson, F., et al. (2023). New geodetic constraints on the role of faults and blocks vs. distribute strain in the nubia-arabia-eurasia zone of active plate interactions. *Turkish Journal of Earth Sciences*, *32*(3), 248–261. https://doi.org/10.55730/1300-0985.1842

Ergintav, S., McClusky, S., Hearn, E., Reilinger, R., Cakmak, R., Herring, T., et al. (2009). Seven years of postseismic deformation following the 1999, M = 7.4 and M = 7.2, Izmit-Düzce, Turkey earthquake sequence. *Journal of Geophysical Research*, *114*(B7). https://doi.org/10.1029/2008JB006021

Ergintav, S., Vernant, P., Tan, O., Karabulut, H., Özarpacı, S., Floyd, M., et al. (2024). Unexpected far-field deformation of the 2023 Kahramanmaraş earthquakes revealed by space geodesy. *Science*, *386*(6719), 328–335. https://doi.org/10.1126/science.ado4220

Faccenna, C., Becker, T. W., Auer, L., Billi, A., Boschi, L., Brun, J. P., et al. (2014). Mantle dynamics in the Mediterranean. *Reviews of Geophysics*, *52*(3), 283–332. https://doi.org/10.1002/2013RG000444

Faccenna, C., Becker, T. W., Jolivet, L., & Keskin, M. (2013). Mantle convection in the Middle East: Reconciling Afar upwelling, Arabia indentation and Aegean trench rollback. *Earth and Planetary Science Letters*, *375*, 254–269. https://doi.org/10.1016/j.epsl.2013.05.043

Faccenna, C., Becker, T. W., Miller, M. S., Serpelloni, E., & Willett, S. D. (2014). Isostasy, dynamic topography, and the elevation of the Apennines of Italy. *Earth and Planetary Science Letters*, *407*, 163–174. https://doi.org/10.1016/j.epsl.2014.09.027

Faccenna, C., Bellier, O., Martinod, J., Piromallo, C., & Regard, V. (2006). Slab detachment beneath eastern Anatolia: A possible cause for the formation of the North Anatolian fault. *Earth and Planetary Science Letters*, *242*(1–2), 85–97. https://doi.org/10.1016/j.epsl.2005.11.046

Faccenna, C., Molin, P., Orecchio, B., Olivetti, V., Bellier, O., Funiciello, F., et al. (2011). Topography of the Calabria subduction zone (southern Italy): Clues for the origin of mt. Etna. *Tectonics*, *30*(1). https://doi.org/10.1029/2010TC002694

Fang, J., Wright, T. J., Johnson, K. M., Ou, Q., Styron, R., Craig, T. J., et al. (2024). Strain partitioning in the Southeastern Tibetan Plateau from kinematic modeling of high-resolution Sentinel-1 InSAR and GNSS. *Geophysical Research Letters*, *51*(19), e2024GL111199. https://doi.org/10.1029/2024GL111199

Fattahi, H., & Amelung, F. (2016). InSAR observations of strain accumulation and fault creep along the Chaman Fault system, Pakistan and Afghanistan. *Geophysical Research Letters*, *43*(16), 8399–8406. https://doi.org/10.1002/2016GL070121

Fischer, K. M., & Wiens, D. A. (1996). The depth distribution of mantle anisotropy beneath the Tonga subduction zone. *Earth and Planetary Science Letters*, *142*(1–2), 253–260. https://doi.org/10.1016/0012-821x(96)00084-2

Flerit, F., Armijo, R., King, G., & Meyer, B. (2004). The mechanical interaction between the propagating North Anatolian Fault and the back-arc extension in the Aegean. *Earth and Planetary Science Letters*, *224*(3–4), 347–362. https://doi.org/10.1016/j.epsl.2004.05.028

Flesch, L. M., Haines, A. J., & Holt, W. E. (2001). Dynamics of the India-Eurasia collision zone. *Journal of Geophysical Research*, *106*(B8), 16435–16460. https://doi.org/10.1029/2001JB000208

Flesch, L. M., Holt, W. E., Haines, A. J., Wen, L., & Shen-Tu, B. (2007). The dynamics of western North America: Stress magnitudes and the relative role of gravitational potential energy, plate interaction at the boundary and basal tractions. *Geophysical Journal International*, *169*(3), 866–896. https://doi.org/10.1111/j.1365-246X.2007.03274.x

Flesch, L. M., Holt, W. E., Silver, P. G., Stephenson, M., Wang, C.-Y., & Chan, W. W. (2005). Constraining the extent of crust–mantle coupling in central Asia using GPS, geologic, and shear wave splitting data. *Earth and Planetary Science Letters*, *238*(1), 248–268. https://doi.org/10.1016/j.epsl.2005.06.023

Floyd, M., King, R., Paradissis, D., Karabulut, H., Ergintav, S., Raptakis, K., & Reilinger, R. (2023). Variations in coupling and deformation along the Hellenic subduction zone. *Turkish Journal of Earth Sciences*, *32*(3), 262–274. https://doi.org/10.55730/1300-0985.1843

Fouch, M. J., & Rondenay, S. (2006). Seismic anisotropy beneath stable continental interiors. *Physics of the Earth and Planetary Interiors*, *158*(2–4), 292–320. https://doi.org/10.1016/j.pepi.2006.03.024

Fox, M., Herman, F., Kissling, E., & Willett, S. D. (2015). Rapid exhumation in the Western Alps driven by slab detachment and glacial erosion. *Geology*, *43*(5), 379–382. https://doi.org/10.1130/G36411.1

Frohlich, C., & Davis, S. D. (1999). How well constrained are well-constrained T, B, and P axes in moment tensor catalogs? *Journal of Geophysical Research*, *104*(B3), 4901–4910. https://doi.org/10.1029/1998JB900071

Fukuda, J., & Johnson, K. M. (2021). Bayesian inversion for a stress-driven model of afterslip and viscoelastic relaxation: Method and application to postseismic deformation following the 2011 M 9.0 tohoku-oki earthquake. *Journal of Geophysical Research: Solid Earth*, *126*(5), e2020JB021620. https://doi.org/10.1029/2020JB021620

Gan, W., Zhang, P., Shen, Z.-K., Niu, Z., Wang, M., Wan, Y., et al. (2007). Present-day crustal motion within the Tibetan Plateau inferred from GPS measurements. *Journal of Geophysical Research*, *112*(B8). https://doi.org/10.1029/2005JB004120

Gao, S., Davis, P. M., Liu, H., Slack, P. D., Zorin, Y. A., Mordvinova, V. V., et al. (1994). Seismic anisotropy and mantle flow beneath the Baikal rift zone. *Nature*, *371*(6493), 149–151. https://doi.org/10.1038/371149a0

Gomez, F., Cochran, W. J., Yassminh, R., Jaafar, R., Reilinger, R., Floyd, M., et al. (2020). Fragmentation of the Sinai Plate indicated by spatial variation in present-day slip rate along the Dead Sea Fault System. *Geophysical Journal International*, *221*(3), 1913–1940. https://doi.org/10.1093/gji/ggaa095

Gomez, F., Khawlie, M., Tabet, C., Nasser Darkal, A., Khair, K., & Barazangi, M. (2006). Late Cenozoic uplift along the northern Dead Sea transform in Lebanon and Syria. *Earth and Planetary Science Letters*, *241*(3), 913–931. https://doi.org/10.1016/j.epsl.2005.10.029

Graham, S. E., Loveless, J. P., & Meade, B. J. (2018). Global plate motions and earthquake cycle effects. *Geochemistry, Geophysics, Geosystems*, *19*(7), 2032–2048. https://doi.org/10.1029/2017gc007391

Güvercin, S. E., Karabulut, H., Konca, A. Ö., Doğan, U., & Ergintav, S. (2022). 02). Active seismotectonics of the East Anatolian Fault. *Geophysical Journal International*, *230*(1), 50–69. https://doi.org/10.1093/gji/ggac045

Haines, A., & Holt, W. (1993). A procedure for obtaining the complete horizontal motions within zones of distributed deformation from the inversion of strain rate data. *Journal of Geophysical Research*, *98*(B7), 12057–12082. https://doi.org/10.1029/93jb00892

Haines, A. J., Dimitrova, L. L., Wallace, L. M., & Williams, C. A. (2015). *Enhanced surface imaging of crustal deformation: Obtaining tectonic force fields using GPS data*. Springer.

Hamiel, Y., & Piatibratova, O. (2021). Spatial variations of slip and creep rates along the southern and central Dead Sea Fault and the Carmel–Gilboa Fault System. *Journal of Geophysical Research: Solid Earth*, *126*(9), e2020JB021585. https://doi.org/10.1029/2020jb021585

Hamiel, Y., Piatibratova, O., & Mizrahi, Y. (2016). Creep along the northern Jordan Valley section of the Dead Sea Fault. *Geophysical Research Letters*, *43*(6), 2494–2501. https://doi.org/10.1002/2016GL067913

Hardebeck, J. L., & Michael, A. J. (2004). Stress orientations at intermediate angles to the San Andreas Fault, California. *Journal of Geophysical Research*, *109*(B11). https://doi.org/10.1029/2004JB003239

Hartog, R., & Schwartz, S. Y. (2001). Depth-dependent mantle anisotropy below the San Andreas fault system: Apparent splitting parameters and waveforms. *Journal of Geophysical Research*, *106*(B3), 4155–4167. https://doi.org/10.1029/2000JB900382

Hatzfeld, D., Karagianni, E., Kassaras, I., Kiratzi, A., Louvari, E., Lyon-Caen, H., et al. (2001). Shear wave anisotropy in the upper mantle beneath the Aegean related to internal deformation. *Journal of Geophysical Research*, *106*(B12), 30737–30753. https://doi.org/10.1029/2001JB000387

Hatzfeld, D., & Molnar, P. (2010). Comparisons of the kinematics and deep structures of the Zagros and Himalaya and of the Iranian and Tibetan plateaus and geodynamic implications. *Review of Geophysics*, *48*(RG2005). https://doi.org/10.1029/2009RG000304

Hayes, G. P., Moore, G. L., Portner, D. E., Hearne, M., Flamme, H., Furtney, M., & Smoczyk, G. M. (2018). Slab2, a comprehensive subduction zone geometry model. *Science*, *362*(6410), 58–61. https://doi.org/10.1126/science.aat4723

He, P., Wen, Y., Zhong, Y., & Cai, J. (2024). Nonoverlapped sources of the devastating 2023 Mw>6 Herat, Afghanistan, earthquake swarm estimated by InSAR. *Seismological Research Letters*, *96*(2A), 838–847. https://doi.org/10.1785/0220240239

He, X., Zhao, L.-F., Xie, X.-B., Tian, X., & Yao, Z.-X. (2021). Weak crust in Southeast Tibetan Plateau revealed by Lg-Wave attenuation tomography: Implications for crustal material escape. *Journal of Geophysical Research: Solid Earth*, *126*(3), e2020JB020748. https://doi.org/10.1029/2020JB020748

Hearn, E. H., McClusky, S., Ergintav, S., & Reilinger, R. E. (2009). Izmit earthquake postseismic deformation and dynamics of the North Anatolian Fault Zone. *Journal of Geophysical Research*, *114*(B8). https://doi.org/10.1029/2008JB006026

Heidbach, O. (2005). Velocity field of the Aegean-Anatolian region from 3D finite element models. In F. Wenzel (Ed.), *Perspectives in modern seismology* (pp. 169–185). Springer.

Heidbach, O., Rajabi, M., Di Giacomo, D., Harris, J., Lammers, S., Morawietz, S., et al. (2025). World Stress Map 2025 [Dataset]. *GFZ Data Services*. https://doi.org/10.5880/WSM.2025.002

Holt, W. E. (1995). Flow fields within the Tonga slab determined from the moment tensors of deep earthquakes. *Geophysical Research Letters*, *22*(8), 989–992. https://doi.org/10.1029/95gl00786

Holt, W. E. (2000). 01). Correlated crust and mantle strain fields in Tibet. *Geology*, *28*(1), 67–70. https://doi.org/10.1130/0091-7613(2000)028<0067:ccamsf>2.3.co;2

Holt, W. E., Chamot-Rooke, N., Le Pichon, X., Haines, A. J., Shen-Tu, B., & Ren, J. (2000). Velocity field in Asia inferred from Quaternary fault slip rates and Global Positioning System observations. *Journal of Geophysical Research*, *105*(B8), 19185–19209. https://doi.org/10.1029/2000JB900045

Holt, W. E., Ni, J. F., Wallace, T. C., & Haines, A. J. (1991). The active tectonics of the eastern Himalayan syntaxis and surrounding regions. *Journal of Geophysical Research*, *96*(B9), 14595–14632. https://doi.org/10.1029/91JB01021

Hou, Z., Liu, L., Zhang, H., Xu, B., Wang, Q., Yang, T., et al. (2024). Cenozoic eastward growth of the Tibetan Plateau controlled by tearing of the Indian slab. *Nature Geoscience*, *17*(3), 255–263. https://doi.org/10.1038/s41561-024-01382-9

Houseman, G., & England, P. (1993). Crustal thickening versus lateral expulsion in the Indian-Asian continental collision. *Journal of Geophysical Research*, *98*(B7), 12233–12249. https://doi.org/10.1029/93JB00443

Huang, X., Li, Y., Shan, X., Zhao, D., Gao, Z., Gong, W., & Qu, C. (2023a). 06). InSAR observations reveal variations in shallow creep on the kangding segment of the xianshuihe fault. *Seismological Research Letters*, *94*(5), 2291–2300. https://doi.org/10.1785/0220230053

Huang, X., Li, Y., Shan, X., Zhao, D., Gao, Z., Gong, W., & Qu, C. (2023b). 06). InSAR observations reveal variations in shallow creep on the kangding segment of the xianshuihe fault. *Seismological Research Letters*, *94*(5), 2291–2300. https://doi.org/10.1785/0220230053

Huang, Z., Zhou, Y., & Zhang, P. (2023). Newly discovered shallow creep along the Gozha Co fault in northwestern Tibet: Spatial extent, rate and temporal evolution. *Earth and Planetary Science Letters*, *621*, 118388. https://doi.org/10.1016/j.epsl.2023.118388

Hussain, E., Hooper, A., Wright, T. J., Walters, R. J., & Bekaert, D. P. S. (2016). Interseismic strain accumulation across the central North Anatolian Fault from iteratively unwrapped InSAR measurements. *Journal of Geophysical Research: Solid Earth*, *121*(12), 9000–9019. https://doi.org/10.1002/2016JB013108

Hussain, E., Wright, T. J., Walters, R. J., Bekaert, D. P., Lloyd, R., & Hooper, A. (2018). Constant strain accumulation rate between major earthquakes on the North Anatolian Fault. *Nature Communications*, *9*(1), 1392. https://doi.org/10.1038/s41467-018-03739-2

Ismail-Zadeh, A., Adamia, S., Chabukiani, A., Chelidze, T., Cloetingh, S., Floyd, M., et al. (2020). Geodynamics, seismicity, and seismic hazards of the caucasus. *Earth-Science Reviews*, *207*, 103222. https://doi.org/10.1016/j.earscirev.2020.103222

Jackson, J., & McKenzie, D. (1984). 04). Active tectonics of the Alpine—Himalayan Belt between western Turkey and Pakistan. *Geophysical Journal International*, *77*(1), 185–264. https://doi.org/10.1111/j.1365-246X.1984.tb01931.x

Jenny, S., Goes, S., Giardini, D., & Kahle, H.-G. (2004). Earthquake recurrence parameters from seismic and geodetic strain rates in the eastern Mediterranean. *Geophysical Journal International*, *157*(3), 1331–1347. https://doi.org/10.1111/j.1365-246x.2004.02261.x

Johansson, J. M., Davis, J. L., Scherneck, H.-G., Milne, G. A., Vermeer, M., Mitrovica, J. X., et al. (2002). Continuous GPS measurements of postglacial adjustment in Fennoscandia 1. Geodetic results. *Journal of Geophysical Research*, *107*(B8), ETG3-1–27. https://doi.org/10.1029/2001JB000400

Johnson, K. M. (2023). BforStrain (version 1.1.0) [Software]. *Zenodo*. https://doi.org/10.5281/zenodo.8139779

Johnson, K. M. (2024). Disagreements in geodetically inferred strain rates in the Western US with stress orientations and geologic moment rates. *Journal of Geophysical Research: Solid Earth*, *129*(4), e2023JB027472. https://doi.org/10.1029/2023jb027472

Johnson, K. M., Hammond, W. C., Weldon, I., & Ray, J. (2024). Review of geodetic and geologic deformation models for 2023 U.S. national seismic hazard model. *Bulletin of the Seismological Society of America*, *114*(3), 1407–1436. https://doi.org/10.1785/0120230137

Jolivet, L., Faccenna, C., Becker, T., Tesauro, M., Sternai, P., & Bouilhol, P. (2018). Mantle flow and deforming continents: From India-Asia convergence to Pacific subduction. *Tectonics*, *37*(9), 2887–2914. https://doi.org/10.1029/2018TC005036

Jolivet, L., Faccenna, C., Huet, B., Labrousse, L., Le Pourhiet, L., Lacombe, O., et al. (2013). Aegean tectonics: Strain localisation, slab tearing and trench retreat. *Tectonophysics*, *597–598*, 1–33. (The Aegean: a natural laboratory for tectonics - Neotectonics). https://doi.org/10.1016/j.tecto.2012.06.011

Jolivet, L., Faccenna, C., & Piromallo, C. (2009). From mantle to crust: Stretching the Mediterranean. *Earth and Planetary Science Letters*, *285*(1), 198–209. https://doi.org/10.1016/j.epsl.2009.06.017

Jolivet, R., Jara, J., Dalaison, M., Rouet-Leduc, B., Özdemir, A., Dogan, U., et al. (2023). Daily to Centennial behavior of Aseismic slip along the central section of the north anatolian fault. *Journal of Geophysical Research: Solid Earth*, *128*(7), e2022JB026018. (e2022JB026018 2022JB026018). https://doi.org/10.1029/2022JB026018

Jónsson, S. (2008). Importance of post-seismic viscous relaxation in southern Iceland. *Nature Geoscience*, *1*(2), 136–139. https://doi.org/10.1038/ngeo105

Kadirov, F., Guliyev, I., Feyzullayev, A., Safarov, R., Mammadov, S., Babayev, G., & Rashidov, T. (2014). GPS-based crustal deformations in Azerbaijan and their influence on seismicity and mud volcanism. *Izvestiya—Physics of the Solid Earth*, *50*(6), 814–823. https://doi.org/10.1134/s1069351314060020

Kahle, H.-G., Straub, C., Reilinger, R., McClusky, S., King, R., Hurst, K., et al. (1998). The strain rate field in the eastern Mediterranean region, estimated by repeated GPS measurements. *Tectonophysics*, *294*(3–4), 237–252. https://doi.org/10.1016/s0040-1951(98)00102-4

Kaneko, Y., Fialko, Y., Sandwell, D. T., Tong, X., & Furuya, M. (2013). Interseismic deformation and creep along the central section of the North Anatolian Fault (Turkey): InSAR observations and implications for rate-and-state friction properties. *Journal of Geophysical Research: Solid Earth*, *118*(1), 316–331. https://doi.org/10.1029/2012JB009661

Karakhanyan, A., Vernant, P., Doerflinger, E., Avagyan, A., Philip, H., Aslanyan, R., et al. (2013). GPS constraints on continental deformation in the Armenian region and Lesser Caucasus. *Tectonophysics*, *592*, 39–45. https://doi.org/10.1016/j.tecto.2013.02.002

Kendall, J.-M., Pilidou, S., Keir, D., Bastow, I., Stuart, G., & Ayele, A. (2006). Mantle upwellings, melt migration and the rifting of Africa: Insights from seismic anisotropy. *Geol. Soc., London, Spec. Pub.*, *259*(1), 55–72. https://doi.org/10.1144/gsl.sp.2006.259.01.06

Khorrami, F., Vernant, P., Masson, F., Nilfouroushan, F., Mousavi, Z., Nankali, H., et al. (2019). An up-to-date crustal deformation map of Iran using integrated campaign-mode and permanent GPS velocities. *Geophysical Journal International*, *217*(2), 832–843. https://doi.org/10.1093/gji/ggz045

Kong, F., Wu, J., Liu, L., Liu, K. H., Song, J., Li, J., & Gao, S. S. (2018). Azimuthal anisotropy and mantle flow underneath the southeastern Tibetan Plateau and northern Indochina Peninsula revealed by shear wave splitting analyses. *Tectonophysics*, *747–748*, 68–78. https://doi.org/10.1016/j.tecto.2018.09.013

Kostrov, V. (1974). Seismic moment and enengy of earthquakes, and the seismic flow of rock. *Izv. Acad. Sci. USSR. Phys. Solid Earth*, *1*, 23–44.

Kreemer, C., Blewitt, G., & Davis, P. M. (2020). Geodetic evidence for a buoyant mantle plume beneath the Eifel volcanic area, NW Europe. *Geophysical Journal International*, *222*(2), 1316–1332. https://doi.org/10.1093/gji/ggaa227

Kreemer, C., Blewitt, G., & Hammond, W. C. (2009). Geodetic constraints on contemporary deformation in the northern Walker Lane: 2. Velocity and strain rate tensor analysis. In *Late cenozoic structure and evolution of the great basin-sierra nevada transition*. Geological Society of America. https://doi.org/10.1130/2009.2447(02

Kreemer, C., Blewitt, G., & Klein, E. C. (2014). A geodetic plate motion and Global Strain Rate Model. *Geochemistry, Geophysics, Geosystems*, *15*(10), 3849–3889. https://doi.org/10.1002/2014GC005407

Kreemer, C., & Chamot-Rooke, N. (2004). Contemporary kinematics of the southern Aegean and the Mediterranean Ridge. *Geophysical Journal International*, *157*(3), 1377–1392. https://doi.org/10.1111/j.1365-246X.2004.02270.x

Kreemer, C., Chamot-Rooke, N., & Le Pichon, X. (2004). Constraints on the evolution and vertical coherency of deformation in the Northern Aegean from a comparison of geodetic, geologic and seismologic data. *Earth and Planetary Science Letters*, *225*(3), 329–346. https://doi.org/10.1016/j.epsl.2004.06.018

Kreemer, C., Hammond, W. C., & Blewitt, G. (2018). A Robust estimation of the 3-D intraplate deformation of the north American plate from GPS. *Journal of Geophysical Research: Solid Earth*, *123*(5), 4388–4412. https://doi.org/10.1029/2017JB015257

Kreemer, C., Lavallée, D. A., Blewitt, G., & Holt, W. E. (2006). On the stability of a geodetic no-net-rotation frame and its implication for the International Terrestrial Reference Frame. *Geophysical Research Letters*, *33*(17). https://doi.org/10.1029/2006GL027058

Kuhlemann, J., Frisch, W., Székely, B., Dunkl, I., & Kazmer, M. (2002). Post-collisional sediment budget history of the Alps: Tectonic versus climatic control. *International Journal of Earth Sciences*, *91*(5), 818–837. https://doi.org/10.1007/s00531-002-0266-y

Kurt, A. I., Ozbakir, A. D., Ergintav, S., Dogan, U., & Ozarpaci, S. (2023). Contemporary velocity field for Turkey inferred from combination of a dense network of long term GNSS observations. *Turkish Journal of Earth Sciences*, *32*(3), 275–293. https://doi.org/10.55730/1300-0985.1844

Lazecký, M., Spaans, K., González, P. J., Maghsoudi, Y., Morishita, Y., Albino, F., et al. (2020). LiCSAR: An automatic InSAR tool for measuring and monitoring tectonic and volcanic activity. *Remote Sensing*, *12*(15), 2430. https://doi.org/10.3390/rs12152430

León Soto, G., Sandvol, E., Ni, J. F., Flesch, L., Hearn, T. M., Tilmann, F., et al. (2012). Significant and vertically coherent seismic anisotropy beneath eastern Tibet. *Journal of Geophysical Research*, *117*(B5). https://doi.org/10.1029/2011JB008919

Le Pichon, X., & Angelier, J. (1979). The Hellenic arc and trench system: A key to the neotectonic evolution of the eastern Mediterranean area. *Tectonophysics*, *60*(1–2), 1–42. https://doi.org/10.1016/0040-1951(79)90131-8

Le Pichon, X., & Kreemer, C. (2010). The miocene-to-present kinematic evolution of the Eastern mediterranean and Middle East and its implications for dynamics. *Annual Review of Earth and Planetary Sciences*, *38*(1), 323–351. https://doi.org/10.1146/annurev-earth-040809-152419

Lev, E., Long, M. D., & van der Hilst, R. D. (2006). Seismic anisotropy in Eastern Tibet from shear wave splitting reveals changes in lithospheric deformation. *Earth and Planetary Science Letters*, *251*(3), 293–304. https://doi.org/10.1016/j.epsl.2006.09.018

Li, A., & Chen, C. (2006). Shear wave splitting beneath the central Tien Shan and tectonic implications. *Geophysical Research Letters*, *33*(22). https://doi.org/10.1029/2006GL027717

Li, X., Jónsson, S., Liu, S., Ma, Z., Castro-Perdomo, N., Cesca, S., et al. (2024). Resolving the slip-rate inconsistency of the northern Dead Sea fault. *Science Advances*, *10*(11), eadj8408. https://doi.org/10.1126/sciadv.adj8408

Li, Y., Nocquet, J.-M., Shan, X., & Jian, H. (2021). Heterogeneous interseismic coupling along the Xianshuihe-Xiaojiang fault System, Eastern Tibet. *Journal of Geophysical Research: Solid Earth*, *126*(11), e2020JB021187. https://doi.org/10.1029/2020JB021187

Li, Y., Nocquet, J.-M., Shan, X., & Song, X. (2021). Geodetic observations of shallow creep on the Laohushan-Haiyuan fault, Northeastern Tibet. *Journal of Geophysical Research: Solid Earth*, *126*(6), e2020JB021576. https://doi.org/10.1029/2020JB021576

Li, Y., Shan, X., Qu, C., Zhang, G., Wang, X., & Xiong, H. (2025). Slip deficit rate and seismic potential on crustal faults in Tibet. *Geophysical Research Letters*, *52*(1), e2024GL112122. https://doi.org/10.1029/2024GL112122

Liang, S., Gan, W., Shen, C., Xiao, G., Liu, J., Chen, W., et al. (2013). Three-dimensional velocity field of present-day crustal motion of the Tibetan Plateau derived from GPS measurements. *Journal of Geophysical Research: Solid Earth*, *118*(10), 5722–5732. https://doi.org/10.1002/2013jb010503

Lin, Y., & Zhao, L. (2024). Upper-Mantle anisotropy in the Southeastern Margin of Tibetan Plateau revealed by fullwave SKS splitting intensity tomography. *Journal of Geophysical Research: Solid Earth*, *129*(3), e2023JB027629. https://doi.org/10.1029/2023JB027629

Lindsey, E. O., Wang, Y., Aung, L. T., Chong, J.-H., Qiu, Q., Mallick, R., et al. (2023). Active subduction and strain partitioning in western Myanmar revealed by a dense survey GNSS network. *Earth and Planetary Science Letters*, *622*, 118384. https://doi.org/10.1016/j.epsl.2023.118384

Lippitsch, R., Kissling, E., & Ansorge, J. (2003). Upper mantle structure beneath the Alpine orogen from high-resolution teleseismic tomography. *Journal of Geophysical Research*, *108*(B8). https://doi.org/10.1029/2002JB002016

Liu, S., Shen, Z.-K., Bürgmann, R., & Jónsson, S. (2020). Thin crème brûlée rheological structure for the Eastern California Shear Zone. *Geology*, *49*(2), 216–221. https://doi.org/10.1130/G47729.1

Liu, S., Xu, X., Nocquet, J.-M., Chen, G., Tan, X., Jónsson, S., & Klinger, Y. (2025). Lower crustal thickening drives active uplift in Northern Tibet. *Earth and Planetary Science Letters*, *655*, 119245. https://doi.org/10.1016/j.epsl.2025.119245

Liu, Z., Luo, H., Klinger, Y., & Wang, T. (2025). Shear strain evolution spanning the 2020 Mw6.8 Elazığ and 2023 Mw7.8/Mw7.6 Kahramanmaraş earthquake sequence along the east Anatolian Fault Zone. *Geophysical Research Letters*, *52*(6), e2024GL114033. https://doi.org/10.1029/2024GL114033

Liu, Z., & Wang, T. (2023). High-Resolution interseismic strain mapping from InSAR phase-gradient stacking: Application to the north anatolian fault with implications for the non-uniform strain distribution related to coseismic slip distribution. *Geophysical Research Letters*, *50*(15), e2023GL104168. https://doi.org/10.1029/2023GL104168

Loveless, J., & Meade, B. (2011). Partitioning of localized and diffuse deformation in the Tibetan Plateau from joint inversions of geologic and geodetic observations. *Earth and Planetary Science Letters*, *303*(1), 11–24. https://doi.org/10.1016/j.epsl.2010.12.014

Luo, H., & Wang, K. (2022). Finding simplicity in the complexity of postseismic coastal uplift and subsidence following great subduction earthquakes. *Journal of Geophysical Research: Solid Earth*, *127*(10), e2022JB024471. https://doi.org/10.1029/2022JB024471

Mai, P. M., Aspiotis, T., Aquib, T. A., Cano, E. V., Castro-Cruz, D., Espindola-Carmona, A., et al. (2023). 05). The Destructive Earthquake Doublet of 6 February 2023 in South-Central Türkiye and Northwestern Syria: Initial Observations and Analyses. *The Seismic Record*, *3*(2), 105–115. https://doi.org/10.1785/0320230007

Makeyeva, L., Vinnik, L., & Roecker, S. (1992). Shear-wave splitting and small-scale convection in the continental upper mantle. *Nature*, *358*(6382), 144–147. https://doi.org/10.1038/358144a0

Malinverno, A., & Ryan, W. B. F. (1986). Extension in the Tyrrhenian Sea and shortening in the Apennines as result of arc migration driven by sinking of the lithosphere. *Tectonics*, *5*(2), 227–245. https://doi.org/10.1029/TC005i002p00227

Mallick, R., Hubbard, J. A., Lindsey, E. O., Bradley, K. E., Moore, J. D., Ahsan, A., et al. (2020). Subduction initiation and the rise of the Shillong Plateau. *Earth and Planetary Science Letters*, *543*, 116351. https://doi.org/10.1016/j.epsl.2020.116351

Maurer, J., & Materna, K. (2023). Quantification of geodetic strain rate uncertainties and implications for seismic hazard estimates. *Geophysical Journal International*, *234*(3), 2128–2142. https://doi.org/10.1093/gji/ggad191

McClusky, S., Balassanian, S., Barka, A., Demir, C., Ergintav, S., Georgiev, I., et al. (2000). Global Positioning System constraints on plate kinematics and dynamics in the eastern Mediterranean and Caucasus. *Journal of Geophysical Research*, *105*(B3), 5695–5719. https://doi.org/10.1029/1999JB900351

McClusky, S., Reilinger, R., Ogubazghi, G., Amleson, A., Healeb, B., Vernant, P., et al. (2010). Kinematics of the southern Red Sea–Afar Triple Junction and implications for plate dynamics. *Geophysical Research Letters*, *37*(5). https://doi.org/10.1029/2009gl041127

McKenzie, D. (1978). Active tectonics of the Alpine—Himalayan belt: The Aegean Sea and surrounding regions. *Geophysical Journal International*, *55*(1), 217–254. https://doi.org/10.1111/j.1365-246X.1978.tb04759.x

McKenzie, D., & Yılmaz, Y. (1991). Deformation and volcanism in western Turkey and the Aegean. *Bulletin of the Technical University of Istanbul*, *44*(1–2), 345–373.

McKenzie, D. P. (1969). The relation between fault plane solutions for earthquakes and the directions of the principal stresses. *Bulletin of the Seismological Society of America*, *59*(2), 591–601. https://doi.org/10.1785/bssa0590020591

McNamara, D. E., Owens, T. J., Silver, P. G., & Wu, F. T. (1994). Shear wave anisotropy beneath the Tibetan Plateau. *Journal of Geophysical Research*, *99*(B7), 13655–13665. https://doi.org/10.1029/93JB03406

Meade, B. J. (2007). Present-day kinematics at the India-Asia collision zone. *Geology*, *35*(1), 81–84. https://doi.org/10.1130/G22924A.1

Merry, T. A. J., Bastow, I. D., Kounoudis, R., Ogden, C. S., Bell, R. E., & Jones, L. (2021). The influence of the north anatolian fault and a fragmenting slab Architecture on upper mantle Seismic Anisotropy in the Eastern mediterranean. *Geochemistry, Geophysics, Geosystems*, *22*(9), e2021GC009896. https://doi.org/10.1029/2021GC009896

Mey, J., Scherler, D., Wickert, A. D., Egholm, D. L., Tesauro, M., Schildgen, T. F., & Strecker, M. R. (2016). Glacial isostatic uplift of the European Alps. *Nature Communications*, *7*(1), 13382. https://doi.org/10.1038/ncomms13382

Michael, A. J. (1987). Use of focal mechanisms to determine stress: A control study. *Journal of Geophysical Research: Solid Earth*, *92*(B1), 357–368. https://doi.org/10.1029/jb092ib01p00357

Milne, G. A., Davis, J. L., Mitrovica, J. X., Scherneck, H.-G., Johansson, J. M., Vermeer, M., & Koivula, H. (2001). Space-Geodetic constraints on glacial isostatic adjustment in fennoscandia. *Science*, *291*(5512), 2381–2385. https://doi.org/10.1126/science.1057022

Molnar, P., England, P., & Martinod, J. (1993). Mantle dynamics, uplift of the Tibetan Plateau, and the Indian Monsoon. *Reviews of Geophysics*, *31*(4), 357–396. https://doi.org/10.1029/93RG02030

Molnar, P., & Lyon-Caen, H. (1988). Some simple physical aspects of the support, structure, and evolution of mountain belts. In *Processes in Continental lithospheric deformation*. Geological Society of America. https://doi.org/10.1130/SPE218-p179

Molnar, P., & Tapponnier, P. (1975). Cenozoic tectonics of Asia: Effects of a Continental collision. *Science*, *189*(4201), 419–426. https://doi.org/10.1126/science.189.4201.419

Mumladze, T., Forte, A. M., Cowgill, E. S., Trexler, C. C., Niemi, N. A., Burak Yıkılmaz, M., & Kellogg, L. H. (2015). Subducted, detached, and torn slabs beneath the Greater Caucasus. *GeoResJ*, *5*, 36–46. https://doi.org/10.1016/j.grj.2014.09.004

Nicolas, A., & Christensen, N. I. (1987). Formation of Anisotropy in upper mantle Peridotites: A review. In *Composition, structure and dynamics of the lithosphere-asthenosphere System* (pp. 111–123). American Geophysical Union (AGU). https://doi.org/10.1029/GD016p0111

Nocquet, J.-M. (2012). Present-day kinematics of the Mediterranean: A comprehensive overview of GPS results. *Tectonophysics*, *579*, 220–242. https://doi.org/10.1016/j.tecto.2012.03.037

Nocquet, J.-M., Sue, C., Walpersdorf, A., Tran, T., Lenôtre, N., Vernant, P., et al. (2016). Present-day uplift of the western Alps. *Scientific Reports*, *6*(1), 28404. https://doi.org/10.1038/srep28404

Nucci, R., Serpelloni, E., Faenza, L., Garcia, A., & Belardinelli, M. E. (2025). Geodetic strain rates and seismicity rates along the Apennines (Italy). *Journal of Geophysical Research: Solid Earth*, *130*(2), e2024JB029848. https://doi.org/10.1029/2024JB029848

Okazaki, T., Fukahata, Y., & Nishimura, T. (2021). Consistent estimation of strain-rate fields from GNSS velocity data using basis function expansion with ABIC. *Earth Planets and Space*, *73*, 1–22. https://doi.org/10.1186/s40623-021-01474-5

Ou, Q., Daout, S., Weiss, J. R., Shen, L., Lazecký, M., Wright, T. J., & Parsons, B. E. (2022). Large-Scale interseismic strain mapping of the NE Tibetan Plateau from Sentinel-1 interferometry. *Journal of Geophysical Research: Solid Earth*, *127*(6), e2022JB024176. https://doi.org/10.1029/2022JB024176

Özalaybey, S., & Savage, M. K. (1995). Shear-wave splitting beneath western United States in relation to plate tectonics. *Journal of Geophysical Research*, *100*(B9), 18135–18149. https://doi.org/10.1029/95JB00715

Özarpacı, S., Doğan, U., Ergintav, S., Çakır, Z., Özdemir, A., Floyd, M., & Reilinger, R. (2021). Present GPS velocity field along 1999 Izmit rupture zone: Evidence for continuing afterslip 20 yr after the earthquake. *Geophysical Journal International*, *224*(3), 2016–2027.

Özbey, V., Sengör, A. M. C., Henry, P., Özeren, M. S., Haines, A. J., Klein, E. C., et al. (2024). Kinematics of the Kahramanmaraş triple junction and of Cyprus: Evidence of shear partitioning. *BSGF - Earth Sciences Bulletin*, *195*, 15. https://doi.org/10.1051/bsgf/2024012

Özdemir, S., & Karslıoğlu, M. O. (2019). Soft clustering of GPS velocities from a homogeneous permanent network in Turkey. *Journal of Geodesy*, *93*(8), 1171–1195. https://doi.org/10.1007/s00190-019-01235-z

Özkan, A., Yavaşoğlu, H. H., & Masson, F. (2023). Present-day strain accumulations and fault kinematics at the Hatay Triple Junction using new geodetic constraints. *Tectonophysics*, *854*, 229819. https://doi.org/10.1016/j.tecto.2023.229819

Pagani, C., Bodin, T., Métois, M., & Lasserre, C. (2021). Bayesian estimation of surface strain rates from global navigation satellite system measurements: Application to the southwestern United States. *Journal of Geophysical Research: Solid Earth*, *126*(6), e2021JB021905. https://doi.org/10.1029/2021jb021905

Palano, M. (2014). On the present-day crustal stress, strain-rate fields and mantle anisotropy pattern of Italy. *Geophysical Journal International*, *200*(2), 969–985. https://doi.org/10.1093/gji/ggu451

Papaleo, E., Cornwell, D., & Rawlinson, N. (2018). Constraints on north anatolian Fault Zone width in the crust and upper mantle from S wave teleseismic tomography. *Journal of Geophysical Research: Solid Earth*, *123*(4), 2908–2922. https://doi.org/10.1002/2017JB015386

Paul, A., Karabulut, H., Mutlu, A. K., & Salaün, G. (2014). A comprehensive and densely sampled map of shear-wave azimuthal anisotropy in the Aegean–Anatolia region. *Earth and Planetary Science Letters*, *389*, 14–22. https://doi.org/10.1016/j.epsl.2013.12.019

Peltzer, G., & Tapponnier, P. (1988). Formation and evolution of strike-slip faults, rifts, and basins during the India-Asia Collision: An experimental approach. *Journal of Geophysical Research*, *93*(B12), 15085–15117. https://doi.org/10.1029/JB093iB12p15085

Perry, M., Kakar, N., Ischuk, A., Metzger, S., Bendick, R., Molnar, P., & Mohadjer, S. (2019). Little geodetic evidence for localized Indian subduction in the Pamir-Hindu Kush of Central Asia. *Geophysical Research Letters*, *46*(1), 109–118. https://doi.org/10.1029/2018gl080065

Piña-Valdés, J., Socquet, A., Beauval, C., Doin, M.-P., D'Agostino, N., & Shen, Z.-K. (2022). 3D GNSS velocity field sheds light on the deformation mechanisms in Europe: Effects of the vertical crustal motion on the distribution of seismicity. *Journal of Geophysical Research: Solid Earth*, *127*(6), e2021JB023451. https://doi.org/10.1029/2021jb023451

Podolefsky, N. S., Zhong, S., & McNamara, A. K. (2004). The anisotropic and rheological structure of the oceanic upper mantle from a simple model of plate shear. *Geophysical Journal International*, *158*(1), 287–296. https://doi.org/10.1111/j.1365-246x.2004.02250.x

Qiao, X., & Zhou, Y. (2021). Geodetic imaging of shallow creep along the Xianshuihe fault and its frictional properties. *Earth and Planetary Science Letters*, *567*, 117001. https://doi.org/10.1016/j.epsl.2021.117001

Read, H. H., & Watson, J. (1975). *Introduction to geology: Earth history. Part II: Later stages of Earth history*. Springer. https://doi.org/10.1007/978-1-349-15613-9

Rebaï, S., Philip, H., Dorbath, L., Borissoff, B., Haessler, H., & Cisternas, A. (1993). Active tectonics in the Lesser Caucasus: Coexistence of compressive and extensional structures. *Tectonics*, *12*(5), 1089–1114. https://doi.org/10.1029/93TC00514

Reguzzoni, M., & Sampietro, D. (2015). GEMMA: An Earth crustal model based on GOCE satellite data. *International Journal of Applied Earth Observation and Geoinformation*, *35*, 31–43. (GOCE earth science applications and models(Based on the ESA GOCE solid earth workshop, 16-17 October 2012. https://doi.org/10.1016/j.jag.2014.04.002

Reilinger, R., & McClusky, S. (2011). Nubia–Arabia–Eurasia plate motions and the dynamics of Mediterranean and Middle East tectonics. *Geophysical Journal International*, *186*(3), 971–979. https://doi.org/10.1111/j.1365-246X.2011.05133.x

Reilinger, R., McClusky, S., Vernant, P., Lawrence, S., Ergintav, S., Cakmak, R., et al. (2006). GPS constraints on continental deformation in the africa-arabia-eurasia continental collision zone and implications for the dynamics of plate interactions. *Journal of Geophysical Research*, *111*(B5). https://doi.org/10.1029/2005JB004051

Replumaz, A., & Tapponnier, P. (2003). Reconstruction of the deformed collision zone between India and Asia by backward motion of lithospheric blocks. *Journal of Geophysical Research*, *108*(B6). https://doi.org/10.1029/2001JB000661

Ritter, J. R., Jordan, M., Christensen, U. R., & Achauer, U. (2001). A mantle plume below the Eifel volcanic fields, Germany. *Earth and Planetary Science Letters*, *186*(1), 7–14. https://doi.org/10.1016/s0012-821x(01)00226-6

Rodriguez, M., Sakellariou, D., Gorini, C., Janin, A., d'Acremont, E., Pourhiet, L. L., et al. (2023). Evolution of the North Anatolian Fault from a diffuse to a localized shear zone in the North Aegean Sea during the Plio-Pleistocene. *Geophysical Journal International*, *235*(3), 2614–2639. https://doi.org/10.1093/gji/ggad364

Royden, L. H. (1993). The tectonic expression slab pull at continental convergent boundaries. *Tectonics*, *12*(2), 303–325. https://doi.org/10.1029/92TC02248

Royden, L. H., Burchfiel, B. C., King, R. W., Wang, E., Chen, Z., Shen, F., & Liu, Y. (1997). Surface deformation and lower crustal flow in Eastern Tibet. *Science*, *276*(5313), 788–790. https://doi.org/10.1126/science.276.5313.788

Saleh, M., & Becker, M. (2014). A new velocity field from the analysis of the Egyptian Permanent GPS Network (EPGN). *Arabian Journal of Geosciences*, *7*(11), 4665–4682. https://doi.org/10.1007/s12517-013-1132-x

Sandwell, D. T. (2022). Elastic solutions for strike-slip faulting. In *Advanced geodynamics: The fourier transform method* (pp. 145–168). Cambridge University Press.

Sandwell, D. T., & Wessel, P. (2016). Interpolation of 2-D vector data using constraints from elasticity. *Geophysical Research Letters*, *43*(20), 10–703. https://doi.org/10.1002/2016gl070340

Savage, J., Gan, W., & Svarc, J. (2001). Strain accumulation and rotation in the Eastern California Shear Zone. *Journal of Geophysical Research*, *106*(B10), 21995–22007. https://doi.org/10.1029/2000jb000127

Savage, J., & Prescott, W. (1978). Asthenosphere readjustment and the earthquake cycle. *Journal of Geophysical Research*, *83*(B7), 3369–3376. https://doi.org/10.1029/jb083ib07p03369

Savage, J. C. (1983). Strain accumulation in western United States. *Annual Review of Earth and Planetary Sciences*, *11*(1), 11–41. https://doi.org/10.1146/annurev.ea.11.050183.000303

Savage, J. C., & Burford, R. O. (1973). Geodetic determination of relative plate motion in central California. *Journal of Geophysical Research*, *78*(5), 832–845. https://doi.org/10.1029/JB078i005p00832

Savage, M. K. (1999). Seismic anisotropy and mantle deformation: What have we learned from shear wave splitting? *Reviews of Geophysics*, *37*(1), 65–106. https://doi.org/10.1029/98RG02075

Savage, M. K., Fischer, K. M., & Hall, C. E. (2004). 01). Strain modelling, seismic anisotropy and coupling at strike-slip boundaries: Applications in New Zealand and the San Andreas fault. In *Vertical coupling and decoupling in the lithosphere*. Geological Society of. https://doi.org/10.1144/GSL.SP.2004.227.01.02

Schulte-Pelkum, V., Becker, T. W., Behr, W. M., & Miller, M. S. (2021). Tectonic inheritance during plate boundary evolution in southern California constrained from seismic anisotropy. *Geochemistry, Geophysics, Geosystems*, *22*(11), e2021GC010099. https://doi.org/10.1029/2021GC010099

Searle, M., Elliott, J., Phillips, R., & Chung, S.-L. (2011). Crustal–lithospheric structure and continental extrusion of Tibet. *Journal of the Geological Society*, *168*(3), 633–672. https://doi.org/10.1144/0016-76492010-139

Şengör, A. (1986). The dual nature of the Alpine-Himalayan system: Progress, problems and prospects. *Tectonophysics*, *127*(3), 177–195. (Tectonics of the Eurasian Fold Belts). https://doi.org/10.1016/0040-1951(86)90060-0

Şengör, A., Görür, N., & Şaroğlu, F. (1985). Strike-Slip faulting and related Basin Formation in zones of tectonic escape: Turkey as a case Study. In *Strike-Slip deformation, Basin Formation, and sedimentation*. SEPM Society for Sedimentary Geology. https://doi.org/10.2110/pec.85.37.0211

Serpelloni, E., Cavaliere, A., Martelli, L., Pintori, F., Anderlini, L., Borghi, A., et al. (2022). Surface velocities and strain-rates in the Euro-Mediterranean region from massive GPS data processing. *Frontiers in Earth Science*, *10*, 907897. https://doi.org/10.3389/feart.2022.907897

Serpelloni, E., Faccenna, C., Spada, G., Dong, D., & Williams, S. D. P. (2013). Vertical GPS ground motion rates in the Euro-Mediterranean region: New evidence of velocity gradients at different spatial scales along the Nubia-Eurasia plate boundary. *Journal of Geophysical Research: Solid Earth*, *118*(11), 6003–6024. https://doi.org/10.1002/2013JB010102

Shaw, M., & Pysklywec, R. (2007). Anomalous uplift of the Apennines and subsidence of the Adriatic: The result of active mantle flow? *Geophysical Research Letters*, *34*(L04311). https://doi.org/10.1029/2006GL028337
Shen, F., Royden, L. H., & Burchfiel, B. C. (2001). Large-scale crustal deformation of the Tibetan Plateau. *Journal of Geophysical Research*, *106*(B4), 6793–6816. https://doi.org/10.1029/2000JB900389
Shen, Z., & Bird, P. (2022). 09). NeoKinema deformation model for the 2023 update to the U.S. national Seismic hazard model. *Seismological Research Letters*, *93*(6), 3037–3052. https://doi.org/10.1785/0220220179
Shen, Z.-K., Jackson, D. D., & Ge, B. X. (1996). Crustal deformation across and beyond the Los Angeles basin from geodetic measurements. *Journal of Geophysical Research*, *101*(B12), 27957–27980. https://doi.org/10.1029/96jb02544
Shen, Z.-K., Lü, J., Wang, M., & Bürgmann, R. (2005). Contemporary crustal deformation around the southeast borderland of the Tibetan Plateau. *Journal of Geophysical Research*, *110*(B11). https://doi.org/10.1029/2004JB003421
Shen, Z.-K., Wang, M., Zeng, Y., & Wang, F. (2015). Optimal interpolation of spatially discretized geodetic data. *Bulletin of the Seismological Society of America*, *105*(4), 2117–2127. https://doi.org/10.1785/0120140247
Silver, P. G. (1996). Seismic ANISOTROPY BENEATH THE CONTINENTS: Probing the depths of geology. *Annual Review of Earth and Planetary Sciences*, *24*(1), 385–432. [Journal Article]. https://doi.org/10.1146/annurev.earth.24.1.385
Silver, P. G., & Chan, W. W. (1991). Shear wave splitting and subcontinental mantle deformation. *Journal of Geophysical Research*, *96*(B10), 16429–16454. https://doi.org/10.1029/91JB00899
Silver, P. G., & Holt, W. E. (2002). The mantle flow field beneath Western North America. *Science*, *295*(5557), 1054–1057. https://doi.org/10.1126/science.1066878
Sokhadze, G., Floyd, M., Godoladze, T., King, R., Cowgill, E., Javakhishvili, Z., et al. (2018). Active convergence between the Lesser and Greater Caucasus in Georgia: Constraints on the tectonic evolution of the Lesser–Greater Caucasus continental collision. *Earth and Planetary Science Letters*, *481*, 154–161. https://doi.org/10.1016/j.epsl.2017.10.007
Sol, S., Meltzer, A., Burgmann, R., Van der Hilst, R., King, R., Chen, Z., et al. (2007). Geodynamics of the southeastern Tibetan Plateau from seismic anisotropy and geodesy. *Geology*, *35*(6), 563–566. https://doi.org/10.1130/G23408A.1
Stamps, D. S., Saria, E., & Kreemer, C. (2018). A geodetic strain rate model for the East African Rift System. *Scientific Reports*, *8*(1), 732. https://doi.org/10.1038/s41598-017-19097-w
Steffen, R., Steffen, H., Kenyeres, A., Nilsson, T., & Lidberg, M. (2025). EuVeM2022—A European three-dimensional GNSS velocity model based on least-squares collocation. *Geophysical Journal International*, *241*(1), 437–453. https://doi.org/10.1093/gji/ggaf052
Sternai, P., Sue, C., Husson, L., Serpelloni, E., Becker, T. W., Willett, S. D., et al. (2019). Present-day uplift of the European Alps: Evaluating mechanisms and models of their relative contributions. *Earth-Science Reviews*, *190*, 589–604. https://doi.org/10.1016/j.earscirev.2019.01.005
Sue, C., Thouvenot, F., Fréchet, J., & Tricart, P. (1999). Widespread extension in the core of the western Alps revealed by earthquake analysis. *Journal of Geophysical Research*, *104*(B11), 25611–25622. https://doi.org/10.1029/1999JB900249
Sun, H., Chang, L., Song, X., & Wang, X. (2025). Crustal deformation across the southeastern flank of the eastern Himalayan syntaxis from 3D velocity and anisotropic structures. *Earth and Planetary Science Letters*, *654*, 119230. https://doi.org/10.1016/j.epsl.2025.119230
Tape, C., Musé, P., Simons, M., Dong, D., & Webb, F. (2009). Multiscale estimation of GPS velocity fields. *Geophysical Journal International*, *179*(2), 945–971. https://doi.org/10.1111/j.1365-246x.2009.04337.x
Tapponnier, P., Peltzer, G., Le Dain, A. Y., Armijo, R., & Cobbold, P. (1982). Propagating extrusion tectonics in Asia: New insights from simple experiments with plasticine. *Geology*, *10*(12), 611–616. https://doi.org/10.1130/0091-7613(1982)10⟨611:PETIAN⟩2.0.CO;2
Tapponnier, P., Zhiqin, X., Roger, F., Meyer, B., Arnaud, N., Wittlinger, G., & Jingsui, Y. (2001). Oblique stepwise rise and growth of the Tibet Plateau. *Science*, *294*(5547), 1671–1677. https://doi.org/10.1126/science.105978
Tatar, O., Poyraz, F., Gürsoy, H., Cakir, Z., Ergintav, S., & Akpınar, Z. (2012). Crustal deformation and kinematics of the Eastern Part of the North Anatolian Fault Zone (Turkey) from GPS measurements. *Tectonophysics*, *518*, 55–62.
Taylor, G., Rost, S., & Houseman, G. (2016). Crustal imaging across the North Anatolian Fault Zone from the autocorrelation of ambient seismic noise. *Geophysical Research Letters*, *43*(6), 2502–2509. https://doi.org/10.1002/2016GL067715
Ten Brink, U., Schoenberg, N., Kovach, R., & Ben-Avraham, Z. (1990). Uplift and a possible moho offset across the Dead Sea transform. *Tectonophysics*, *180*(1), 71–85. https://doi.org/10.1016/0040-1951(90)90373-G
Thatcher, W. (2009). How the continents deform: The evidence from tectonic geodesy*. *Annual Review of Earth and Planetary Sciences*, *37*(1), 237–262. https://doi.org/10.1146/annurev.earth.031208.100035
Thatcher, W. (2007). Microplate model for the present-day deformation of Tibet. *Journal of Geophysical Research*, *112*(B1). https://doi.org/10.1029/2005JB004244
Tian, D., Uieda, L., Leong, W. J., Fröhlich, Y., Schlitzer, W., Grund, M., et al. (2024). PyGMT: A Python interface for the Generic Mapping Tools (Version 0.12.0) [Software]. *Zenodo*. https://doi.org/10.5281/zenodo.11062720
Timsina, P., Hearn, T. M., & Ni, J. F. (2024). Crust and mantle flow from central Tibetan Plateau to the Indo-Burma subduction Zone. *Journal of Geophysical Research: Solid Earth*, *129*(10), e2023JB027540. https://doi.org/10.1029/2023JB027540
Tong, X., & Chen, S. (2024). 08). Temporal and spatial variation of fault creep along the xianshuihe fault from InSAR Stacking. *Geophysical Journal International*, ggae310. https://doi.org/10.1093/gji/ggae310
Tosi, L., Teatini, P., & Strozzi, T. (2013). Natural versus anthropogenic subsidence of Venice. *Scientific Reports*, *3*(1), 2710. https://doi.org/10.1038/srep02710
Townend, J., & Zoback, M. D. (2004). Regional tectonic stress near the San Andreas fault in central and southern California. *Geophysical Research Letters*, *31*(15). https://doi.org/10.1029/2003GL018918
Townend, J., & Zoback, M. D. (2006). Stress, strain, and mountain building in central Japan. *Journal of Geophysical Research*, *111*(B3). https://doi.org/10.1029/2005JB003759
van Gelder, I., Willingshofer, E., Sokoutis, D., & Cloetingh, S. (2017). The interplay between subduction and lateral extrusion: A case study for the European Eastern Alps based on analogue models. *Earth and Planetary Science Letters*, *472*, 82–94. https://doi.org/10.1016/j.epsl.2017.05.012
Vardić, K., Clarke, P. J., & Whitehouse, P. L. (2022). A GNSS velocity field for crustal deformation studies: The influence of glacial isostatic adjustment on plate motion models. *Geophysical Journal International*, *231*(1), 426–458. https://doi.org/10.1093/gji/ggac047
Vauchez, A., Tommasi, A., & Mainprice, D. (2012). Faults (shear zones) in the Earth's mantle. *Tectonophysics*, *558*, 1–27. https://doi.org/10.1016/j.tecto.2012.06.006
Vilotte, J. P., Madariaga, R., Daigniéres, M., & Zienkiewicz, O. (1986). Numerical study of continental collision: Influence of buoyancy forces and an initial stiff inclusion. *Geophysical Journal International*, *84*(2), 279–310. https://doi.org/10.1111/j.1365-246X.1986.tb04357.x
Viltres, R., Doubre, C., Doin, M.-P., & Masson, F. (2025). Aseismic creep and strain partitioning accommodating the Nubia-Eurasia oblique convergence in northern Africa from InSAR analysis. *Geology*, *53*(4), 349–354. https://doi.org/10.1130/G53117.1

Viltres, R., Jónsson, S., Alothman, A. O., Liu, S., Leroy, S., Masson, F., et al. (2022). Present-Day motion of the arabian plate. *Tectonics*, *41*(3), e2021TC007013. https://doi.org/10.1029/2021tc007013

Viltres, R., Jónsson, S., Ruch, J., Doubre, C., Reilinger, R., Floyd, M., & Ogubazghi, G. (2020). Kinematics and deformation of the southern Red Sea region from GPS observations. *Geophysical Journal International*, *221*(3), 2143–2154. https://doi.org/10.1093/gji/ggaa109

Vinnik, L. P., Makeyeva, L. I., Milev, A., & Usenko, A. Y. (1992). Global patterns of azimuthal anisotropy and deformations in the continental mantle. *Geophysical Journal International*, *111*(3), 433–447. https://doi.org/10.1111/j.1365-246X.1992.tb02102.x

Walker, K., Bokelmann, G., Klemperer, S., & Bock, G. (2005). Shear-wave splitting around the eifel hotspot: Evidence for a mantle upwelling. *Geophysical Journal International*, *163*(3), 962–980. https://doi.org/10.1111/j.1365-246x.2005.02636.x

Wang, C.-Y., Flesch, L. M., Silver, P. G., Chang, L.-J., & Chan, W. W. (2008). Evidence for mechanically coupled lithosphere in central Asia and resulting implications. *Geology*, *36*(5), 363–366. https://doi.org/10.1130/G24450A.1

Wang, L., & Barbot, S. (2023). Three-dimensional kinematics of the India–Eurasia collision. *Communications Earth and Environment*, *4*(1), 164. https://doi.org/10.1038/s43247-023-00815-4

Wang, L., Wang, R., Roth, F., Enescu, B., Hainzl, S., & Ergintav, S. (2009). Afterslip and viscoelastic relaxation following the 1999 M 7.4 İzmit earthquake from GPS measurements. *Geophysical Journal International*, *178*(3), 1220–1237. https://doi.org/10.1111/j.1365-246X.2009.04228.x

Wang, M., & Shen, Z.-K. (2020). Present-day crustal deformation of continental China derived from GPS and its tectonic implications. *Journal of Geophysical Research: Solid Earth*, *125*(2), e2019JB018774. https://doi.org/10.1029/2019jb018774

Watson, A. R., Elliott, J. R., Lazecký, M., Maghsoudi, Y., McGrath, J. D., & Walters, R. J. (2024). An InSAR-GNSS velocity field for Iran. *Geophysical Research Letters*, *51*(10), e2024GL108440. https://doi.org/10.1029/2024GL108440

Wedmore, L. N., Biggs, J., Floyd, M., Fagereng, Å., Mdala, H., Chindandali, P., et al. (2021). Geodetic constraints on cratonic microplates and broad strain during rifting of thick Southern African lithosphere. *Geophysical Research Letters*, *48*(17), e2021GL093785. https://doi.org/10.1029/2021gl093785

Weertman, J., & Weertman, J. (1964). *Elementary dislocation theory*. Macmillan. Retrieved from https://books.google.com.sa/books?id=Ok1RAAAAMAAJ

Weiss, J. R., Walters, R. J., Morishita, Y., Wright, T. J., Lazecky, M., Wang, H., et al. (2020). High-resolution surface velocities and strain for Anatolia from Sentinel-1 InSAR and GNSS data. *Geophysical Research Letters*, *47*(17), e2020GL087376. https://doi.org/10.1029/2020GL087376

Wessel, P., Luis, J. F., Uieda, L., Scharroo, R., Wobbe, F., Smith, W. H. F., & Tian, D. (2019). The generic mapping tools version 6. *Geochemistry, Geophysics, Geosystems*, *20*(11), 5556–5564. https://doi.org/10.1029/2019GC008515

Wolfe, C. J., & Solomon, S. C. (1998). Shear-Wave splitting and implications for Mantle Flow Beneath the MELT Region of the East Pacific rise. *Science*, *280*(5367), 1230–1232. https://doi.org/10.1126/science.280.5367.1230

Wortel, M. J. R., & Spakman, W. (2000). Subduction and slab detachment in the mediterranean-carpathian Region. *Science*, *290*(5498), 1910–1917. https://doi.org/10.1126/science.290.5498.1910

Wu, D.-L., Ge, W.-P., Liu, S.-Z., Yuan, D.-Y., Zhang, B., & Wei, C.-M. (2024). Present-day 3D crustal deformation of the Northeastern Tibetan Plateau from space geodesy. *Geophysical Research Letters*, *51*(4), e2023GL106143. https://doi.org/10.1029/2023GL106143

Wu, Y., Zheng, Z., Nie, J., Chang, L., Su, G., Yin, H., et al. (2022). High-precision vertical movement and three-dimensional deformation pattern of the Tibetan plateau. *Journal of Geophysical Research: Solid Earth*, *127*(4), e2021JB023202. https://doi.org/10.1029/2021JB023202

Yamamoto, R., Kido, M., Ohta, Y., Takahashi, N., Yamamoto, Y., Pinar, A., et al. (2019). Seafloor geodesy revealed partial creep of the north anatolian fault submerged in the Sea of Marmara. *Geophysical Research Letters*, *46*(3), 1268–1275. https://doi.org/10.1029/2018GL080984

Yang, W., & Hauksson, E. (2013). 04). The tectonic crustal stress field and style of faulting along the Pacific North America Plate boundary in Southern California. *Geophysical Journal International*, *194*(1), 100–117. https://doi.org/10.1093/gji/ggt113

Yeck, W. L., Hatem, A. E., Goldberg, D. E., Barnhart, W. D., Jobe, J. A. T., Shelly, D. R., et al. (2023). Rapid Source Characterization of the 2023 Mw 6.8 Al Haouz, Morocco, Earthquake. *The Seismic Record*, *3*(4), 357–366. https://doi.org/10.1785/0320230040

Yin, A., & Harrison, T. M. (2000). Geologic evolution of the Himalayan-Tibetan orogen. *Annual Review of Earth and Planetary Sciences*, *28*(1), 211–280. https://doi.org/10.1146/annurev.earth.28.1.211

Zelenin, E., Bachmanov, D., Garipova, S., Trifonov, V., & Kozhurin, A. (2021). The database of the active faults of Eurasia (AFEAD): Ontology and design behind the continental-scale dataset. *Earth System Science Data Discussions*, *2021*, 1–20. https://doi.org/10.5194/essd-14-4489-2022

Zeng, Y. (2022). GPS velocity field of the western United States for the 2023 National Seismic Hazard Model Update. *Seismological Society of America*, *93*(6), 3121–3134. https://doi.org/10.1785/0220220180

Zhang, J., ze Wen, X., ling Cao, J., Yan, W., lin Yang, Y., & Su, Q. (2018). Surface creep and slip-behavior segmentation along the northwestern Xianshuihe fault zone of southwestern China determined from decades of fault-crossing short-baseline and short-level surveys. *Tectonophysics*, *722*, 356–372. https://doi.org/10.1016/j.tecto.2017.11.002

Zhang, S., & Karato, S.-i. (1995). Lattice preferred orientation of olivine aggregates deformed in simple shear. *Nature*, *375*(6534), 774–777. https://doi.org/10.1038/375774a0

Zhang, Y. G., Zheng, W. J., Wang, Y. J., Zhang, D. L., Tian, Y. T., Wang, M., et al. (2018). Contemporary deformation of the North China Plain from global positioning System data. *Geophysical Research Letters*, *45*(4), 1851–1859. https://doi.org/10.1002/2017GL076599

Zheng, G., Wang, H., Wright, T. J., Lou, Y., Zhang, R., Zhang, W., et al. (2017). Crustal deformation in the India-Eurasia collision zone from 25 years of GPS measurements. *Journal of Geophysical Research: Solid Earth*, *122*(11), 9290–9312. https://doi.org/10.1002/2017JB014465

Zubovich, A., Schöne, T., Metzger, S., Mosienko, O., Mukhamediev, S., Sharshebaev, A., & Zech, C. (2016). Tectonic interaction between the Pamir and Tien Shan observed by GPS. *Tectonics*, *35*(2), 283–292. https://doi.org/10.1002/2015TC004055